A Density Functional Study of Actinyl Containing Complexes

By

Joel John Paul Joseph Berard

A Thesis
Submitted to the Faculty of Graduate Studies
In Partial Fulfillment of the Requirements for the Degree of
Master of Science

Department of Chemistry
University of Manitoba
Winnipeg, Manitoba

Abstract

Density functional (DFT) methods are first used to study 22 of the most stable solution-phase UN_4O_{12} isomers containing uranyl nitrate, $UO_2(NO_3)_2$. Based on relative free energy calculations, 4 solution (**a6**, **a5**, **a8**, and **a1**) and 5 gas-phase isomers (**a1**, **a2**, **a3**, **b1**, and **b2**) are identified as the strongest candidates to exist and possibly predominate within their respective environments.

DFT is then applied to a new form of binucleating Schiff–base polypyrrolic macrocycles containing actinyl ions $[AnO_2]^{n+}$ (An = U, Np, Pu; n = 1, 2) and 3d transition metals (TM): Mn, Fe, Co, and Zn. Formal bond order evidence is provided for 24 TM to actinyl–endo–oxygen partial bond formations. Special structural cases are discussed. Redox potentials for $\mathbf{An^{VI}O_21/An^{V}O_21^-}$ couples closely follow the Np > Pu > U trend seen for $AnO_2(H_2O)_5^{2+/1+}$. Predictions of –1.10, 0.25, and 0.01 eV are made for U, Np, and Pu redox potentials.

Acknowledgements

I would like to thank my advisor, Dr. Georg Schreckenbach, for his valued support and guidance in scientific matters relating to the contents of this thesis and for taking the time to proofread the thesis and the many manuscript revisions related to the thesis. Also, thanks to Grigory A. Shamov and Mohammad A. Namdarghanbari for many helpful discussions and to Dr. Dimitri N. Laikov, Moscow/Stockholm, for making his Priroda code available. Furthermore, thanks to Dr. Georg Schreckenbach for his major contribution to the contents of section **3.3.5** on dissociation, and the valuable comments of Drs. James D. Xidos and Peter H. M. Budzelaar of the University of Manitoba, on this issue. Thanks also to Polly L. Arnold, Dipti Patel, and Jason B. Love at the University of Edinburgh for their collaboration, in providing experimental data, as well as suggestions and feedback regarding Chapter 4 of this thesis and its accompanying manuscript. Lastly, thanks to Gernot Frenking, of the University of Marburg, for resolving an issue with the usage of the ADF ETS energy decomposition method and suggesting the use of NBO analysis instead.

Financial support from the Natural Sciences and Engineering Research Council of Canada and from the University of Manitoba start-up funds and The Research Grants Program are also gratefully acknowledged.

Table of Contents

List of Tables

List of Figures

List of Copyrighted Material for which Permission was Obtained

List of Abbreviations

ad hoc	for this purpose
ADF	Amsterdam Density Functional (software)
AE	all electron (method)
An	actinyl
a.u.	atomic units
B3LYP	non-local Becke exact exchange combined with the Lee, Yang and Parr correlation functional (hybrid method)
CBS	Complete Basis Set
cc–pVTZ	correlation consistent polarized triple zeta (basis set)
CCSD(T)	coupled cluster singles, doubles and partial triples (method)
CGF	contracted Gaussian function
CH_3NO_2	nitromethane (solvent)
CI	configuration interaction (method)
COSMO	conductor-like screening model (solvation)
COT	cyclooctatrienyl
C–PCM	conductor polarized continuum model (solvation)
Cp	cyclopentadienyl
Cp*	methylated cyclopentadienyl
DFT	density functional theory
e.g.	*exempli gratia*, for instance
ECP	effective–core potential

Eq. or Eqn.	equation
etc.	*et cetera* “And so on”
ESI	electrospray ionization
ESI–MS	electrospray ionization mass spectrometry
EXAFS	extended X–ray absorption fine structure spectroscopy
Expt. or exptl.	Experimental
FT–ICR–MS	Fourier transform ion–cyclotron resonance mass spectrometry
g03	Gaussian 2003 (software)
GGA	generalized gradient approximation (functional method)
GTO	Gaussian–type orbital
HEU	highly enriched uranium
HF	Hartree–Fock
HOMO	highest occupied molecular orbital
i.e.	*id est*, that is to say
IR	infrared (frequency)
KS	Kohn–Sham
LC–ECP	large core effective core potential (relativistic method)
LCAO	linear combination of atomic orbitals (basis set expansion)
LEU	low-enriched uranium
MO	molecular orbital
NMR	nuclear magnetic resonance
NR	nonrelativistic
p5	Priroda version 5 (software)

PBE	Perdew, Burke and Ernzerhof (GGA method)
PCM	polarized continuum model
PUREX	Plutonium Uranium Recovery by Extraction
RECP	relativistic effective–core potential
RI	resolution of identity
redox	reduction–oxidation (potential)
SAS	solvent accessible surface
SC–ECP	small core effective core potential (relativistic method)
SCF	self-consistent field
SCM	Scientific Computing & Modelling
SCRF	self-consistent reaction field
STO	Slater–type orbital
SVWN	Slater exchange functional combined with Vosko, Wilk and Nusair correlation functional (GGA method)
THF or thf	tetrahydrofuran (solvent)
TM	transition metal
TZP	triple zeta polarized (basis set)
TZVP	triple zeta valence polarized (basis set)
VDZ	valence double zeta (basis set)
VTZ	valence triple zeta (basis set)
XC	exchange–correlation (potential)
ZORA	zero order relativistic approximation (relativistic method)
ZPE	zero-point energy (correction)

CHAPTER ONE

INTRODUCTION

1.1 Motivation

The ongoing proliferation of fissile material worldwide, whether for the purposes of being used for nuclear weapons or nuclear power generation has created a genuine cause for anxiety regarding the immediate and long-term global consequences to both personal health and the environment. As a result, the radioactive waste and groundwater contamination created by six decades of atomic weapons production and nuclear power generation, has made the chemistry of the early actinides (An = U, Np, Pu, Am) and actinyls AnO_2^{n+} (n = 1 or 2) related to one of the most pressing environmental challenges of our time. Cause for concern exists should certain actinides in radioactive wastes be introduced into the environment due to their toxicity and, in particular, due to the long half-lives of some of their isotopes and those of their daughter elements. Because of these concerns the importance of separating individual actinide elements from one another or from the other elements in the nuclear fuel cycle, as well as furthering the understanding of the environmental chemistry of the relevant actinide and actinyl complexes, has been and is now even more so, the focus of many ongoing and growing numbers of research efforts [2, 3].

Under the general theme of "actinyl containing complexes" we investigate, through the use of computational methods, two unique categories of molecular structures. Through such efforts we are looking to build on the existing level of knowledge of these

environmentally important, yet less commonly studied, triatomic components, in the hopes that continued developments in this field will lead to beneficial advances in relation to their consequential role within nuclear fuel processing and waste storage.

1.2 Overview

What is interesting about our investigations into two very different cases of actinyl containing molecules is that they require us to work within all three phases of matter (solid, liquid, and gas) to produce the molecular structures and properties we set out to study. First, we begin in the solid-state phase, where the existing experimental results of X–Ray, neutron or extended X–ray absorption fine structure (EXAFS) spectroscopy provide us with the structural starting points — connectivity, bond lengths and angles — for the molecular structures that we are looking to build, as well as the formal actinide oxidation states. Also provided, is some degree of likelihood that such structures may indeed exist in the solution from which they originated. Next, we turn to the gas-phase or more specifically the vacuum phase, which is the medium in which the quantum mechanical models provide us with the most accurate, reliable and expedient results. Lastly, to model the molecules of this study under the environmental conditions in which they are most likely to exist and in the chemical reactions they are most likely to take place we need to work in the liquid-phase or more appropriately the solution–phase. Most often this means within aqueous solutions, but in our case due to the high degree of

reactivity of the early actinides with both oxygen and water this means nonaqueous or organic solvent solutions.

Computational modeling within solution, due to its high degree of complexity, still has a long way to go to reach a level of reliability and shorter calculation times currently established for the gas-phase models, especially for some of the larger molecules (108 atoms) that we work with in this study [4, 5]. The complexity of modeling kinetic factors, concentrations, solubilities, and in particular for actinyls, many oxidation states along with their abundant complexation possibilities, still remains to be worked out. The level of pH, for example, is a very critical factor in our investigation into the structure of actinyl complexes, for many of the separation techniques directed at the early actinides and actinyls occur in acidic solutions, whereas, much of the waste storage tanks of repositories contain highly basic solid solutions.

We again turn to actinide solid-state structural chemistry to provide us with a broad organization of the existing areas of research for which structural data has been accumulating. Roughly speaking we can break these areas down into three divisions and two subdivisions of actinide and actinyl containing complexes: 1) the inorganic compounds, which account for those made up of oxides, hydrides, borohydrides, borides, carbides, silicides, pnictides, chalcogenides, halides, oxohalides, carbonates, nitrates, phosphates, arsenates and sulfates among others, 2) the coordination compounds which can be further subdivided into a) the organic acyclic carboxylic acid derivatives consisting of formates, acetates, carboxylates, oxalates and malonates as well as many others and b) the macrocycles made up of macrocyclic ligands including crown ethers, calixarenes, porphyrins, expanded porphyrins, and phthalocyanines, and 3) the

organometallic compounds involving derivatives of cyclopentadienyl (Cp, Cp*), cyclooctatrienyl (COT), indenyl, arene, etc.

Before providing a thorough investigation into two quite different types of actinyl containing structures in chapters 3 and 4, we use chapter 2 to outline the quantum chemical theory forming the foundation of the approximation methods used, as well as their features. Focus is placed on methods specific to this research, at times including more than one approach to accomplishing the same computational task.

Our first case study, chapter 3, of actinyl containing molecules is drawn from the inorganic actinide compounds containing nitrates. More specifically uranyl nitrate $UO_2(NO_3)_2$ forms the core component of an investigation into the relative stabilities and properties of the computationally most stable UN_4O_{12} isomers within both gas-phase and solution. Although the computational investigation into UN_4O_{12} isomers is somewhat challenging due to the sizes of these structures (17 atoms), our second case study of binucleated Schiff–base polypyrrolic macrocycles, at up to 108 atoms, is a major increase in size and challenge. Drawn from the second subdivision of actinyl containing coordination compounds we proceed to examine, in chapter 4, both structure and properties across the actinyl series (An = U, Np, Pu) of metals within one cavity, along with the 3d series of transition metals (TM), Mn, Fe, Co, and Zn within the second cavity. This increase in complexity is accompanied by substantially longer turn-around times for obtaining results, as well as an even more limited choice of available accurate computational methods.

We conclude with the fifth chapter, summarizing some of our important results, as well as providing an outlook of where future investigations may best be directed. An

appendix, for supplementary material to chapter 3, has also been provided. In the appendix the results of the higher energy UN_4O_{12} isomers investigated, beyond the 22 selected, are discussed in greater detail.

1.3 The Early Actinides and their Actinyls

Of the three early actinide elements, uranium, neptunium, and plutonium, only uranium is present in sufficient amounts to warrant extraction from natural sources. The richest deposits of uranium are located in northern Saskatchewan, Canada with other very large deposits found in Kazakhstan, Australia, and the United States. Of the twenty-four known isotopes of Uranium the most abundant and naturally occurring ^{238}U represents 99.28%, whereas the strategically important fissionable ^{235}U exists in nature to the extent of only 0.71%. Uranium is not only widely distributed in the Earth's crust but is also found in significant concentrations in the oceans (3.3 μg/L) mostly as the anionic complex $UO_2(CO_3)_3^{4-}$ [6]. Five grades of isotopically separated uranium are commonly recognized: depleted ^{235}U (< 0.71%), natural ^{235}U (0.71%), low–enriched ^{235}U (LEU, 0.71–20%), highly enriched ^{235}U (HEU, 20–90%), and weapons grade ^{235}U (> 90%). HEU is produced from natural ^{235}U for use in nuclear weapons and commercial nuclear reactors [2].

Songkasiri et al. [7] recently determined Np^V to be the most mobile of the actinide species in solution. With the long-lived ^{237}Np isotope, formed from the radioactive decay of ^{241}Pu, being the principal actinide present within nuclear waste even after 1 million

years, it is considered to be one of the largest contributors to the long-term potential threat of radioactivity from nuclear waste.

The two primary fissile isotopes are ^{235}U and the strategically important ^{239}Pu, which has a low critical mass of < 2 Kg. The ^{239}Pu isotope is now produced by the ton in nuclear reactors. Three grades of plutonium are commonly recognized: weapon-grade ^{240}Pu (< 7%), fuel-grade ^{240}Pu (7–18%) and reactor-grade ^{240}Pu (18%). High-level waste from the isolation of ^{239}Pu also contains large quantities of ^{238}Pu, as well as heavier Pu isotopes. Isotope ^{238}Pu is considered to be an important fuel source and is commonly used as a source of energy in both earth and space borne satellites [2].

These and other radiotoxic actinides, found in nuclear fuel processing and waste storage, pose an immediate and future environmental concern. Treatment often involves either separation for reuse or immobilization for long-term storage. The waste solutions from the processing of irradiated uranium fuel contain U, Np, and Pu isotopes but often also contain other isotopes representative of as much as a third of the periodic table of elements. U, Np, and Pu can often be isolated and purified by a combination of solvent extraction, ion exchange, and precipitation/coprecipitation techniques.

The separation of the early actinides from their fission products and from each other is generally accomplished by adjusting the oxidation state of the actinide ion in aqueous solution to make the coordination chemistry substantially different from that of the other species to be separated.

The radioactivity, toxicity, and chemical reactivity of the actinides make handling them in atmosphere-controlled glove boxes a necessity. When high levels of penetrating radiation are encountered, manipulation also needs to be done with remote controls. With

the exception of depleted uranium special containment and shielding facilities are required for safe handling of these substances. Not only is containment important for radiation shielding but it is also necessary to prevent inhalation because of the toxicity of these elements. Inhaled transuranium elements can deposit in the lungs and ingested elements can translocate to the bone, where radioactivity can lead to neoplasms.

The variety and strength of ligands that form complexes with actinide ions in aqueous solutions are limited by the preference of the actinides for hard donor ligands and by the tendency of actinides towards hydrolysis. Consequently, ligands that bind the highly electropositive cations in aqueous solution usually contain some form of 'hard' Lewis base (oxygen or fluorine) donor sites. The strength and basicity of the ligands containing solely soft donors generally are insufficient to suppress the precipitation of actinide hydroxides. In organic solvents, where actinide hydrolysis is not a significant factor, ligands with softer donors such as nitrogen and sulfur form actinide complexes that are generally more stable, but to a lesser degree than similar oxygen donor ligands.

The complexing ability for actinyl containing complexes typically follow the order of fluoride > nitrate > chloride > perchlorate for the singly charged anions and carbonate > oxalate > sulfate for dianions. Another powerful complexing agent for actinides is the phosphate trianion, PO_4^{3-}. Complex stabilities, containing the same ligands, often follow the order $An^{4+} > AnO_2^{2+} \approx An^{3+} > AnO_2^{+}$ and increase for ions of the same charge, as the ionic radius gets smaller across the actinide series [2].

Actinides, in the higher oxidation states, form unusually stable covalent bonds to oxygen with partial triple bond character that persists as a linear actinyl unit through a large variety of chemical environments. Coordination of 4, 5, and 6, with either

monodentate or bidentate ligands, occur most often in the equatorial plane perpendicular to the linear O=An=O axis, typically generating octahedral, pentagonal bipyramidal, and hexagonal bipyramidal geometries.

The trans-oxo uranyl unit was first elucidated by Fankuchen in 1935 [8] and since then hundreds of structural characterizations have been published. Isostructural hexavalent actinyls are also known for neptunyl, plutonyl, and americyl. The An=O bond strength and reduction resistance both decrease across the series U > Np > Pu > Am. The formation of AmO_2^{2+} requires the use of strong oxidizing agents and is less commonly studied than the other three actinyls. Because of this and in the interest of working with a manageable amount of data, americyl was not included in this thesis study.

Actinyls readily form complexes with ionic F^-, Cl^-, O^{2-}, OH^-, SO^{4-}, NO^{3-}, PO_4^{3-}, CO_3^{2-}, and carboxylates, as well as neutral H_2O, tetrahydrofuran (thf), and pyridine. Oxygen–containing electron donor ligands such as tributyl and dibutyl phosphates, ketones, and ethers also form strong complexing agents. Such reagents continue to be used on an industrial scale for the extraction and separation of actinides. Chelating ligands are also known to form strong actinide complexes and ongoing investigations into the multidentate chelating abilities of macrocyclic ligands such as crown ethers [2, 9, 10], calixarenes [2, 11], expanded-porphyrins [2, 12-17], and phthalocyanines [2, 17] are adding to this active field of research.

Furthering the understanding of the chemistry of the early actinide elements, An = U, Np, and Pu and their common actinyl formations AnO_2^{n+} (n = 1 or 2) found in aqueous and nonaqueous solutions, is one of the key aims of this research. These elements have been explored to a much lesser extent than those before them in the periodic table. With

all the actinides being radioactive and most of them either scarce (therefore expensive to obtain) or toxic, they are often found to be difficult to study experimentally. This creates an opportunity for computational studies to supplement some of the experimental efforts or potentially allows experimentalists to be better informed and prepared to make time saving decisions before proceeding experimentally.

Furthermore, the early actinides are among the heaviest elements, containing 90 electrons or more. This is before even considering their molecular forms, thus often leading to very time consuming and often, difficult calculations. With the 5f, 6s, 6d, 7s, and 7p orbitals of these elements all being relatively close in energy and spatial extent [18, 19], the possibility of entirely new bonding schemes often exist [2, 20]. As well, to approach chemical accuracy (< 2 kcal/mol) it is deemed necessary to include electron correlation effects, resulting from electron–electron interactions. Even more importantly scalar and often also spin–orbit relativistic effects must be included [18, 21-24].

1.3.1 Electronic Configurations of Early Actinides

The 5f orbitals are delocalized and less contracted at the beginning of the actinide series than those of the 4f orbitals of the lanthanides and have been shown to play a significant role in the covalent metal–ligand An=O bonding. As the 5f shell fills, the 5f electrons become more localized and the energy levels fall. In the crossover region, at plutonium, where the transition from delocalized to localized takes place the electronic behavior is especially complicated because of the small energy differences between

delocalized and localized 5f electrons. This is reflected in the complex chemical and physical properties of U, Np, and especially Pu. As well, with the 5f orbitals overlapping the 6p, 6d, and 7s orbitals, the closeness in energy of the many electronic configurations can potentially lead to multiple self-consistent forms of similar structure and energy. Plutonium, in particular, is sensitive to chemical variations, especially in the presence of hydrogen or water. Its ability to have multiple oxidation states in solution at the same time depends on several key factors: the most important of these are the tendency of Pu^{IV} and Pu^{V} to disproportionate, and the relatively slow kinetics of reactions that involve the making or breaking of bonds in plutonyl ions (PuO_2^{2+} and PuO_2^{+}). Other factors include ion concentration, ionic strength, pH, temperature, and the presence or absence of complexing ligands [2].

Electronic structure calculations have shown that one must consider more than just the occupied 5f orbitals for metal–ligand bonding in the early-actinyls. The virtual 5f and 6d orbitals, as well as the semicore 6s and 6p orbitals also play an important role (Figure 1–1) [2, 18].

Unlike their 4f counterparts the 5f electrons of the early actinides are not completely shielded by the 6s and 6p electrons, resulting in a significant radial extention of the 5f orbitals that allows for overlap with ligand orbitals and a covalent bonding contribution. However, the covalent contribution is relatively small and bonding is still thought to be predominantly ionic in character. In addition, there is an increasing tendency for the 6d and 7s electrons to experience less shielding from the nuclear charge as an increase occurs along the actinide series for a given oxidation state. This reduced shielding leads to a contraction of the atomic radius, “the actinide contraction”. For the

early actinides the addition of each 5f electron, along with the accompanying increase in positive nuclear charge, increases electrostatic bonding forces, thereby resulting in a decrease in atomic volume.

Figure 1–1. Radial probability densities of Pu^{3+} valence orbitals from relativistic Hartree–Fock orbitals $\Phi_{nl}(r)$. Copyright permission obtained from Hans van Sintmaartensdijk/Springer on 11/30/07 and David L. Clark/LANL on 12/08/07 [2, 3].

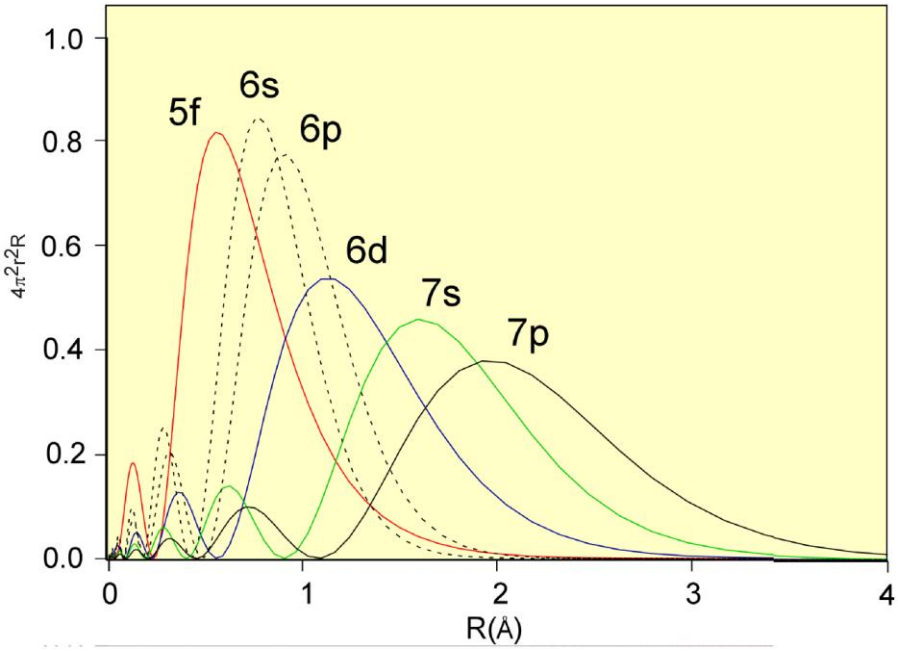

Furthermore, with the radial distributions of the 6s and 6p semicore orbitals found to lie in the valence region between 5f and 6d, they are considered to be active in chemical bonding. As well, the relatively low-lying 6d orbitals have greater spatial extent than the 5f orbitals thus increasing their ability to form bonds.

Spin–orbit coupling and electron correlation effects are also found to be extremely important. Unlike the strong splitting caused by the presence of a ligand field in 3d transition metals those of the more contracted 5f orbitals show only weak splitting. As a consequence, the occupation of these closely spaced unpaired 5f electrons determine

the ground state electron configurations, which generally leads to a variety of computationally difficult to model, closely spaced, open-shell states.

1.3.2 Electronic Strucure of Actinyls

The electronic structure of the actinyl unit AnO_2^{2+} is closely tied to the orbitals of the actinide atoms. If we consider the fully ionic picture, the actinyl cation is treated as An^{6+} and the two oxygen anions as O^{2-}. In this picture the oxygen atoms adopt a closed-shell configuration $2s^2 2p^6$ of an inert gas while uranium adopts closed-shell $5f^0$ state (Figure 1–2).

As for neptunium and plutonium they adopt open-shell $5f^1$ and $5f^2$ states ($1\delta_u$ or $1\phi_u$), with one and two unpaired electron configurations, respectively.

There has been much disagreement over the ordering of the highest filled orbitals of UO_2^{2+}—examples of alternate orderings include [23, 25, 26]—even so, most calculations predict $2\sigma_u$ as the highest occupied molecular orbital (HOMO), as shown in Figure 1–2. Also, since U^{6+} is an f^0 ion, the highest filled MOs of UO_2^{2+} are thought to be mostly $O(2p^6)$ in character. Because of the cylindrical symmetry of the linear UO_2^{2+} unit, the allowed U(5f) (ungerade) and U(6d) (gerade) interactions are mutually exclusive. Thus only the 5f (σ_u, π_u) MOs have the correct symmetry to interact with the $3\sigma_u$, $3\pi_u$ MOs and in turn only 6d (σ_g, π_g) MOs can interact with the $2\sigma_g$, $2\pi_g$ MOs. Therefore, even though the 12 valence electrons all originate from the two oxygen atoms, both the 6d and 5f actinyl orbitals are thought to have significant participation in forming what is

generally considered to be a partial triple bond between the actinide metal and each oxygen atom.

Figure 1–2. Ionic model MO diagram of UO_2^{2+}, showing atomic orbital interactions between U^{6+} ($6p^6$, $5f^0$, $6d^0$) and two O^{2-} ($2s^2$, $2p^6$), (spin-orbit component excluded). Copyright permission obtained from Hans van Sintmaartensdijk/Springer on 11/30/07 and from Nikolas Kaltsoyannis/University College, London, on 01/14/08 [2, 21].

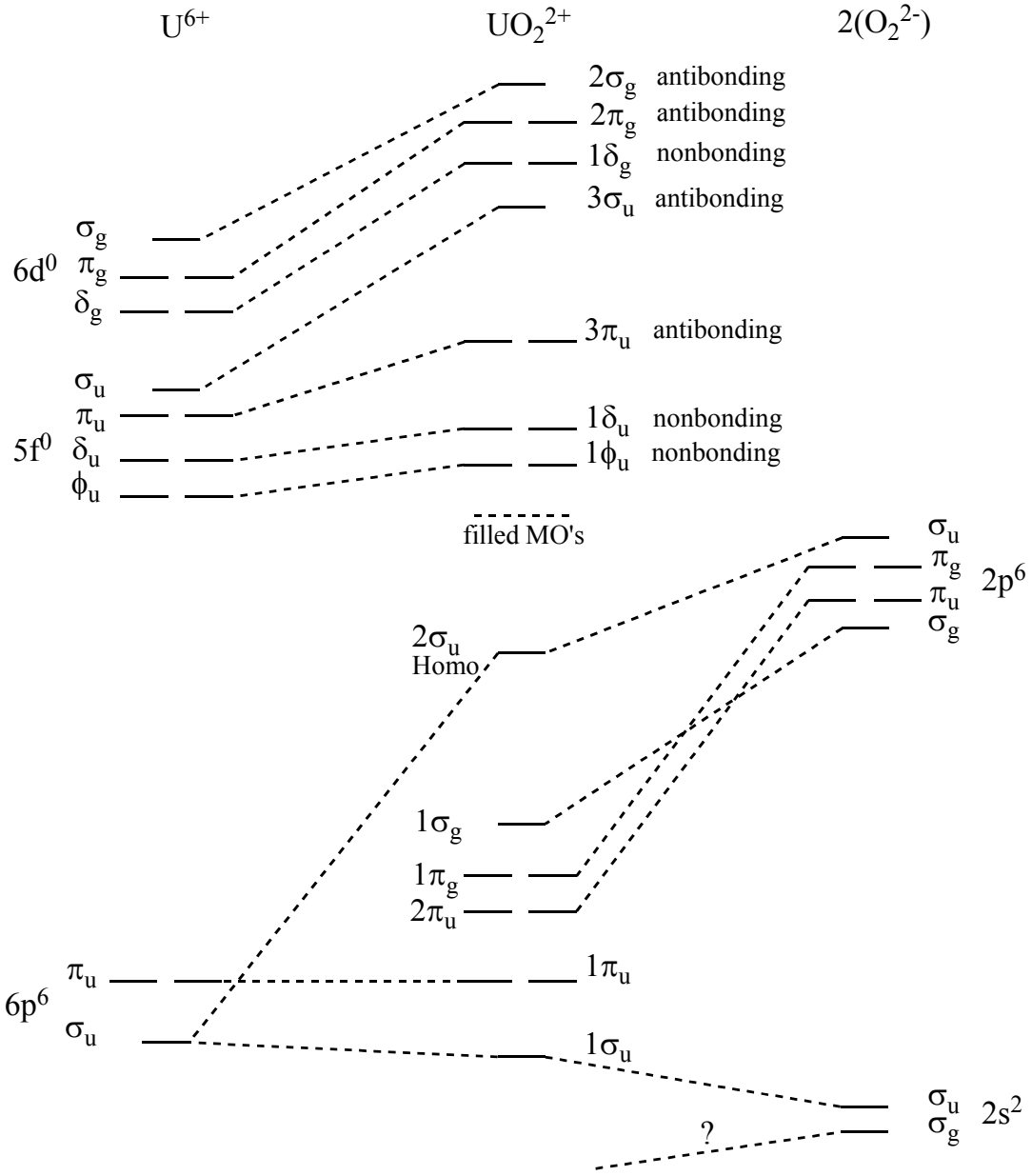

Under the ionic model MO diagram presented the $2\pi_u$ MO would be considered the most U-O bonding. The $2\sigma_u$ HOMO is much less stable, has less 2p character, and has the least U-O bonding compared to the other three bonding orbitals. All three of these features are thought to be due to the admixture of the U 6p(σ_u) semicore atomic orbital [23].

One potential scenario for the make-up of the partial triple bond of the actinyl unit is the following combination of three symmetry–allowed bond formations: 1.) O($2p_y$) to An($6d_{yz}$) with π_g anti-bonding symmetry, 2.) O($2p_y$) to An($5f_{yz}2$) with π_u non-bonding symmetry, and 3.) O($2p_z$) to An $5f_z^3$ with σ_u bonding symmetry [23] .

Orbitals in the equatorial plane, not utilized by the actinyl oxygens, typically are viewed as acceptors to weak σ–donor ligands. Such U ligand MOs as 6d(x^2-y^2), 6d(xy), 5f(x^3-$3xy^2$), and 5f(y^3-$3x^2y$), and to a smaller degree the 7s and 7p MOs are also thought to play a role [23].

However, a DFT analysis of $UO_2(H_2O)_5^{2+}$ [27] reveals that the UO_2^{2+} bonding picture is of a much more covalent nature with atomic orbital occupations of $2s^{1.94}2p^{4.32}$ for oxygen and $5f^{2.71}6d^{1.26}7s^{0.21}7p^{0.16}$ for uranium. As such, modifications must be made to the ionic model to account for this covalency. Also, once spin-orbit effects are properly incorporated one can see why there has been, and continues to be, difficulty in finalizing a more accurate MO diagram for uranyl and its actinyl counterparts.

1.3.3 Early Actinides and Actinyls in Aqueous Solution

Aqueous actinide cations exist in several oxidation states (+2 to +7), with tri–, tetra–, penta–, and hexavalent structures being most common. In acidic aqueous solutions of pH < 3, four structural forms of actinide cations can typically be identified: An^{3+}, An^{4+}, AnO_2^{+}, and AnO_2^{2+}. The bare cations An^{3+} and An^{4+} have a strong tendency for solvation, hydrolysis, and polymerization, whereas the more oxidized actinides are often quickly oxygenated to form actinyl cations. Uranium predominantly exists in solution as the uranyl dication $U^{VI}O_2^{2+}$, neptunium as the neptunyl cation $Np^{V}O_2^{+}$, and plutonium as the neutral plutonyl $Pu^{IV}O_2$.

Considered to be hard Lewis acids the early actinides tend to have a strong affinity for oxygen and fluorine atoms, hard donor ligands, and for this reason few ligands are able to compete with water once hydrated actinyl complexes form. In most cases water molecules bind directly to the metal cation to form an inner-sphere complex ion.

1.3.4 Early Actinides and Actinyls in Nonaqueous Solutions

In transitioning from aquaeous to nonaqueous solvents variations are often seen in the relative stabilities of the actinide oxidation states and the types of complexes formed with actinide and actinyl cations in these states. However, the fundamental principles

governing their redox reactions and their complexing abilities are typically the same regardless of the solvent used [1].

Three factors are important for actinides and actinyls in nonaqueous solvents: (1) the formation of neutral cation–anion pairs is often dominant due to the lower dielectric constants of mostly organic solvents, (2) conditions allow for complex formation between actinides and actinyls, and soft Lewis base ligands, such as those bound by nitrogen and sulfur, unlikely to have formed within an aqueous solution, (3) nonaqueous solvents are often useful for stabilizing redox–sensitive actinide and actinyl complexes with oxidation states that tend to be unstable in aqueous solutions.

CHAPTER TWO

GENERAL THEORY AND APPROXIMATION METHODS

Within electronic structure theory, we must use statistical quantum mechanics to describe electron motion within the charge distributions of molecules because electrons are so small. For lighter non-relativistic atoms this is generally accomplished by solving the time–independent electronic Schrödinger equation (2–1) [28].

$$H_e \Psi = E_e \Psi \tag{2–1}$$

There are two conceptually distinct approaches for determining the total electronic energy $E_e(\vec{R})$ equation (2–2) in a fixed electrostatic field of nuclei: the wave function approach and the density functional approach. Both are dependent on the Born–Oppenheimer approximation where the motion of the electrons is "decoupled" from that of their interacting nuclei.

$$E_e(\vec{R}) = E_k + E_{en} + E_{ee} \tag{2–2}$$

In equation (2–2), $\vec{R}$ represents the fixed nuclear coordinates, E_k the kinetic energy of the electrons, E_{en} the attractive interaction between the electrons and the nuclei, and E_{ee} the electron–electron repulsion energy.

In its simplest form, the many-electron wave function is approximated by a product of several one-electron wave functions. The motion of each electron is considered to be independent of the motion of all other electrons. The interactions between electrons are taken into account in an average way and are said to be uncorrelated, with each unaware of the positions of the other electrons at any given time. This approach is referred to as the Hartree–Fock (HF) approximation.

$$E_{HF}^{NR}\left(\vec{R}\right) = E_k + E_{en} + \left\langle E_{ee} \right\rangle_{Coul} + E_x \qquad \textbf{(2–3)}$$

In equation (2–3), $E_{HF}^{NR}\left(\vec{R}\right)$ represents the nonrelativistic (NR) HF energy, E_k the kinetic energy of the electrons, E_{en} the attractive interaction between the electrons and the nuclei, $\left\langle E_{ee} \right\rangle_{Coul}$ the averaged electron–electron Coulomb repulsion energy, and E_x the electron–electron exchange energy.

The self-consistent field solution (SCF) to the Hartree–Fock approximation is based on a revised Schrödinger equation—the Hartree–Fock equations—containing one-electron Hamiltonians represented by the Fock operator f_i^{HF} for each electron, see equation (2–4). The HF equations are obtained from equation (2–3) by way of the variational principle.

$$f_i^{HF}\psi(\vec{r}) = \varepsilon_i \psi(\vec{r}) \qquad \textbf{(2–4)}$$

The individual electrons are each described by molecular orbitals (MOs) $\psi(\vec{r})$ that have orbital energies ε_i. The MOs are a product of a spatial orbital and a spin function (α or β), which together are also known as spin–orbitals.

The variational procedure for obtaining self-consistent solutions to the HF Schrödinger equation begins with an initial guess at the total electronic density $\rho(\vec{r})$ equation (2–5) to solve for the MOs, and then the new MOs are used to obtain a new guess at the density.

$$\rho(\vec{r}) = \sum_i \left|\psi_i(\vec{r})\right|^2 \qquad \textbf{(2–5)}$$

This process is repeated until the current electron density agrees with the previous one to a certain predetermined degree of precision. In this manner one obtains the lowest energy for the single Slater determinant ground-state wave function.

The MOs are typically expanded as a finite basis set on each atomic centre composed of a radial part, a function of the distance from the nucleus, and an angular part, corresponding to the various angular momenta (s, p, d, f, g, etc…).

Although the HF method is known to obtain reasonably accurate geometries, energies involving a change in the number of paired electrons are poorly calculated, due to the failure to account for electron correlation. Several approaches have been developed to correct for this by accounting for the missing electron correlation and thereby

providing improved electronic energies. Among the popular techniques, which use the HF wave function as a starting point, are many-body perturbation theory, coupled-cluster theory, and configuration interaction (CI). Each of these methods yields more accurate results than the HF model alone, but they are computationally much more demanding, and as a result make obtaining accurate predictions for moderately large molecules of chemical interest difficult [27, 28].

2.1 Density Functional Theory

The 1998 Nobel Prize in Chemistry recipients John Pople and Walter Kohn were recognized for their respective participation to the convergence of the traditional quantum chemical techniques (Pople) with that of the relatively new density functional methodology (Kohn).

Advances in accurate and expedient quantum chemical calculations on inorganic and organometallic actinide molecules of reasonable size, has only recently become possible. Actinide chemistry in particular with its relatively unexplored f-element chemistry and inherent experimental challenges merits further computational investigation that often results in time savings for experimentalists [18, 21-24].

One of our aims is to test the abilities of DFT, and the many methods used in combination with it, at providing chemically accurate results. Only recently with advances in computing power and the growing acceptance of DFT methods, which incorporate electron correlation and relativistic effects, have computational chemical

investigations into intermediate size structures (containing greater than 15 non-hydrogen atoms) involving actinide elements become commonplace [27, 28].

The DFT approach replaces the search for an accurate many-electron wave function, which is a function of 3N electron coordinates, with that of the electron density, which depends on only three spatial coordinates. The DFT method often provides computational a time saving advantage over the HF wave function methods for molecular calculations of the same size and in turn allows DFT to be extended to larger molecules where the HF method, and particularly post-HF methods, become somewhat prohibited. However, there is one disadvantage of DFT, and that is that there is no systematic approach to improving the results towards an exact solution, unlike that for HF and post HF methods [27-29].

2.1.1 Nonrelativistic Total Energy

The conceptual foundation of DFT is the Hohenberg–Kohn theorem [30], which states that knowing the ground-state electronic density suffices in determining all the properties of a many-electron system. In the Kohn–Sham electronic–structure formulation of DFT [31], the NR electronic energy $E_{DFT}^{NR}\left(\vec{R}\right)$ is partitioned into three HF-like terms (E_k^{NI}, E_{en} and $\left\langle E_{ee}\right\rangle_{Coul}$) with everything else grouped into an electron–electron exchange–correlation energy E_{xc} term [27]:

$$E_{DFT}^{NR}\left(\vec{R}\right) = E_k^{NI} + E_{en} + \left\langle E_{ee} \right\rangle_{Coul} + E_{xc} \qquad \textbf{(2–6)}$$

With the E_k^{NI} term accounting for the kinetic energy of the non-interacting model system of the same density, and the remaining interacting kinetic energy being accounted for within the E_{xc} term.

With this ingenious and ground-breaking step, Kohn and Sham introduced the new concept of using a non-interacting reference system, with the exact same density as the real system, to account for almost all of the kinetic energy, instead of the exact amount accounted for by the Schrödinger equation. The remaining small amount of kinetic energy is then merged into the only unknown term in equation (2–6), E_{xc}. In order to solve for this term an appropriate method of approximation must be chosen.

The most commonly used approach to determining approximations for E_{xc} is to separate it into an exchange term E_x and a correlation term E_c, and approximate each of these terms separately.

$$E_{xc} = E_x + E_c \qquad \textbf{(2–7)}$$

Given an expression for E_{xc} one can formulate a one-electron Schrödinger equation (2–8) analogous to the HF equation (2–4). This allows us to use the well-established HF SCF technique.

$$\hat{f}^{KS}\varphi_i = \varepsilon_i\varphi_i \qquad \textbf{(2–8)}$$

2.1.2 Exchange–Correlation Functionals

For the purposes of this research we use in Priroda 5 (p5) [22, 24–27] and Amsterdam Density Functional (ADF) [32-35] softwares, the gradient corrected exchange–correlation (XC) functional PBE [29, 36], in which the XC energy E_{xc} depends on the local density and its gradient (first derivative). Also used in p5 and Gaussian 03 (g03) [61] is the hybrid density functional B3LYP [63–65] which combines a nonlocal Becke and exact exchange functional [37] with the Lee, Yang, and Parr correlation functional [38]. B3LYP is often found to yield additional accuracy improvements in bond energies (to that of PBE), while typically requiring more computational time.

2.1.3 Kohn–Sham Molecular Orbitals and Basis Set Expansion

Most implementations of Kohn–Sham (KS) density functional theory make use of the linear combination of atomic orbitals (LCAO) expansion of the KS molecular orbitals $\{\varphi_i\}$. With this approach a set of L predefined basis functions $\{\eta_\mu\}$ are used to linearly expand the KS orbitals as:

$$\varphi_i = \sum_{\mu=1}^{L} c_{\mu i}\eta_\mu \qquad \textbf{(2–9)}$$

If a complete set (i.e., $L = \infty$) were used then every function $\{\varphi_i\}$ could be expressed exactly using this equation. By using a truncated linear combination of predefined basis functions to express the KS orbitals, however, one reduces the optimization problem to a much simpler one.

Furthermore, by inserting equation (2–9) into equation (2–8) we obtain an equation (2–10), very similar to the HF case.

$$\hat{f}^{KS}(\vec{r}_1)\sum_{\nu=1}^{L} c_{\nu i}\eta_\nu(\vec{r}_1) = \varepsilon_i \sum_{\nu=1}^{L} c_{\nu i}\eta_\nu(\vec{r}_1) \qquad \textbf{(2–10)}$$

Two types of basis functions are used in this research. For g03 and p5 we use contracted Gaussian–type orbitals (GTO) combined into a contracted Gaussian function (CGF) of the form:

$$\eta^{GTO} = Nx^a y^b z^c e^{-\alpha r^2} \qquad \textbf{(2–11a)}$$

$$\eta_\tau^{CGF} = \sum_{a}^{A} d_{a\tau}\eta_a^{GTO} \qquad \textbf{(2–11b)}$$

Where N is the normalization factor; x, y, and z are the Cartesian coordinates; r is the radial spherical coordinate; a, b, and c are exponential values that sum to the angular quantum number l ; α is the orbital exponent which determines compactness (large) or diffuseness (small) of the function; and $d_{\alpha\tau}$ are the contraction coefficients.

In ADF Slater type orbitals (STO) are used:

$$\eta^{STO} = Nr^{n-1}e^{-\zeta r}Y_{lm}(\Theta,\phi) \qquad \textbf{(2–12)}$$

Where in addition to the terms described above Y_{lm} describes the angular spherical harmonics and ζ is the orbital exponent, and n, l and m are the quantum numbers [29].

Preference to the use of GTO functions is motivated by the computational advantages of multiplying two Gaussian functions to yield yet another Gaussian function, thereby leading to highly efficient computational algorithms. Whereas, STO functions physically describe the electron in the hydrogen atom correctly by exhibiting the correct cusp behavior as $r \rightarrow 0$ with a discontinuous derivative and the desired exponential decay of the tail region as $r \rightarrow \infty$ [60].

Both GTO and STO basis functions are used along with the two very similar basis sets selected for our computational calculations: the triple zeta valence polarized (TZP) basis set in ADF and the correlation-consistent polarized valence triple zeta (cc–pVTZ) basis set [39] in g03 and p5 [40].

2.1.3.1 Auxiliary Basis Set Expansion

The term resolution of identity (RI) is used to describe the time saving expansion of the Coulomb energy term using auxiliary basis sets. The RI approximation has been found to give an excellent approximation to the Coulomb energy at greatly reduced

computational costs. Almlöf et al. [41] were first to recognize the benefit of separating the calculation of the two-electron interaction into both a Coulomb and an exchange part. The theory behind the RI approximation method has been well reviewed by both Whitten [42] and Dunlap et al. [43], and has been implemented in numerous density functional codes.

Dmitri N. Laikov, author of the Priroda code, takes this expansion method a step further by not only expanding the Coulomb energy term but also the exchange–correlation energy term with auxiliary basis sets. Such an approach has been shown to be about an order of magnitude faster than the usual approximation to the Coulomb energy. Though there is some loss in accuracy, tests have shown that basis sets of moderate size, such as the ones we use, are sufficient to yield good accuracy for geometries and energies [44].

2.2 Relativistic Effects

In molecules containing heavy atoms the motion of the electrons must be treated relativistically because the effective velocity of the electrons, especially the inner core ones that penetrate closer to the nucleus, is non-negligible relative to the speed of light. Relativistic corrections are often found to be quite substantial. A primary relativistic stabilization effect, as a consequence of orbital orthogonality requirements, leads to the contraction of the 1s and higher s functions. The same effect is also seen, to a lesser degree, for the p electrons. A secondary effect arises from an increased shielding of the

nucleus by the stabilized outer core s and p electrons, which in turn leads to both destabilization and expansion of the valence d and f electrons [45]. As a rule of thumb, relativity has a noticeable effect on electronic levels and on calculated energies and bond lengths for elements beyond krypton (Z > 36) [27, 46].

In the very heavy actinide elements the relativistic expansion and destabilization of the valence 5f orbitals is sufficient to alter chemistry markedly in comparison with nonrelativistic analogues. These expansion and destabilization effects lead to weaker bond orbitals, and along with the larger range of oxidation states observed for the early actinides, can be traced to their tendency to form covalent bonds and hence their being more chemically active as compared to the 4f elements [45].

The Dirac Equation [47] is the starting point for most relativistic methods. Previously, with the use of the electronic Hamiltonian in NR theory, each molecular orbital is described as a scalar function associated with either spin up or spin down. However, in relativistic theory molecular orbitals are represented as four component spinors comprised of large (electronic) and small (positronic) components each having both up and down spins.

One important technique for separating the large and small component into a two component Hamiltonian called the Breit–Pauli Hamiltonian, equation (2–13), was developed by Foldy and Wouthuysen [48]:

$$H = H_{NR} + H_{mv} + H_D + H_{SO} \qquad \textbf{(2–13)}$$

Where the Hamiltonian terms represent, nonrelativistic, mass–velocity, equation (2–13a), Darwin, equation (2–13b), and spin–orbit coupling, equation (2–13c), respectively:

$$H_{mv} = \frac{-p^4}{8m^3c^2} \qquad \textbf{(2–13a)}$$

$$H_D = \frac{1}{8m^2c^2}\left(p^2 V_{ext}\right) \qquad \textbf{(2–13b)}$$

$$H_{SO} = \frac{1}{4c^2}\left(\nabla\left(V_N + V_{el}\right)\times \vec{p}\right)\bullet \vec{s} \qquad \textbf{(2–13c)}$$

The Hamitonian operators H_{mv} and H_D are corrections to the nonrelativistic kinetic and potential energy operators, respectively, and $V_{ext} = V_N + V_{el}$ where V_N is the nuclear potential and V_{el} is the electron potential of electron density. Also, ***p*** or $\vec{p}$ is the momentum operator, ***m*** is the electron mass, **c** is the velocity of light, and $\vec{S}$ is the spin angular momentum operator. All three equations are in atomic units [49].

However, one of the main difficulties with the Breit–Pauli Hamiltonian is that the operators are highly singular and therefore cannot be used variationally, thus leading to computational difficulties.

2.2.1 The Scalar Four–Component Method

Because the spin-free effects of the mass–velocity and Darwin terms dominate the relativistic corrections to electronic structure in many cases and because factoring out the spin–orbit term leads to a considerable reduction in computational effort it is advantageous to develop a spin-free relativistic Hamiltonian. The Priroda code uses such a method whereby starting from the full Dirac equation it applies a relativistic scalar four–component process in which all spin–orbit terms are separated from their scalar terms [40, 50] and neglected [40, 44, 51-53].

2.2.2 The Zero Order Regular Approximation (ZORA) Method

The zero order regular approximation (ZORA) [49, 54-56] relativistic calculation implemented in ADF is very similar in structure to a nonrelativistic one, having only a few additional terms in the Hamiltonian, equation (2–14) [33].

$$H_{ZORA} = \vec{\sigma} \cdot \vec{p} \frac{c^2}{2mc^2 - V} \vec{\sigma} \cdot \vec{p} + V$$

$$= \sum_i p_i \frac{c^2}{2mc^2 - V} p_i + \frac{mc^2}{\left(2mc^2 - V\right)^2} \vec{\sigma} \cdot \left(\nabla V \times \vec{p}\right) + V \qquad \textbf{(2–14)}$$

Spin-orbit effects accounted for in the second term of equation (2–14), where $\vec{\sigma}$ is the spin operator, can be either included or neglected depending on the circumstances. A key benefit of this method is that the mentioned singularities of the Breit-Pauli Hamiltonian, equation (2–13), are avoided.

2.2.3 Relativistic Effective Core Potentials (RECPs)

In the Schrödinger equation for a valence orbital the one-electron Hamiltonian, equation (2–15), includes the kinetic energy of the electron, the interactions of the nucleus, and the core electrons, as well as the interactions with the other valence electrons and the relativistic operator [27].

$$H = T + V_{core} + V_{nuc} + V_{rel} + V_{val} \qquad \textbf{(2–15)}$$

With the RECP, the Schrödinger equation (2–16) serves to replace the Coulomb effects of the inner core electrons, as well as the direct relativistic effects on the valence electrons. In general, RECPs can be used with either *ab initio* methods, including HF, or with DFT methods, to study molecules containing heavy elements. For the purposes of this research RECPs were used only with the density functional method.

$$H = T + V_{RECP} + V_{val} \qquad \textbf{(2–16)}$$

For our first case study we use the Stuttgart–Dresden small-core relativistic effective core potential (SC–ECP) of Küchle et al. [57].

2.2.4 Spin–Orbit Coupling

Spin–orbit effects are relativistic in origin (e.g. equations 2-13c and 2-14), but can be introduced in an *ad hoc* manner in nonrelativistic or quasi-relativistic situations and calculated as corrections after the electronic Schrödinger equation has been solved.

Spin–orbit effects can usually be ignored for determining geometry optimizations and bonding energies of closed-shell molecules, or for situations where the number of unpaired electrons remains constant and under these circumstances scalar relativistic calculations generally provide reasonably accurate results. However, accounting for spin–orbit effects for the majority open-shell molecules of the actinide and actinyl complexes being investigated is found to be necessary.

Of the two vector addition approaches to spin–orbit coupling, which account for the orbital and spin angular momenta within molecular structures, neither LS coupling (also referred to as Russell–Saunders coupling) nor j–j coupling, is found to completely describe these effects, within early actinides and their ions, properly. This is thought to be because the 5f orbitals are sensitive to their atomic or ionic environment and also because

spin–orbit coupling interactions are found to be energetically similar to interatomic repulsions within such complexes [45].

Spin-orbit effect calculations are not applied in our investigation of UN_4O_{12} complexes because we only work with uranium in its f^0 state. As for our study of polypyrrolic macrocycles, spin-orbit effect calculations are deemed necessary for the unrestricted spin states.

In addition, the calculation of redox potentials also utilize an *ad hoc* form to account for spin-orbit effects called the Hay correction [58]. Hay corrections are based on model spin-orbit configuration interaction (CI) calculations of the PuO_2^{n+} species, to account for multiplet and spin-orbit effects not included in the single-configuration DFT wave function.

2.3 Solvation Methods

2.3.1 COSMO and C–PCM

With a large portion of chemistry occurring within solution, the need to accurately model the significant effects of solute–solvent interactions on molecular energies, structures, and properties has become increasingly important.

The well-established polarizable continuum solvation models (PCMs) [4, 5] utilize a bulk solvent representative of a structureless polarizable medium characterized

by a dielectric constant (ε). The dielectric is polarizable and when perturbed by the solute a reaction field is generated.

Unlike the PCM models the conductor-like screening model (COSMO) [34, 59, 60] in ADF [32-35] and the conductor-like polarizable continuum model (C–PCM) [61] in Gaussian 03, approximate the dielectric medium with a scaled spherical conductor. This allows a vanishing total potential of an infinite conductor to be used as a relatively simple boundary condition.

Within these two very similar models the bulk solvent is treated as a dielectric medium that induces charge polarization on a solvent accessible surface (SAS) around the molecule immersed in solution. The solvent accessible surface is made up of a series of atomic–centered spheres that envelop the molecule forming a cavity [62]. Inside the cavity the solute is surrounded by the dielectric constant of a vacuum (ε_o), outside it takes on the value of the desired solvent (e.g., $\varepsilon = 38.2$ for CH_3NO_2 and $\varepsilon = 7.58$ for THF). The radii of the spheres are usually defined or chosen to be around 1.2 times that of Van der Waals atomic radii. The surface defining the spheres, are partitioned into surface triangles called tesserae (little tiles) with each triangle assigned an adjustable point charge. In the self-consistent reaction field (SCRF) procedure, the surface point charges are determined from the total charge density of the molecule [33].

2.4 Molecular Properties Investigated

Such molecular properties as the nature of bonding, relative Gibbs free energies, solvation energies, dipole moments, bond lengths, bond angles, bond orders, atomic charges, vibrational frequencies and metal coordinations are addressed and compared to experimental results where possible. Lastly, a determination of oxidation reduction (redox) potentials was made.

There are various methods of structural formation—radical and ionic are thought to be the most common—for the complexes we analyze in our two case studies. As for the nature of bonding it is often subject to interpretation and we therefore use descriptions such as covalent (based on bond multiplicity), mixed covalent/ionic, and ionic (based on atomic charges). However, this is done in a relative sense rather than an absolute one, with the use of qualifying terms such as mostly, predominantly, and weakly often necessary to clarify such descriptions. Furthermore, in order to answer certain questions regarding our aims or goals, we analyze specific atomic pairings which provide information unique to the structure, as well as identifying distinguishing features potentially helpful to experimental identification.

Relative Gibbs free energies and solvation energies are mostly used to provide relative stability information on the many structures analyzed in gas–phase and solution.

Calculations of dipole moments, bond lengths, bond angles, bond orders, atomic charges, and vibrational frequencies are typically built into the variety of computational software packages available including the ones we use. We chose to use Mayer bond

orders [64, 65] and Hirshfeld atomic charges [66] for both of our case studies and further details of these methods are discussed below.

Harmonic vibrational frequencies were calculated to obtain thermochemistry data, such as Gibbs free energies and corrections, to verify the nature of stationary points of optimized geometries, and offer helpful comparisons for experimental identification. For example, higher frequency vibrations are usually proportional measures of bond strength increases and bond length decreases.

Metal coordination is another common identifying feature and in our second case study it is also used to determine octahedral versus tetrahedral high and low spin states of the 3d transition metals used.

Redox potentials are further used to describe the tendency of a chemical species to gain or lose electrons. Common experimental methods of measuring redox potentials are cyclic voltammetry and spectrophotometry combined with pulse radiolysis [1]. The redox chemistry of the early actinides is quite diverse due to the accessibility of higher oxidation states [67].

2.4.1 Mayer Bond Orders

The Mayer bond order [64, 65] provides us with a method of summing all the electron density contributions to the bond. A substantial computational advantage arises in larger compounds with little or no symmetry, because the large number of orbital

interactions arising between the two atomic centres of a bond often restricts analysis to only the high-lying occupied and low-lying virtual orbitals.

The Mayer bond order between atoms *A* and *B* is given by equation (2–17), where $\boldsymbol{P}$ is known as the density matrix and $\boldsymbol{S}$ as the atomic orbital overlap matrix.

$$B_{AB}^{Mayer} = \sum_{s}^{onA} \sum_{t}^{onB} (PS)_{st} (PS)_{ts} \qquad \textbf{(2–17)}$$

Bond orders of this type have similar basis set dependence as Mulliken population analysis [68] on which it is based. The off-diagonal elements of $\boldsymbol{PS}$ are known as the Mulliken overlap populations. Because of this, comparison between different systems is only valid when analogous basis sets are used.

2.4.2 Hirshfeld Atomic Charges

Further insight into bonding and reactivity can be gained by computing individual effective charges on the atoms of a molecular complex. It is, however, important to be aware that atomic charges have some degree of arbitrariness to them and are primarily meaningful in comparison of trends where such effects as basis set variation are greatly reduced. Both the Priroda and ADF implementations used support Hirshfeld charge calculations [66].

The Hirshfeld charge on an atom *A* is defined as the integral of the charge density weighted by the relative contribution, at each point in space, of the initial unperturbed charge density of that atom, equation (2–18):

$$Q_A^{Hirshfeld} = Z_A - \int \rho(\vec{r}) \frac{\rho_A(\vec{r})}{\sum_B \rho_B(\vec{r})} d\vec{r} \qquad \textbf{(2–18)}$$

CHAPTER THREE

DENSITY FUNCTIONAL STUDY OF THE VARIOUS FORMS OF UN_4O_{12} CONTAINING URANYL NITRATE

3.1 Introduction

Often the topics of computational research papers are based on existing chemical structures discovered through experimental investigations by either trial and error methods or by the unexpected chance of recognizing something unusual and exploring it further. It seems that a reversal of this process may now be possible with computational chemistry becoming poised to supply experimental chemists with alternatives for exploring new chemistry or for predicting the existence of new structures. Actinide chemistry in particular with its relatively unexplored f-element chemistry and inherent experimental challenges currently merits further investigation, and computational chemistry now offers unique advantages that can often result in time savings for experimentalists [18, 21-24].

Hexavalent uranium is known to exist most often in aqueous environments as the uranyl dication [2, 25, 45] UO_2^{2+} and is thought to combine with nitrates, when they are made available, to form the neutral complex uranyl nitrate, $UO_2(NO_3)_2$, or one of its hydrated forms $UO_2(NO_3)_2{\cdot}6H_2O$, $UO_2(NO_3)_2{\cdot}3H_2O$, or $UO_2(NO_3)_2{\cdot}2H_2O$ [69-71]. Uranyl nitrate is considered to be the most abundant salt found in the reprocessing of spent nuclear fuel [72].

Pasilis et al. [73] recently used electrospray ionization (ESI) and Fourier transform ion–cyclotron resonance mass spectrometry (FT–ICR–MS) to analyze the ions generated from uranyl nitrate solutions. In particular, with a negative ion ESI–MS of a 95:5 CH_3OH/H_2O solution, the three most intense peaks were assigned to $[UO_2(O)(NO_3)_2]^-$, $[UO_2(O)(NO_3)]^-$, and $[UO_2(NO_3)_3]^-$, respectively. In the first of these gas-phase ions O^{2-} is thought to undergo oxidation to O^-. Furthermore, the third ion is identical to that of trinitratouranylate, known to form in ketones, ethers, and alcoholic solvents and is an indication of competition between solvent and nitrate molecules for ligand coordination positions to uranyl in solution [74].

In the crystal structures of $K[UO_2(NO_3)_3]$, $Rb[UO_2(NO_3)_3]$, and $Cs[UO_2(NO_3)_3]$ each nitrate is found to chelate bidentately to uranyl, forming a hexagonal bipyramid around uranium [75]. The coordination of the complex ion $[UO_2(NO_3)_3]^-$ is thought to be similar in the gas phase [73].

Furthermore, the possibility of various ionic or radical nitrogen oxides (N_xO_y) and oxoions (N_2O, NO^-, NO, $(NO)_2$, N_2O_3, NO^+, NO_2^-, NO_2, N_2O_4, N_2O_5, NO_2^+, and NO_3^-) combining with $UO_2(NO_3)_2$ leads to a multitude of diverse structural possibilities occuring in equilibrium. Due to their environmental role in the chemistry of the Earth's troposphere and stratosphere and their links to ozone depletion and smog formation, nitrogen oxides have been the subject of considerable theoretical and experimental work over the past decade. Nitrogen oxides, often cited as NO_x, are produced when fossil fuels are burned and constitute a large portion of industrial pollution. The photodissociation of N_2O_4, for example, has aroused particular interest in atmospheric chemistry [79]. As well, interactions between water and N_xO_y species in condensed phases also play an important

role in atmospheric chemistry. In this instance N_2O_5 has been implicated in stratospheric ozone depletion [80-82].

The idea of computationally investigating the structural forms of UN_4O_{12} containing uranyl nitrate was prompted by a recent paper by Crawford and Mayer [83]. The authors make reference to the importance of establishing whether the uranium (VI) species of UN_4O_{12} takes on the form of an ionic or covalent compound in solution. They go on to point out how conflicting evidence for two structural forms of UN_4O_{12} appear in the research literature. The most commonly cited form is an adduct of uranyl nitrate and dinitrogen tetroxide, $UO_2(NO_3)_2 \cdot N_2O_4$, whose thermal decomposition leads to the formation of the important precursor anhydrous uranyl nitrate. The hydrated complex, $UO_2(NO_3)_2 \cdot 6H_2O$, is one of the most important compounds of the plutonium uranium recovery by extraction (PUREX) process for the separation of fission products from uranium and plutonium fuels and a main wastewater pollutant [2]. The second most cited form is the nitrosonium salt, $NO^+UO_2(NO_3)_3^-$. They were able to experimentally obtain crystallization of this salt. By deposition of uranium metal turnings in a 30:70 nitromethane/dinitrogen tetroxide (CH_3NO_2/N_2O_4) solution under anhydrous conditions a precipitate was obtained from a saturated solution at –28 °C [84].

Nitrosonium salt structures of similar form also include the previously investigated nitrosonium nitratometallates: $NO[Cu(NO_3)_3]$ [19], $NO[Co(NO_3)_3]$ [76], $NO[Ni(NO_3)_3]$ [77] and $NO[Mn(NO_3)_3]$ [78].

The present computational work was undertaken with the aim of establishing, if possible, the UN_4O_{12} structure or structures containing uranyl nitrate most likely to exist and predominate in either an inert gas or a nonaqueous solution environment. As a

broader goal we look to show that a computational density functional (DFT) [29] investigation into isomers of UN_4O_{12} can provide experimentalists with a valuable list of potential structural candidates for identification. An analysis of selected structures based on relative Gibbs free energies is made to identify distinguishing features that could be potentially helpful to experimental identification. Such molecular properties as the nature of bonding, relative Gibbs free energies, dipole moments, bond lengths and angles, bond orders, atomic charges, frequencies, and metal coordination are addressed and compared to experimental results where possible.

3.2 Computational Methods

Gas-phase calculations were performed with Priroda–5 (p5) [40, 44, 51-53] and Gaussian03 (g03) [85]. All calculations used DFT with either the pure generalized gradient approximation (GGA) [58] functional PBE [36] of Perdew, Burke and Ernzerhof or the hybrid B3LYP exchange–correlation (XC) functional [37, 38, 86]. B3LYP combines a nonlocal Becke and exact exchange functional [37] with the Lee, Yang and Parr correlation functional [38]. Vibrational frequencies were calculated to obtain thermochemistry data, such as Gibbs free energies and corrections, and to verify the nature of stationary points of optimized geometries. All p5 calculations used correlation-consistent polarized valence triple–ζ (cc–pVTZ) basis sets [29]. As for g03, we used the cc–pVTZ basis set for nitrogen and oxygen and the Stuttgart–Dresden "small–core" effective core potential SC–ECP [57] basis set for uranium.

Our experience has shown that the use of pure GGA functionals yield reasonable calculation times while providing accurate geometry optimizations and reliable self-consistent field (SCF) convergences [87-89]. Frequency calculations using p5 PBE were then performed on the gas-phase p5 PBE optimized geometries to verify that no imaginary frequencies were present. Gibbs free energy corrections were obtained with these frequency calculations. B3LYP has been shown to be more accurate than PBE for the calculation of Gibbs free energies [87, 90], but due to the costs of running B3LYP optimizations, we chose to add the p5 PBE gas-phase Gibbs free energy corrections to B3LYP single-point energy results obtained for both p5 and g03 before calculating relative Gibbs free energies from them. In Gaussian, an "ultrafine" integration grid, and a "tight" SCF convergence criteria were used to obtain single-point SCF energies. Although this method is less than ideal, our test calculations showed that this time-saving procedure provides a good approximation for the comparison of relative Gibbs free energies.

To approximate relativistic effects in Gaussian we chose to use SC–ECPs [57] rather than "large core" (LC–ECPs) ones. Recently, SC–ECPs have been shown to give a much closer agreement with experiment for a number of molecular properties, including geometries [87, 91, 92], vibrational frequencies [91, 92], and NMR chemical shifts [58, 90, 93, 94]. Batista et al. [90], have shown that the use of SC–ECPs, along with the hybrid B3LYP [37, 38, 86] XC functional, give excellent results for the geometries, vibrations, and first bond dissociation energies of UF_6. In Gaussian, relativistic effects were included by replacing the core electrons of uranium with a Stuttgart–Dresden SC–ECP according to Küchle et al. [57]. The Stuttgart–Dresden SC–ECP treats 60 electrons

as the core and the remaining electrons as part of the variational valence space. Priroda applies a relativistic scalar four–component process, where all spin–orbit terms are separated from their scalar terms [40, 50] and neglected [40, 44, 51-53]. For geometries and frequencies, neglecting spin–orbit effects is generally accepted to be a valid approach. In previous studies of these relativistic methods it was found that g03 SC–ECP (60e) and Priroda's scalar four–component method were of comparable quality [87-89].

Modeling such chemical structures in solution requires the use of accurate solvation methods. The solid-state crystals isolated [83] were found to react with both water, leading to the vigorous liberation of gaseous NO_2. In fact, it was determined to be so sensitive that it was deemed necessary to handle it under an inert atmosphere. We therefore chose to perform our solvation calculations with the aprotic polar solvent nitromethane (dielectric constant $\varepsilon = 38.2$). Relative Gibbs free energies using this solvent were found to be very similar to those found using water as a solvent. Accurate solvated Gibbs free energy differences were obtained with single-point calculations of p5 PBE gas-phase optimized geometries using g03 B3LYP SC–ECPs and the conductor polarized continuum model (C–PCM) [61]. As well, using the Gibbs free energy corrections obtained from the p5 PBE gas-phase frequency results to calculate the relative solvated Gibbs free energies provided an accurate alternative to running costly g03 solvated frequency calculations.

Although common, the use of single-point calculations on gas-phase optimized geometries is not considered to be the optimal method for obtaining solution-phase Gibbs free energies. A preferable method of obtaining Gibbs free energies would be to reoptimize the gas-phase geometries in solution. Efforts were made toward this using the

Amsterdam density functional (ADF) [32, 33, 35] software with the scalar relativistic ZORA [49, 54-56] method, the TZP basis set made up of Slater–type orbitals (STOs) and the conductor-like screening model (COSMO) [34, 59, 60]. For ADF/COSMO calculations we used the Klamt atomic radii of 1.72 Å for oxygen and 1.83 Å for nitrogen [59] and an atomic radius of 1.70 Å for the uranium atom [88, 89, 95]. Due to problems with numerical noise and despite several attempts, only three of 22 isomers were found to converge to a stationary point without any imaginary frequencies. Combinations of ADF integration accuracy values and geometry gradient convergence criteria of 4.0/1 x 10^{-2}, 5.5/1 x 10^{-3}, and 6.5/1 x 10^{-3} (over 22 UN_4O_{12} isomers were calculated with this last combination) were tried and found to provide similar results for imaginary frequencies (ranging from 9i to 533i in multiples of 1–4 per isomer) with no apparent advantages. We therefore chose not to pursue geometry optimizations in solution any further.

Gas- and solution-phase calculations were also performed to obtain the relative Gibbs free energies of 13 N_2O_4 isomers to discuss their relative stabilities and geometries. Relativistic methods were not necessary and we chose to use g03 B3LYP/cc–pVTZ in the gas phase and g03 B3LYP/cc–pVTZ/CPCM in solution for geometry optimizations and frequency calculations.

All molecular species calculated with uranium considered it to be in the U^{VI} oxidation state with an f^0 valency, and therefore all calculations were done with a restricted, closed-shell, Kohn–Sham formalism. Due to the radical nature of some of the N_2O_4 isomers and the UN_4O_{12} isomers containing them as components, the use of a restricted, closed-shell formalism may not model some of the higher-energy structures effectively.

3.3 Results and Discussion

The proceeding sections are organized as follows: Subsection **3.3.1** outlines and discusses the characteristics of the key structural components found to make up the UN_4O_{12} isomers containing uranyl nitrate, subsection **3.3.2** discusses how 73 identified UN_4O_{12} isomers containing uranyl nitrate are classified into three categories and 19 types, subsection **3.3.3** gives a general analysis and discussion of 22 select gas- and solution-phase UN_4O_{12} isomers containing uranyl nitrate, and subsection **3.3.4** provides a detailed by-type discussion of these isomers for the two categories and six types that were found to be represented. Finally, in subsection **3.3.5**, we look briefly at the possibility of dissociation of UN_4O_{12}.

With some exceptions (for example, isomers **a1–a3**, **a7**, and **a9**) the p5 PBE gas-phase relative Gibbs free energy calculations were found to be significantly different in comparison to both the p5 and the g03 B3LYP single-point results (Table 3–1). Moreover, hybrid functionals such as B3LYP have been shown provide better results to those of GGAs (such as PBE) for the energetics of actinide species [87, 90, 91]. With the two sets of B3LYP results being very similar, with a few possible exceptions such as **b1–b4,** we arbitrarily chose to use the p5 B3LYP single-point results for the stability ordering of the UN_4O_{12} isomers containing uranyl nitrate in the gas phase.

Table 3–1. Calculated gas- and solution-phase single-point relative Gibbs free energies and absolute Gibbs free energy differences between gas- and solution-phase ΔG_{solv} of 30 selected UN_4O_{12} isomers (in kcal/mol)

Isomers	p5 PBE	p5 B3LYP	g03 B3LYP	g03 C–PCM B3LYP (p5)	
	G_{gas}^{rel}	G_{gas}^{rel}	G_{gas}^{rel}	G_{sol}^{rel}	ΔG_{solv}
a6	8.2	2.5	3.0	0.0	–21.2
a5	8.6	2.4	3.3	1.1	–20.3
a8	7.0	2.6	3.6	2.2	–19.5
a1	0.0	0.0	0.0	3.6	–14.5
a27	19.3	18.5	17.8	4.5	–31.5
a2	1.0	0.2	–0.2	5.2	–12.8
a13	8.7	4.5	4.4	5.6	–17.0
a10	9.9	3.0	3.3	6.0	–15.4
a14	8.5	4.5	4.6	6.3	–16.5
a7	2.2	2.5	2.7	6.8	–14.7
a9	2.6	2.9	3.0	6.8	–18.3
a4	7.9	2.1	2.5	7.4	–17.0
a16	11.9	5.5	5.6	7.6	–20.6
b6	19.2	15.7	15.5	8.2	–31.1
b2	6.5	1.7	3.8	8.2	–13.8
b1	3.9	1.4	4.2	8.8	–13.5
a3	1.5	1.2	0.9	9.0	–14.0
a12	9.5	4.1	4.8	9.1	–17.5
b3	5.3	2.6	5.5	9.6	–19.1
a11	8.7	3.7	4.4	10.0	–15.5
b4	5.9	3.6	6.1	10.4	–20.1
a15	11.6	4.8	4.7	10.4	–18.4
a17	9.5	7.0	9.6	14.9	–24.6
a18	8.5	8.6	8.7	14.9	–16.2
a20	15.5	12.5	12.4	16.9	–15.6
a19	9.4	9.3	9.9	17.8	–11.9
a21	15.6	13.0	13.1	18.2	–15.5
b5	11.7	11.1	14.3	21.0	–11.4
c1	16.9	19.1	22.2	32.0	–22.6
b7	20.4	23.7	27.5	38.6	–11.2

Thirty of the gas-phase optimized isomers with the lowest relative Gibbs free energies within each category were then chosen to calculate single–point solvated relative Gibbs free energies. The 22 lowest relative Gibbs free energy structures found in solution were then selected for detailed analysis and discussion.

Several other gas-phase isomers of UN_4O_{12} that do not contain uranyl nitrate were also identified. The most prominent one, $U(NO_3)_4$ with the formal oxidation state for uranium of IV, is as yet undiscovered, as far as we can determine [96]. However, previous experimental attempts have shown that $U(NO_3)_4$ may exist in solution but was found to oxidize spontaneously to a U^{VI} complex before being isolated [97]. Our calculations show that $U(NO_3)_4$ has a gas-phase Gibbs free energy of 34.6 kcal/mol relative to our chosen reference **a1**. This high relative energy could explain the difficulty in isolating this isomer in experimental investigations. The most stable of the remaining isomers had a relative gas-phase Gibbs free energy of 62.1 kcal/mol. Consequently these isomers were not investigated any further.

3.3.1 The Structural Components

A diverse assortment of nitrogen oxoions and oxides, along with dioxygen and superoxide were found to bind with uranyl nitrate to yield the large number of computationally stable UN_4O_{12} isomers. Many nitrogen oxides are commonly found in both ionic and radical forms. All of them contain some form of resonance hybrid/multiple bonding structure. Some of the most commonly encountered oxoions and oxides of nitrogen are NO^+, NO_2^+, NO_2^-, NO_3^-, NO, NO_2, N_2O_3, N_2O_4, and N_2O_5, with formal oxidation numbers for nitrogen ranging from +2 to +5. Other less commonly encountered forms are *cis*– and *trans*–ONOO and $ONOO^-$, the NO_3 radical, and other isomers of

N_2O_3, N_2O_4, and N_2O_5 (Figures 3–1 and 3–2) [98, 99]. The paper by Laane and Ohlsen [100] provides a good preliminary overview of the N_xO_y species.

The majority of the bond lengths in Figure 3–1 are experimental, taken from one of the following references [99, 101]. The exceptions are: (1) the uranyl **1** bond length which is a calculated value using the Stuttgart SC–ECP (60 e) for uranium and the TZVP (DFT/B3LYP) basis set for oxygen and nitrogen [102, 103], (2) the uranyl nitrate **2** bond lengths which were calculated using the Stuttgart SC–ECP (60 e) for uranium and the TZVP (DFT/SVWN) basis set for oxygen and nitrogen [102, 103], (SVWN combines a Slater exchange functional [104] with the Vosko, Wilk, and Nusair correlation functional [105]), and (3) the peroxynitrites **12**–**15** which are CCSD(T) calculated values [106].

In the following paragraphs a more detailed discussion of the various N_2O_4 structural forms is provided along with a brief review of some of the known chemistry of N_2O_4. The structural components of Figure 3–1 are discussed in the Appendix.

Figure 3–1. Structural components: **1**, uranyl dication; **2**, uranyl nitrate; **3**, dioxygen; **4**, superoxide anion; **5**, nitric oxide radical; **6**, nitrosonium (nitrosyl) cation; **7**, nitrogen dioxide radical; **8**, nitrite anion; **9**, nitronium (nitryl) cation; **10**, nitrate radical; **11**, nitrate anion; **12** and **13**, *cis*– and *trans*–peroxynitrite radical; **14** and **15**, *cis*– and *trans*–peroxynitrite anion; **16**, dinitrogen trioxide; **29**, dinitrogen pentoxide (Bond lengths are given in angstroms, and angles in degrees; see the text.)

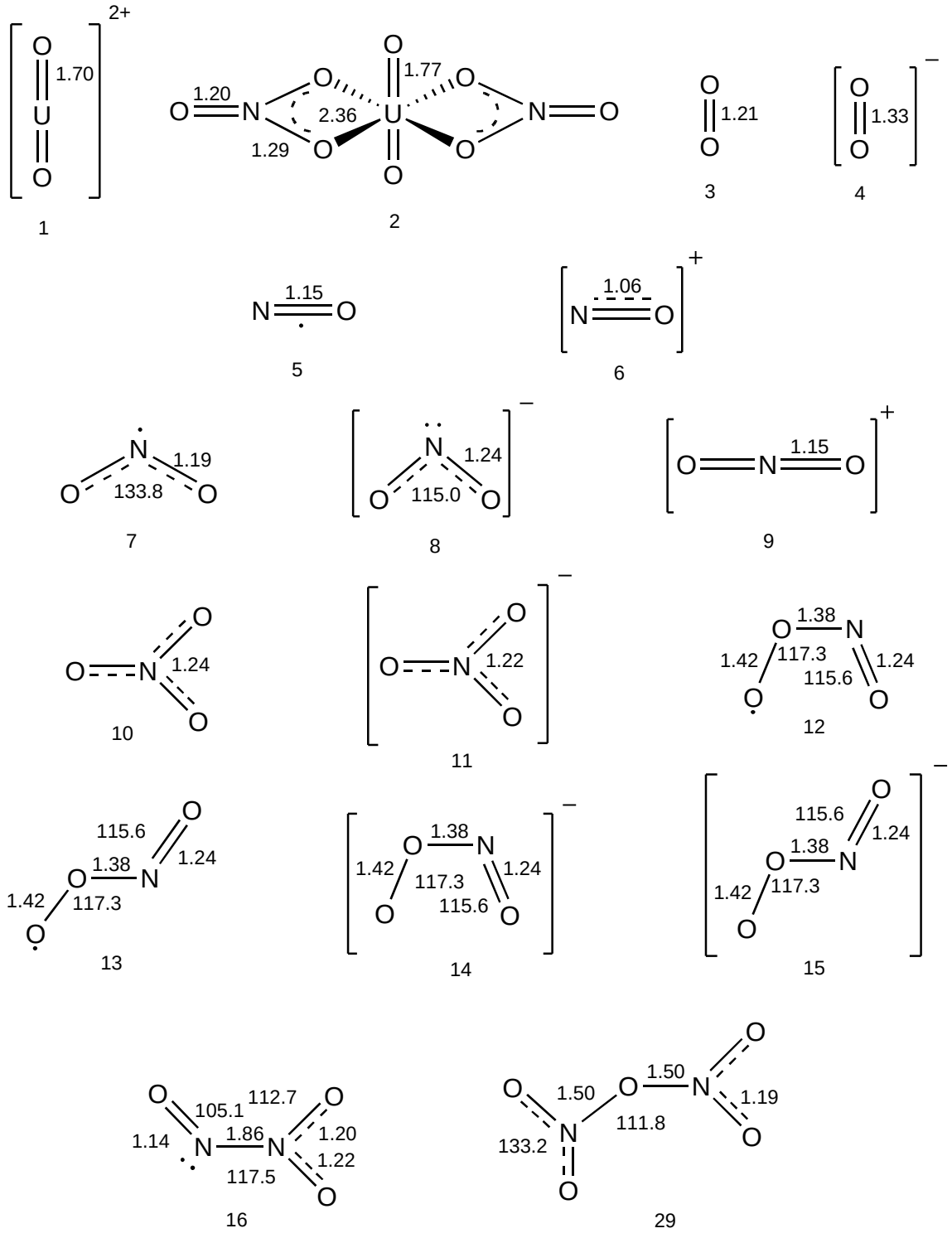

The ordering of the various N_2O_4 isomers shown in Figure 3–2 is based on our relative Gibbs free energy calculations with g03 B3LYP/cc–pVTZ/C–PCM using a nitromethane solvent, Table 3–2.

Table 3–2. Calculated gas- and solution-phase optimized relative Gibbs free energies of free dinitrogen tetroxide isomers[a]

N_2O_4 Isomers		g03 B3LYP cc–pVTZ	g03 C–PCM B3LYP cc–pVTZ	g98 B3LYP 6–311G* CBS–QB3[b]
		G^{rel}_{gas}	G^{rel}_{sol}	E^{rel}_{gas}
sym–N_2O_4	**17**	0.0	0.0	0.0
cis–ON·O·NO_2	**18s**		5.7	
twist–ON·O·NO_2	**18g**	11.9		
trans–ON·O·NO_2	**19**	(10.3)	7.0	3.4
ON·O_2NO	**20**	11.8	7.6	
perp–ON·O·NO_2	**21**	11.6	11.8	7.4
$NO^+NO_3^-$	**22**	33.0	18.3	
NO_2·O_2N	**23**	(22.0)	23.1	13.4
cis,cis–ON·OO·NO	**24**	30.8	30.3	24.0
cis,trans–ON·OO·NO	**25**	32.3	34.3	25.8
trans,trans–ON·OO·NO	**26**	33.8	36.6	31.4
cis,cis–OO·$(NO)_2$	**27**	48.3	47.2	
trans,trans–OO·$(NO)_2$	**28**	66.3	60.7	

[a]The bracketed values were determined to have a single imaginary frequency indicative of their being transition states (kcal/mol). [b]Reference [100, 107].

The nature of each stationary point was verified for 12 of 13 structures in solution (**18g** was stable only in the gas phase). The order of the gas-phase relative Gibbs free energies of these isomers using g03 B3LYP/cc–pVTZ was determined to be **17**, **21**, **20**, **18g**, **22**, and **24**–**28** with **19** and **23** found to be transition states with single imaginary frequencies. However, recent gas-phase calculations by Olson et al. [107] using g98 B3LYP/6–311G* (without zero-point energy corrections) and CBS–QB3 found the order to be **17**, **19**, **21**, and **23**–**26** with **18g**, **20**, **22**, **27**, and **28** unconsidered. Calculated

structural parameters (g03 B3LYP/cc–pVTZ, gas phase) for all 13 structures can be found in Figure 3–2.

Figure 3–2. Thirteen isomers of dinitrogen tetroxide, N_2O_4: **17**, sym–N_2O_4; **18s**, *cis*–$ON{\cdot}O{\cdot}NO_2$; **18g**, twist–$ON{\cdot}O{\cdot}NO_2$; **19**, *trans*–$ON{\cdot}O{\cdot}NO_2$; **20**, $ON{\cdot}O_2NO$; **21**, perp–$ON{\cdot}O{\cdot}NO_2$; **22**, $NO^+NO_3^-$; **23**, $NO_2{\cdot}O_2N$; **24**, *cis,cis*–$ON{\cdot}OO{\cdot}NO$; **25**, *cis,trans*–$ON{\cdot}OO{\cdot}NO$; **26**, *trans,trans*–$ON{\cdot}OO{\cdot}NO$; **27**, *cis,cis*–$OO{\cdot}(NO)_2$; **28**, *trans,trans*–$OO{\cdot}(NO)_2$. (Bond lengths are given in angstroms, and angles in degrees. These are g03 B3LYP/cc–pVTZ gas phase values; see the text)

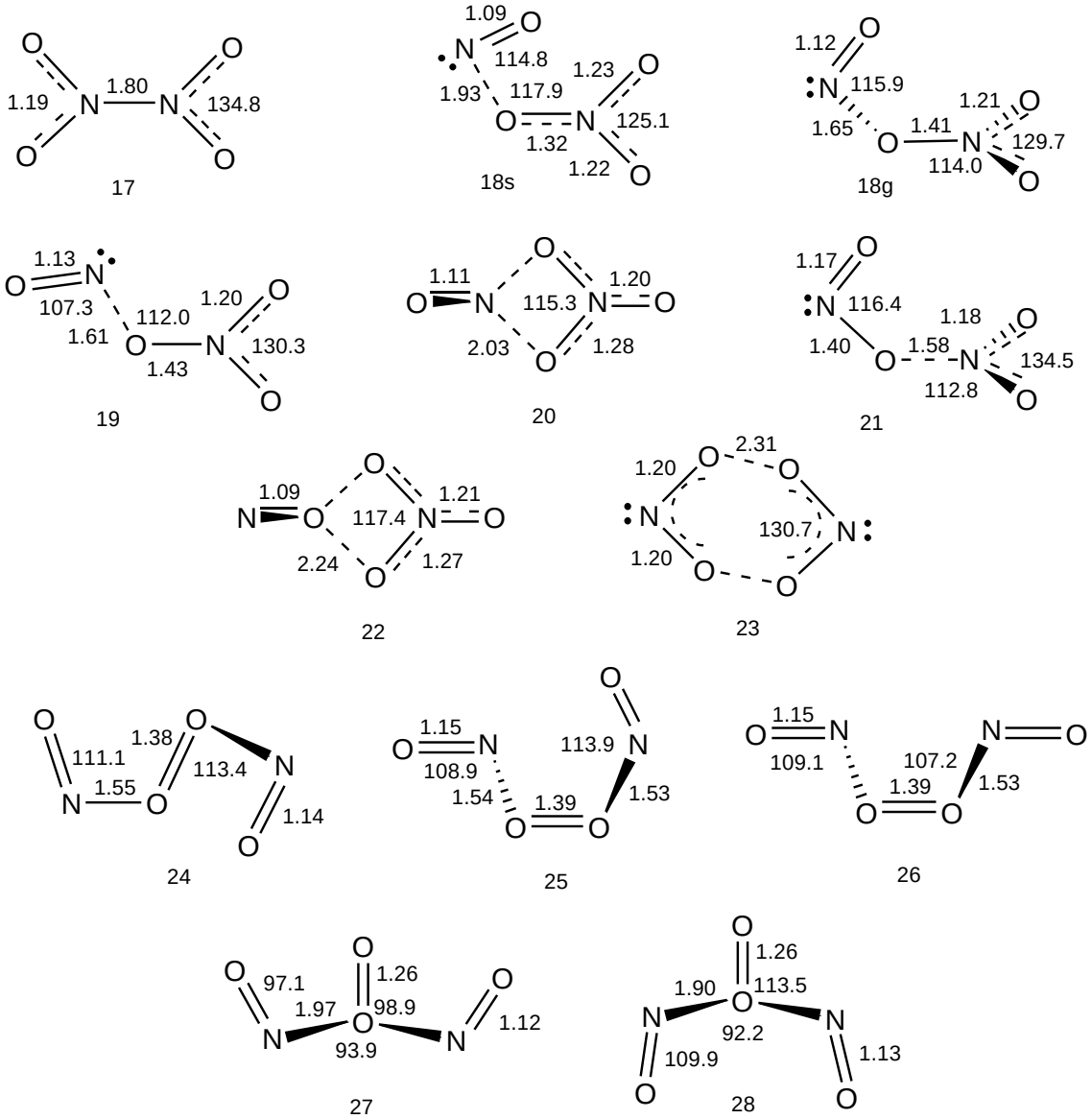

Two NO_2 radicals are thought to dimerize reversibly at low temperatures to the most common sym–N_2O_4 ($O_2N{\cdot}NO_2$) isomer **17**, Figure 3–2, of D_{2h} symmetry (reaction 3–1) [101]. It is thought that the odd electron delocalizes to a π–antibonding orbital. The similarity between N_2O_4 and NO_2, with the same N=O bond length of 1.19 Å and ONO angles of 135.4° and 133.8°, respectively, along with the longer than ordinary N–N bond distance of 1.78 Å, supports the notion that sym–N_2O_4 is formed by a weakly bound pair of NO_2 radicals. The dissociation energy of sym–N_2O_4 in the gas phase is 75 kJ/mol. The characteristic bands for symmetric NO_2 are 1368–1359 cm^{-1}, and for antisymmetric NO_2 they are 1758–1730 cm^{-1}. As well, a very strong out-of-plane NO_2 bend is observed at 743 cm^{-1} [100].

$$\mathbf{N_2O_4 \leftrightarrow 2NO_2} \qquad \textbf{(3–1)}$$

$$\mathbf{N_2O_4(l) \leftrightarrow NO^+(l) + NO_3^-(l)} \qquad \textbf{(3–2)}$$

$$\mathbf{N_2O_4(l) \leftrightarrow NO_2^+(l) + NO_2^-(l)} \qquad \textbf{(3–3)}$$

In anhydrous solutions, N_2O_4 self-ionizes almost completely to NO^+ and NO_3^- (reaction 3–2) and, to a much lesser degree, to NO_2^+ and NO_2^- (reaction 3–3). Partial dissociation of sym–N_2O_4 occurs in solution at low temperatures but becomes complete above 140 °C [99]. Sym–N_2O_4 is known to undergo self-ionization endothermically to form *trans*–$ON{\cdot}O{\cdot}NO_2$ **19** and *cis*–$ON{\cdot}O{\cdot}NO_2$ **18s**. Isomer **18s** is usually observed in condensed phases as a minor contaminant of sym–N_2O_4. Sterling et al. [101] describes the formation of **19** as the combination NO_2 and NO linked through an O bridge. The IR

bands of **19** are 1290 cm^{-1} for the symmetric stretch of NO_2, 1644 cm^{-1} for the antisymmetric stretch of NO_2, and 1828 cm^{-1} for the N=O stretching mode [100].

Perpendicular perp–ON·O·NO_2 **21** is found to have a O–N–O–NO dihedral angle of 90° for the terminal nitroso group (─N=O) relative to the planar NO_3 group, whereas for *cis*–ON·O·NO_2 **18s** and twist–ON·O·NO_2 **18g** we see dihedral angles of 6.8° and 40.1°, respectively [108]. Upon optimization, isomers **18s** and **18g** are found to interconvert into each other on going from the gas phase to solution and back again. Therefore, **18s** is not found to exist in the gas phase, and **18g** is not found to exist in the solution phase. Although these three conformations may appear to be very similar in structure, upon closer inspection of their bond lengths one sees that they are substantially different. The IR bands of **18g** are 1290 cm^{-1} for the symmetric stretch of NO_2, 1584 cm^{-1} for the antisymmetric stretch of NO_2, and 1890 cm^{-1} for the N=O stretching mode [100]. As for NO_2·O_2N **23**, Olson et al. [107] found it to be a stable intermediate to the formation of the more stable **21**.

The structural parameters for isomers ON·O_2NO **20** and $NO^+NO_3^-$ **22** are calculated for the first time, as far as we can determine. However, the X–ray crystal structure of $N_4O_6^{2+}$ $[(NO^+)_3(NO_3^-)]$ potentially contains **20** and **22** as structural subcomponents [109, 110]. We elieve that Song et al. [111] discusses the formation of **22** as a high pressure and high temperature induced phase transition from sym–N_2O_4 to ionic $NO^+NO_3^-$. They identify an observed IR peak at 2208 cm^{-1} as the distinguishing feature correlating it with the experimentally observed NO^+ stretching mode at 2390–2102 cm^{-1} [100, 112]. Our DFT/B3LYP/cc–pVTZ calculations yielded a stretching mode of 2167 cm^{-1}, underestimating the result of Song et al. by 41 cm^{-1}. This is a reasonable deviation,

considering that DFT/B3LYP/cc–pVTZ is known to underestimate frequencies by around this amount.

The peroxide form ON·OO·NO has been proposed as an intermediate in the oxidation of NO by O_2 to yield NO_2 [107]. Its three conformations are *cis/cis*, *cis/trans*, and *trans/trans* **24–26**. The remaining isomer type $OO\cdot(NO)_2$ is believed to have been calculated for the first time and was found to come in two conformational forms cis/cis **27** and *trans/trans* **28**.

3.3.2 Classifications of UN_4O_{12} Isomers Containing Uranyl Nitrate

Using the p5 B3LYP gas-phase optimized relative Gibbs free energy results we were able to visually sort the optimized gas-phase geometries of 73 distinct UN_4O_{12} isomers into three separate categories: (1) 44 dinitrogen tetroxide adducts of uranyl nitrate (a–series), $UO_2(NO_3)_2\cdot N_2O_4$, (2) 22 nitrosonium salt adducts of uranyl nitrate (b– series), $NO^+UO_2(NO_3)_3^-$, $NO^+UO_2(NO_3)_2O(NO_2)^-$, $NO^+UO_2(NO_3)_2(ONOO)^-$, or $(NO^+)_2UO_2(NO_3)_2O_2^{2-}$, and (3) seven bis(nitrogen dioxide) adducts of uranyl nitrate (c– series), $UO_2(NO_3)_2\cdot 2NO_2$. Our first category, the a–series, is characterized by having various forms of a neutral N_2O_4 group attached to a neutral uranyl nitrate. Basically, any weakly bound combination of two nitrogens and four oxygens not considered to be part of the uranyl nitrate group fell into this category. Fourteen a–series types were identified. The second category, the b–series, is characterized by the existence of an NO^+ group thought to be ionically bound to a complex anion $[UN_3O_{11}]^-$. Four different b–series

types were identified. The third category, the c–series, consists of two NO_2 groups that are not bound to each other but are each separately attached to uranyl nitrate. Only the one c–series type was identified.

3.3.2.1 N_2O_4 Adducts

A total of 44 gas-phase optimized structures were identified for the a–series category of the UN_4O_{12} isomers, $UO_2(NO_3)_2 \cdot N_2O_4$ (Figures 3–3 and 3–5 and the Appendix). They contain the lowest gas-phase Gibbs free energy isomer **a1**, which we chose to use as the reference for the comparison of the Gibbs free energy differences of all of the gas-phase isomers calculated. Fourteen different types of N_2O_4 adducts of uranyl nitrate were identified; all but six (types 3, 4, 8, 9, 13 and 14) were found to contain N_2O_4 structural forms previously identified in papers by Olson et al. [107] (types 1, 2, 5, 6, and 10–12), McKee et al. [108] (types 1, 6, 7, and 12), and Wang et al. [113] (types 1, 6, 7, and 10–12).

The most stable and most commonly cited gas- and solution-phase form of sym–N_2O_4 **17** was not only found to be represented within the three most stable gas-phase UN_4O_{12} structures but was also determined to have four separate type 1 (containing sym–N_2O_4) orientations (**a1**, **a2**, **a3**, and **a7**) (Figure 3–3). Both **a1** "side–on" and **a7** "end–on" are bidentately bound to uranium in the equatorial plane, whereas both **a2** and **a3** are unidentately bound.

Figure 3–3. Optimized UN_4O_{12} isomers: uranyl nitrate N_2O_4 adducts (bound NO_2 groups) obtained from p5 PBE/cc–pVTZ gas-phase optimized geometries.

type 1 containing sym–N_2O_4 **17**

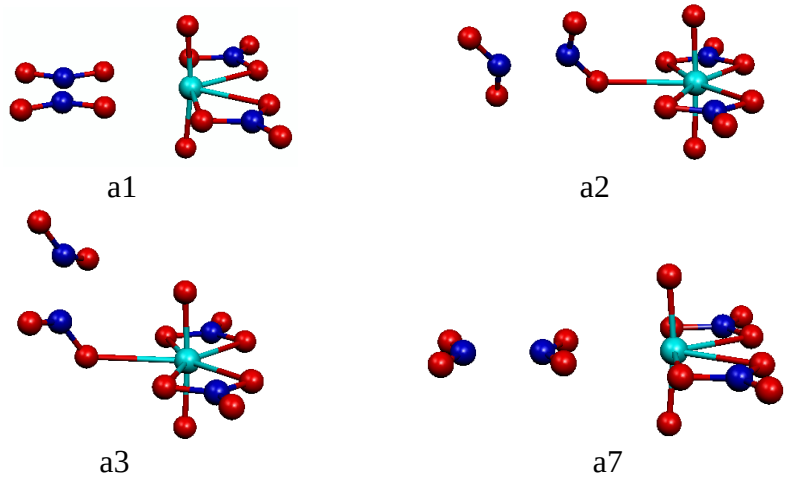

The third most stable solution-phase form of free N_2O_4, *trans*–ON·O·NO_2 **19**, was determined to be a component of four distinct type 6 orientations of UN_4O_{12} (Figure 3–4). Only **a5** was found to bond bidentately to uranium. The lowest–energy variation was **a4** with a G_{gas}^{rel} value of 2.1 kcal/mol. All three of **a4**, **a10**, and **a11** were found to be unidentately bound to uranium.

cis–ON·O·NO_2 **18s** is considered to be the second most stable solution-phase form of free N_2O_4. Six versions of the type 7 UN_4O_{12} isomer with **18s** as a component were identified with **a6** found to be lowest in energy with a G_{gas}^{rel} value of 2.7 kcal/mol. The others are **a9**, **a12**, and **a15**–**a17**.

The fourth most stable solution-phase form ON·O_2NO **20**, first occurs within type 8 as **a8** with a gas-phase relative Gibbs free energy of 2.6 kcal/mol and then also unidentately bound to uranium as **a13** and **a14** and again in an inverted form with the nitroso (─N=O) group oxygen unidentately bound to uranium as **a34** and **a35**.

Figure 3–4. Optimized UN_4O_{12} isomers: uranyl nitrate N_2O_4 adducts (NO_3 bound to a terminal nitroso [─N=O] or inverted nitrosonium cation) obtained from p5 PBE/cc–pVTZ gas-phase optimized geometries.

type 6 containing *trans*–ON·O·NO_2 **19**

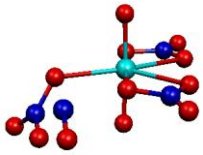

a4

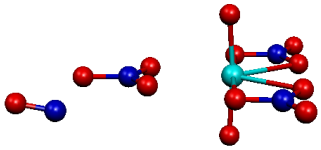

a5

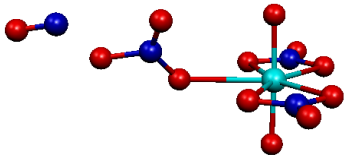

a10

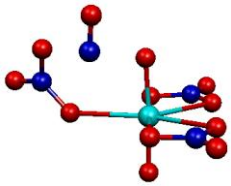

a11

type 7 containing *cis*–ON·O·NO_2 **18s**

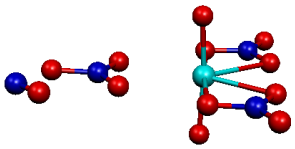

a6

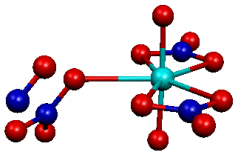

a9

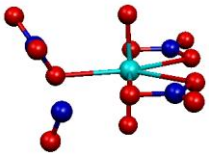

a12

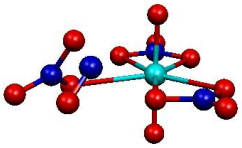

a15

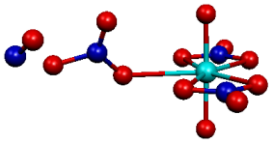

a16

type 8 containing ON·O_2NO **20**

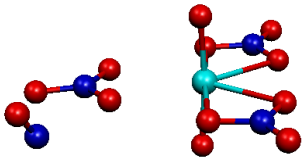

a8

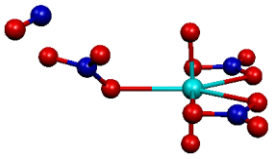

a13

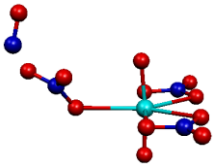

a14

type 9 containing $NO^+NO_3^-$ **22**

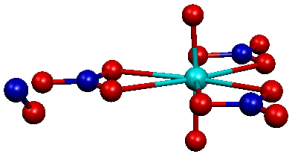

a27

Two occurrences of type 9, **a27** and **a44**, containing $NO^{+}NO_3^{-}$ **22**, the sixth most stable solution form of free N_2O_4, were identified, similar structurally to those of type 8, except the type 9 isomers contain an inverted nitrosonium cation instead of a nitroso (─N=O) group. Isomer **a27** corresponds to an inverted nitrosonium version of **a8**. The energy found for **a27** is 18.5 kcal/mol.

3.3.2.2 Nitrosonium Salts

A total of 22 gas-phase optimized structures were located for this b–series category of the UN_4O_{12} isomers, $NO^{+}UO_2(NO_3)_3^{-}$, $NO^{+}UO_2(NO_3)_2O(NO_2)^{-}$, $NO^{+}UO_2(NO_3)_2(ONOO)^{-}$, or $(NO^{+})_2UO_2(NO_3)_2O_2^{2-}$. They contain the fourth and fifth lowest gas-phase Gibbs free energy isomers **b1** and **b2**. Four distinct types of nitrosonium salts were identified.

The first set of five type 15 isomers **b1**–**b4** and **b6**, Figure 3–5, was found to have the lowest relative Gibbs free energies within the b–series. The first four structures were quite close in gas-phase energy to that of the reference structure **a1** with **b1** having a G_{gas}^{rel} value of 1.4 kcal/mol.

Figure 3–5. Optimized UN_4O_{12} isomers: uranyl nitrate nitrosonium salt adducts obtained from p5 PBE/cc–pVTZ gas-phase optimized geometries.

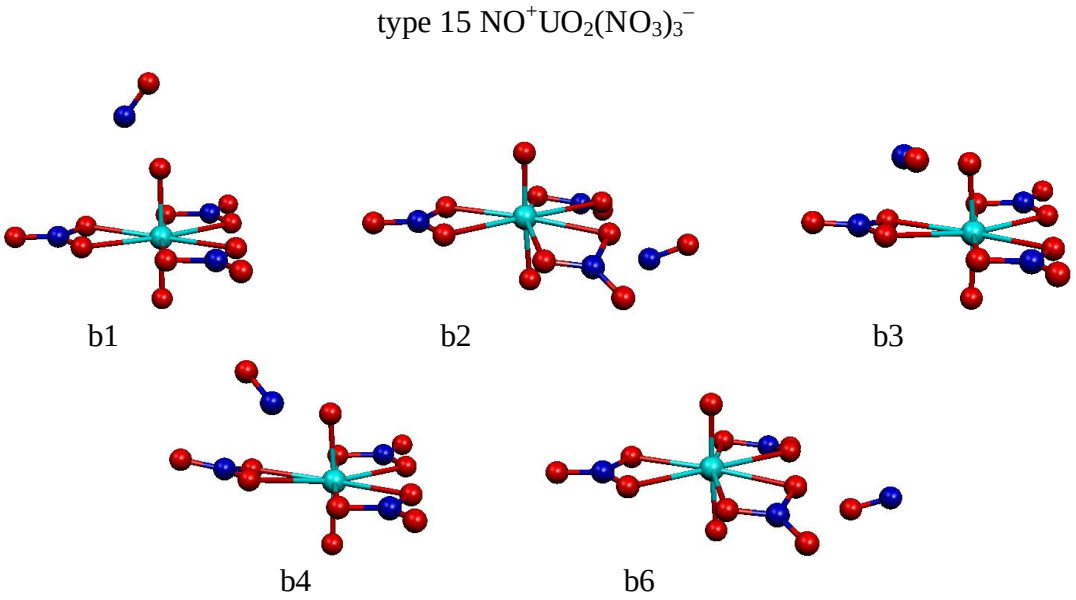

3.3.2.3 2·NO_2 Adducts

Seven c–series type 19 isomers **c1**–**c7** were identified with a uranyl nitrate group and two completely separate NO_2 groups located in various energy minimizing positions, $UO_2(NO_3)_2{\cdot}2NO_2$.

A more extensive version of the preceding discussion can be found in the Appendix under the same heading, in particular, the UN_4O_{12} isomers with higher relative Gibbs free energies: a–series types 3–5, 7–9, and 14, b–series types 16–18, and c–series type 19.

3.3.3 General Analysis and Discussion of Selected UN_4O_{12} Isomers

Single-point solvated Gibbs free energies were calculated for 30 gas-phase optimized structures (**a1**–**a21**, **a27**, **b1**–**b7**, and **c1)** with g03 B3LYP/CPCM using the p5 PBE gas-phase optimized geometries (Table 3–3). We chose to focus on the 22 UN_4O_{12} isomers **a1**–**a16**, **a27**, **b1**–**b4**, and **b6** after determining that they represented the 22 most stable structures in solution as well as the 20 most stable structures in the gas phase. The two isomers not among the 20 most stable gas-phase isomers are **a27** and **b6**. With the two largest ΔG_{solv} values of –31.5 and –31.1 kcal/mol, they were found to go from being the 33rd and 27th most stable isomers in the gas phase to being the fifth and 14th most stable isomers in solution.

A general analysis and discussion of the nature of bonding, Gibbs relative free energies, dipole moments, bond lengths, angles, and orders, Hirschfeld atomic charges [66, 114], vibrational frequencies, and metal coordination are given to provide the reader with a general understanding of how these properties varied over the selected UN_4O_{12} isomers.

3.3.3.1 Nature of Bonding within the N_2O_4 unit and between NO^+ and $UO_2(NO_3)_3^-$ Components

In performing an analysis of the various structures it was deemed important to discuss the nature of the bonding within the identified complexes. Often this can be

subject to different interpretations, so the following outlines the approach we chose to use in our interpretation.

There are various potential ways leading to the formation of these structures. In the following, we will describe a likely scenario. In solution our three starting components are uranium, present as the uranyl dication, dinitrogen tetroxide mostly in the sym–N_2O_4 form, and nitromethane, which is responsible for the dissociation of sym–N_2O_4 into the ionic components NO^+ and NO_3^- (reaction 3-2). With the anionic nitrate available, both uranyl nitrate $UO_2(NO_3)_2$ and trinitratouranylate $UO_2(NO_3)_3^-$ are expected to form. Next, the abundant sym–N_2O_4 likely combines with uranyl nitrate to form the a–series type 1 isomers **a1**–**a3** and **a7** in varying amounts. Furthermore, the combination of a nitrosonium cation and a trinitratouranylate complex anion likely leads to the formation of the b–series type 1 isomers **b1**–**b4** and **b6** as well as the a–series isomers **a5**, **a6**, **a8**, and **a27**. The remaining a–series isomers (**a4** and **a9**–**a16**), if at all existent in solution, could be formed through isomerization of the other forms.

Upon the basis of the abundance of research available on sym–N_2O_4, which consists of two radical NO_2 groups forming a covalent N–N bond, the four a–series type 1 isomers **a1**–**a3** and **a7** containing sym–N_2O_4 are considered to be of covalent bonding character with respect to their N–N bond. As described above, these UN_4O_{12} complexes are thought to be the result of coordinate bonding between neutral N_2O_4 and uranyl nitrate components.

The five b–series type 1 isomers **b1**–**b4** and **b6** all contain a nitrate anion (NO_3^-) attached to a neutral uranyl nitrate forming the complex anion $[UO_2(NO_3)_3]^-$, which further combines with a nitrosonium cation (NO^+) in various ways (Figure 3–5). At first

glance, all of these b–series type 1 isomers should be predominantly of ionic bonding character and are described as salts or salt adducts of uranyl nitrate. However, this is not necessarily the case as we discuss in more detail below.

For the remaining 18 isomers, we have defined the O_x oxygen to be the one that is weakly bound to the nitrogen of N_y=O except for **a27** and **b6** where two O_x oxygens bond symmetrically to the oxygen of N_y=O. N_y=O is considered to be a nitrosonium cation or an inverted nitrosonium cation (**b6**) for the b–series isomers and a terminal nitroso (─N=O) group or an inverted nitrosonium cation (**a27**) for the a–series isomers. The key bond for characterizing the nature of bonding of these structures is the O_x–N_y or O_x–O bond.

Isomer **b6** has a unique structure that involves an inverted N_y=O^+ group with its oxygen bound symmetrically to two separate nitrate oxygens of uranyl nitrate. More importantly, isomer **b6** is considered to be the only one of the b–series type 1 isomers ionic in character. It has calculated values for an O_x–O bond length of 2.364 Å, an O_x–O bond order of 0.10 (considered negligible), a N_y=O bond length of 1.105 Å, a N_y=O bond order of 2.41, and a N_y=O frequency of 2025 cm^{-1}. Corresponding experimental and theoretical values are 1.15 Å, 2.5, and 1876 cm^{-1} for free NO and 1.06 Å, 3.0, and 2390–2102 cm^{-1} for free NO^+.

Isomers **b2**, **b3**, and **b4**, classified as salts, are considered to be mostly ionic in nature. They have a small amount of covalent bonding character in the O_x–N_y bond with bond lengths of 2.127, 2.158, and 2.213 Å and bond orders of 0.29, 0.26, and 0.23, respectively. However, isomer **b1** with the shortest O_x–N_y bond length (1.735 Å) and a corresponding bond order of 0.65 may be more appropriately described as of mixed

covalent/ionic character rather than an ionic salt, although it is still considerably more ionic than covalent.

Isomer **a27** of type 9 has a unique structure that involves an inverted $N_y{=}O^+$ group with its oxygen weakly bound symmetrically to two different oxygens of a nitrate group. It is considered to be the only one of the selected a–series isomers to be predominantly of ionic character. It has an O_x–O bond length and bond order of 2.375 Å and 0.09 as well as a N_y=O bond length, bond order, and frequency of 1.109 Å, 2.37, and 2007 cm^{-1}.

The calculated data also show that the a–series type 8 isomers **a8**, **a13**, and **a14**, containing a N_2O_4 component of the form $ON{\cdot}O_2NO$ have O_x–N_y bond lengths of 2.110, 2.097, and 2.085 Å and corresponding bond orders of 0.28, 0.33, and 0.33. These isomers, therefore, represent the a–series isomers of mixed covalent/ionic bonding character with the most ionic character.

The remaining nine a–series type 6 and 7 isomers **a4**–**a6**, **a9**–**a12**, **a15**, and **a16** containing an N_2O_4 component of the form *trans*– or *cis*–$ON{\cdot}O{\cdot}NO_2$ are interpreted to be of mixed covalent/ionic bonding character, ranging in O_x–N_y bond length from 1.783 to 2.039 Å and in O_x–N_y bond order from 0.67 to 0.39 for **a10** and **a12**, respectively (Figure 3–4).

3.3.3.2 Energies

The 20 most stable gas-phase isomers are all within 5.45 kcal/mol (**a16**) of the gas-phase reference. The same 20 isomers in solution become much more separated from

each other and are now found to be within 10.4 kcal/mol (**a15**) of the solution-phase reference. Also noticeable is that the order of the gas-phase relative Gibbs free energies is not maintained in solution; a substantial reordering of the 20 most stable gas-phase isomers has occurred. As well, the solvent can be seen to have a stabilizing effect for the isomers analyzed; all 22 analyzed structures show a substantial reduction in absolute Gibbs free energy in going from the gas to the solution phase, with $\Delta G_{solv} = -12.8$ kcal/mol (**a2**) or more and $\Delta G_{solv} = -18.3$ kcal/mol on average (Table 3–1).

3.3.3.3 Dipole Moments

The two plots presented in Figure 3–6 of the differences in the gas- and solution-phase dipole moments $\Delta\mu = \mu_{soln} - \mu_{gas}$ and the solvation free energies ΔG_{solv} provide a rough estimate of the ionic versus covalent nature of the bonding within the 22 UN_4O_{12} isomers, and a general correlation can been seen between $\Delta\mu$ and ΔG_{solv}. The two most ionic isomers, with the largest values of $\Delta\mu$ and ΔG_{solv}, are **a27** and **b6**, whereas **a1** and **a2**, with the smallest changes in dipole moment and solvation free energies, would be considered the least ionic or the most covalent.

Figure 3–6. Δμ (♦, Debye) versus ΔG_{solv} (■, kcal/mol) of 22 UN_4O_{12} isomers

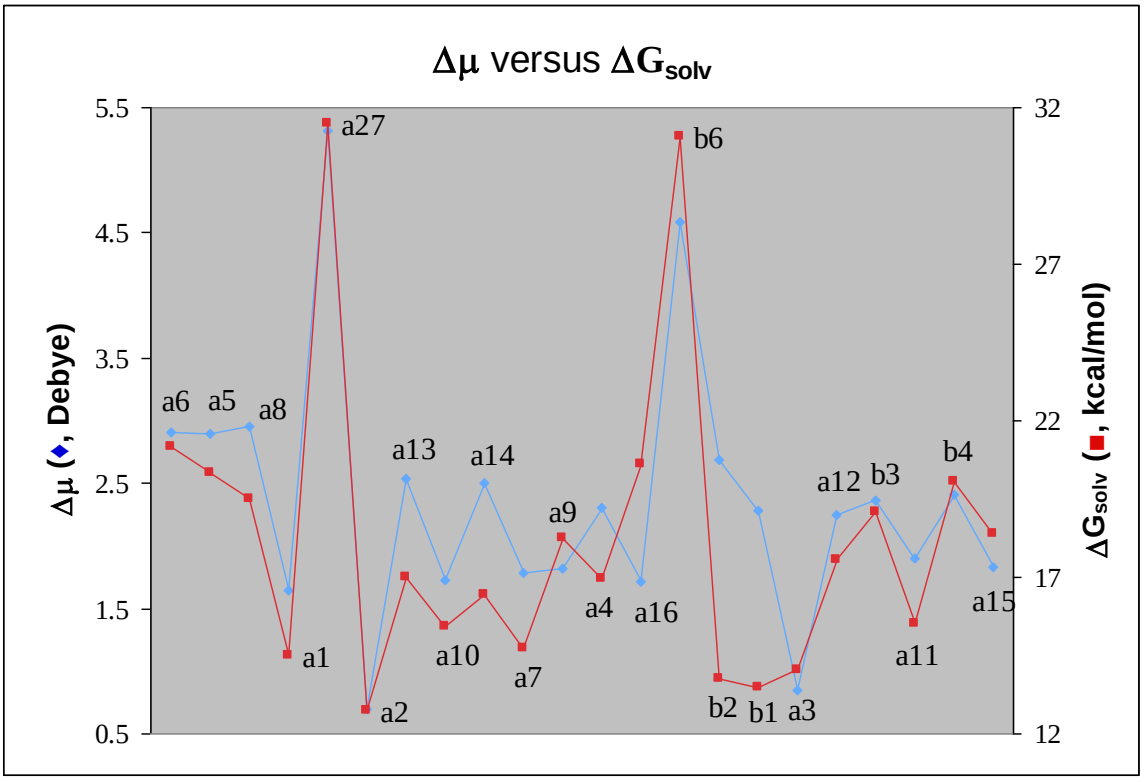

Both the amount of reduction in ΔG_{solv} and the order in relative Gibbs free energies of the 22 selected isomers can be attributed in part to the degree of charge separation within these particular structures. This charge separation is represented to a first order by the permanent dipole moment. In the gas phase both the p5 and g03 B3LYP results for dipole moments are very similar with the largest variance of 0.28 D (**a27**) found over the 22 isomers. The two isomers with the lowest and highest dipole moments in both the gas and solution phases are **a2** and **a27**, respectively, Table 3–3.

Table 3–3. Calculated single-point dipole moments, μ, and absolute dipole moment differences $\Delta\mu = \mu_{soln} - \mu_{gas}$ of the 22 most stable solution-phase UN_4O_{12} isomers (Debye)

Isomers	Gas-phase μ_{gas}		Solution–phase μ_{soln}	
	p5 B3LYP	g03 B3LYP	g03 C–PCM B3LYP (p5)	Δμ
a6	12.6	12.7	15.6	2.9
a5	13.0	13.2	16.1	2.9
a8	11.5	11.6	14.5	3.0
a1	7.5	7.4	9.1	1.7
a27	14.4	14.7	20.0	5.3
a2	4.7	4.6	5.3	0.7
a13	11.3	11.4	14.0	2.5
a10	9.4	9.4	11.1	1.7
a14	11.1	11.2	13.7	2.5
a7	8.3	8.3	10.0	1.8
a9	7.3	7.2	9.0	1.8
a4	7.4	7.4	9.7	2.3
a16	9.0	9.0	10.7	1.7
b6	11.4	11.5	16.0	4.6
b2	7.7	7.8	10.5	2.7
b1	6.2	6.1	8.4	2.3
a3	4.7	4.6	5.5	0.9
a12	7.2	7.2	9.4	2.3
b3	6.3	6.3	8.6	2.4
a11	6.1	6.1	8.0	1.9
b4	6.3	6.3	8.7	2.4
a15	6.7	6.6	8.5	1.8

The change in dipole moment Δμ is always positive in going from the gas phase to the solution phase. The change is reasonably consistent, ranging from 0.70 (**a2**) to 5.31 D (**a27**) but averaging 2.36 D for the 22 isomers. Higher–order charge moments will certainly play a role as well.

3.3.3.4 Bond Lengths, Angles, Bond Orders and Atomic Charges

For structural analysis each of the 22 selected isomers was separated into uranyl nitrate and nitrosonium tetroxide or nitosonium salt fragments. Ten bonds and three angles were identified for analysis (Tables 3–4 and 3–5).

The gas-phase uranyl bond lengths were found to vary little when no external group was found binding to either of the axial uranyl oxygens. In this case, they span a range of 1.790–1.799 Å, averaging around 1.795 Å. Correspondingly, the uranyl bond orders were very consistent at 2.40 ± 0.01. These numbers correspond to the well-known partial triple bond character of the uranyl bond. The uranyl bond order is reduced to values below 2.0 for those cases where an NO^+ is attached to the uranyl oxygen (**b1**, **b3**, and **b4**). All of the select gas-phase N_y=O bond lengths are found to range from 1.105 to 1.128 Å, with an average of 1.117 Å.

As for the weak O_x–N_y bond, it plays an important role in identifying the degree of charge separation between the N_y=O cation and the O_x oxygen of the complex anion for the isomers with ionic components. Equatorial U–O(nitrate) bonds show bond orders of 0.5– 0.6 in most cases, corresponding to partial covalent character, whereas the U– O(N_2O_4) bond orders are in most cases lower, averaging 0.36.

Of all of the isomers studied, structure **b1** was found to be the closest in geometry to that of the crystal structure isolated [60]. Unsigned mean deviations of selected bond lengths and angles between experimental X–ray crystallography and gas-phase calculations of 0.035 Å/0.3° were obtained. In particular, the experimental uranyl bond

length is 1.753 Å, which is 0.042 Å less than the calculated average. This shows that the PBE XC functional with the cc–pVTZ basis set used in our study overestimates this type of bond length, in agreement with earlier findings [88, 89, 95]. In studying UF_6 in the gas phase, Batista et al. [90] determined that using a PBE functional with a 6–31+G* basis set overestimated bond lengths by 1–2%. In our gas-phase study using PBE and the cc–pVTZ, basis set we found that the uranyl bond lengths were overestimated on average by 2.4%.

The calculated U and O charges in the uranyl ion vary little among the different species (Table 3–6). With the exception of **b6**, all selected UN_4O_{12} b–series isomers contain a N_y=O group where both atoms are positively charged. The nitrosonium oxygen of **b6** is the only one that was negatively charged.

Table 3–4. Calculated bond lengths and angles using p5 PBE/cc–pVTZ gas-phase optimized geometries of the 22 most stable solution-phase UN_4O_{12} isomers (in angstroms and deg)

isomers	uranyl nitrate						dinitrogen tetroxide / nitrosonium salt						
Gas	U=O	U=O	U–O	O_U–N	N–O_t	OUO	U–O	O_U–N	O_x–N_y[a]	N_y=O	N–N	UON	O_UNO
a6	1.797	1.796	2.423	1.306	1.203	174.2	2.653	1.252	1.938	1.115		96.2	119.5
a5	1.796	1.797	2.425	1.305	1.203	174.0	2.665	1.243	1.862	1.120		95.2	119.9
a8	1.796	1.796	2.421	1.306	1.202	174.4	2.657	1.303	2.110	1.115		97.6	117.6
a1	1.795	1.796	2.419	1.309	1.201	172.6	2.762	1.211			1.864		
a27	1.795	1.795	2.458	1.295	1.207	176.5	2.540	1.298	2.375	1.109			
a2	1.793	1.791	2.444	1.301	1.201	177.4	2.599	1.226			1.881		
a13	1.793	1.796	2.404	1.311	1.202	175.2	2.556	1.250	2.097	1.119			
a10	1.794	1.792	2.451	1.300	1.202	178.2	2.538	1.249	1.783	1.128			
a14	1.798	1.792	2.405	1.311	1.202	174.9	2.541	1.251	2.085	1.119			
a7	1.795	1.795	2.414	1.308	1.201	172.5	2.820	1.214			1.884		
a9	1.794	1.795	1.445	1.300	1.201	176.4	2.449	1.278	1.934	1.114			
a4	1.792	1.795	2.397	1.312	1.200	176.4	2.382	1.294	1.993	1.118			
a16	1.793	1.792	2.448	1.300	1.202	178.9	2.539	1.250	1.838	1.123			
b6	1.794	1.799	2.541	1.277	1.207	176.6			2.364	1.105		96.6	123.3
b2	1.792	1.798	2.567	1.266	1.201	176.2			2.127	1.115		96.6	123.5
b1	1.968	1.795	2.415	1.305	1.199	179.9			1.735	1.126		96.9	123.5
a3	1.799	1.790	2.445	1.301	1.200	176.2	2.568	1.231			1.897		
a12	1.793	1.793	2.396	1.318	1.200	175.9	2.387	1.305	2.039	1.117			
b3	1.877	1.793	2.412	1.307	1.200	174.6			2.158	1.113		96.4	120.5
a11	1.831	1.790	2.391	1.314	1.200	176.2	2.405	1.287	1.956	1.117			
b4	1.893	1.792	2.411	1.308	1.199	174.9			2.213	1.116		96.4	120.8
a15	1.790	1.790	2.433	1.302	1.200	178.5	2.515	1.268	1.906	1.120			
exptl.[b]		1.753	2.456	1.291	1.203	179.8						96.5	123.0

[a] O_x oxygen bonds weakly to nitrogen of N_y=O except for **a27** and **b6** where it bonds to oxygen of N_y=O.
[b] Reference [83] for $NO^+UO_2(NO_3)_3^-$ in the solid state.

Table 3–5. Calculated gas-phase Mayer bond orders [64, 65] using p5 PBE/cc–pVTZ optimized geometries of the 22 most stable solution-phase UN_4O_{12} isomers

isomers	uranyl nitrate					dinitrogen tetroxide / nitrosonium salt				
Gas	U=O	U=O	U–O	O_U–N	N–O_t	U–O	O_U–N	O_x–N_y[a]	N_y=O	N–N
a6	2.39	2.39	0.57	1.28	1.72	0.26	1.47	0.50	2.34	
a5	2.39	2.39	0.56	1.28	1.72	0.26	1.51	0.56	2.31	
a8	2.39	2.39	0.57	1.28	1.72	0.23	1.28	0.28	2.32	
a1	2.40	2.40	0.58	1.27	1.72	0.18	1.63			0.38
a27	2.39	2.39	0.51	1.31	1.70	0.35	1.30	0.09	2.37	
a2	2.40	2.40	0.54	1.30	1.73	0.24	1.58			0.37
a13	2.39	2.40	0.59	1.26	1.73	0.31	1.46	0.33	2.29	
a10	2.40	2.40	0.54	1.30	1.73	0.32	1.46	0.67	2.27	
a14	2.39	2.40	0.59	1.26	1.73	0.32	1.45	0.33	2.29	
a7	2.40	2.40	0.58	1.27	1.73	0.17	1.65			0.36
a9	2.39	2.40	0.54	1.30	1.73	0.40	1.35	0.50	2.35	
a4	2.40	2.40	0.59	1.26	1.73	0.53	1.29	0.43	2.30	
a16	2.40	2.40	0.54	1.30	1.73	0.32	1.45	0.61	2.28	
b6	2.39	2.39	0.39	1.37	1.70	0.55	1.28	0.10	2.41	
b2	2.39	2.40	0.36	1.42	1.73	0.57	1.28	0.29	2.33	
b1	1.95	2.41	0.58	1.27	1.74	0.44	1.12	0.65	2.34	
a3	2.39	2.40	0.54	1.30	1.73	0.27	1.53			0.35
a12	2.40	2.39	0.59	1.26	1.73	0.54	1.26	0.39	2.32	
b3	1.95	2.41	0.58	1.27	1.74	0.44	1.12	0.26	2.34	
a11	2.19	2.40	0.61	1.25	1.74	0.49	1.32	0.46	2.32	
b4	1.88	2.41	0.58	1.27	1.74	0.44	1.15	0.23	2.32	
a15	2.40	2.40	0.55	1.29	1.73	0.38	1.39	0.50	2.29	

[a] O_x oxygen bonds weakly to nitrogen of N_y=O except for **a27** and **b6** where it bonds to oxygen of N_y=O.

Table 3–6. Calculated Hirschfeld atomic charges [94] using p5 PBE/cc–pVTZ gas-phase optimized geometries of the 22 most stable solution-phase UN_4O_{12} isomers (e)

isomers	uranyl nitrate						dinitrogen tetroxide / nitrosonium salt				
Gas	U	$O_{U=O}$	$O_{U=O}$	O_U	N	O[a]	O_U	N[b]	O_x[c]	N_y	$O_{N=O}$
a6	0.49	–0.29	–0.28	–0.16	0.30	–0.14	–0.12	0.30	–0.05	0.24	0.16
a5	0.49	–0.28	–0.28	–0.16	0.30	–0.14	–0.10	0.30	–0.12	0.24	0.14
a8	0.49	–0.28	–0.29	–0.16	0.30	–0.14	–0.10	0.30	–0.12	0.24	0.15
a1	0.51	–0.28	–0.28	–0.17	0.30	–0.13	–0.03	0.25			
a27	0.48	–0.28	–0.28	–0.15	0.30	–0.13	–0.14	0.29	–0.16	0.25	0.21
a2	0.60	–0.28	–0.27	–0.16	0.30	–0.13	–0.05	0.23			
a13	0.56	–0.29	–0.28	–0.16	0.30	–0.14	–0.10	0.30	–0.13	0.22	0.13
a10	0.58	–0.29	–0.28	–0.16	0.30	–0.14	–0.09	0.30	–0.12	0.21	0.11
a14	0.56	–0.30	–0.27	–0.16	0.30	–0.14	–0.10	0.30	–0.12	0.22	0.13
a7	0.51	–0.28	–0.28	–0.16	0.30	–0.16	–0.15	0.22			
a9	0.56	–0.28	–0.28	–0.16	0.30	–0.13	–0.15	0.30	–0.13	0.24	0.17
a4	0.57	–0.27	–0.29	–0.16	0.30	–0.13	–0.16	0.30	–0.14	0.24	0.13
a16	0.58	–0.28	–0.28	–0.16	0.30	–0.14	–0.09	0.30	–0.12	0.22	0.12
b6	0.48	–0.28	–0.30	–0.11	0.29	–0.15	–0.15	0.30	–0.17	0.27	–0.15
b2	0.48	–0.27	–0.30	–0.11	0.30	–0.13	–0.15	0.30	–0.15	0.25	0.15
b1	0.47	–0.28	–0.26	–0.15	0.30	–0.12	–0.15	0.30	–0.25	0.26	0.17
a3	0.57	–0.30	–0.27	–0.16	0.30	–0.13	–0.06	0.23			
a12	0.56	–0.28	–0.28	–0.16	0.30	–0.13	–0.17	0.30	–0.14	0.24	0.14
b3	0.47	–0.28	–0.26	–0.15	0.30	–0.12	–0.15	0.30	–0.28	0.26	0.17
a11	0.55	–0.30	–0.26	–0.16	0.30	–0.12	–0.15	0.30	–0.14	0.25	0.14
b4	0.48	–0.28	–0.25	–0.15	0.30	–0.12	–0.15	0.29	–0.28	0.27	0.15
a15	0.58	–0.28	–0.27	–0.15	0.30	–0.13	–0.11	0.29	–0.11	0.23	0.13

[a] External O of uranyl nitrate. [b] N of N_2O_4 or NO_3 nearest to U. [c] O_x oxygen bonds weakly to nitrogen of N_y=O except for **a27** and **b6** where two O_x oxygens bond to oxygen of N_y=O.

3.3.3.5 Frequencies

Analysis of gas-phase frequencies for the 22 selected isomers, through there relationship to bond lengths and bond strengths, highlights the predominantly mixed covalent/ionic nature of the majority of these isomers (Table 3–7). Particularly distinct dinitrogen tetroxide / nitrosonium salt bands are the N_y=O stretching modes, the two N_y=O torsions, the O_x–N_y stretching mode and the out-of-plane NO_3 bending mode.

Experimentally, the gas-phase stretching frequency of N=O in its free form is 1876 cm^{-1} [115], and as part of **18g**, 1890 cm^{-1}, and **19**, 1828 cm^{-1}. However, $N{=}O^+$ in its free form exhibits frequencies ranging from 2390 to 2102 cm^{-1}, and in salts is often seen to absorb in the 2391–2150 cm^{-1} range [116]. The 18 isomers that we studied with N_y=O stretching frequencies had values that ranged from 1915 to 2025 cm^{-1} suggesting that the complexation of these structures had the effect of strengthening the N_y=O bond relative to their N_2O_4 counterparts in free form; thereby increasing the N_y=O stretching frequencies. The actual effect may even be somewhat larger because DFT PBE has a tendency to underestimate experimental frequencies.

In general, other than the strongly mixed modes of **a2**, we see a very consistent underestimation of uranyl symmetric and antisymmetric stretching modes (848 ± 7 cm^{-1}, 930 ± 7 cm^{-1}) and an overestimation of uranyl bending mode (203 ± 6 cm^{-1}) across the isomers analyzed. This can be compared to experimental IR spectral data [117] where we see values of 871, 940, and 182 cm^{-1}, resulting in differences of –24, –12, and +23 cm^{-1}, respectively. Exceptions are the uranyl bending mode of **a12**, **a27**, and **b6** and the uranyl modes of **a11**. As for the b–series, with the bonding of NO^+ to one of the

Table 3–7. Calculated vibrational frequencies using p5 PBE/cc–pVTZ gas-phase optimized geometries of the 22 most stable solution-phase UN_4O_{12} isomers (cm^{-1})

isomers	uranyl			dinitrogen tetroxide / nitrosonium salt											
Gas	s-str OUO	a-str OUO	bend OUO	s-str NO_2	a-bend NO_2	s-bend NO_2	s-str N–N	str NO_3	str NO_3	s-str NO_3	bend NO_3	str O_x–N_y[a]	str N_y=O	tor N_y=O	tor N_y=O
a6	843	923	203					1198	1423		758	289	1957	512	
a5	844	924	206					1201	1444		766	280	1933	522	
a8	846	926	208					1186	1419	974	760	267	1981	490	378
a1	846	925	200	1371	620	389	292								
a27	846	927	214										2007	278	252
a2[b]															
a13	849	929	208					1208	1355	999	769	274	1961	517	399
a10	851	933	207					1202	1579		745	319	1920	501	
a14	847	928	209					1213	1347	999	771	277	1962	514	393
a7	850	927	197	1383	729	418	273								
a9	849	931	208					1120	1530		764	308	1991	515	
a4	850	932	209					1107	1504		772	279	1963	477	330
a16	852	934	206					1196	1508		764	324	1941	572	
b6	842	925	225										2025	277	261
b2	846	929	206									263	1980	468	376
b1												269	1915	652	583
a3	848	930		1369	724	375	264								
a12	849	932	221					1090	1506		772		1965	463	
b3												297	1984	458	370
a11	789	905	224					1122	1512		761	275	1968	482	296
b4												317	1964	459	346
a15	855	937	207					1162	1481		783	333	1943	548	256
Expt[c]	871	940	182												

[a] O_x oxygen bonds weakly to nitrogen of N_y=O except for **a27** and **b6** where it bonds to oxygen of N_y=O. [b] Strongly mixed vibrational modes for **a2**. [c] Reference [98] for $NO^+UO_2(NO_3)_3^-$ in the solid state.

uranyl oxygens in **b1, b3**, and **b4** the typical uranyl modes do not exist; in their place we see lone U=O stretching and bending modes. This is not, however, the case with **b2** and **b6** where the nitrosonium ion bonds symmetrically between two nitrate oxygens.

3.3.3.6 Metal Coordination

For all of the isomers studied uranium was always found to be either seven- or eight-coordinate. Seven-coordinate uranium was found to contain a unidentately–coordinated component, and eight-coordinate uranium was found to contain a bidentately coordinated component. The one exception is **c7**, which was found to contain two unidentately coordinated components, for a coordination number of 8.

3.3.4 By-Type Discussion of Selected UN_4O_{12} Isomers

This final subsection focuses on a by-type discussion of 22 select UN_4O_{12} isomers for the purpose of identifying the structure or structures most likely to predominate in either an inert gas or a nonaqueous polar aprotic solvent environment. To gauge the likelihood of their existence in the gas or solution phases UN_4O_{12} isomers were tabulated according to their relative Gibbs free energies. Of the 22 selected structures only two of the three categories and six of the 19 types classified in subsection **3.3.2** were

represented. The proceeding discussions are organized around these six types of isomers: a–series type 1, 6, 7, 8, and 9 and b–series type 15.

3.3.4.1 a–series type 1: a1, a2, a3 and a7

All four a–series type 1 isomers are found to be among the 20 most stable gas-phase and the 22 most stable solution-phase isomers. This group is characterized by containing the most stable gas-phase form of planar sym–N_2O_4 (Figure 3). Bidentately bound planar N_2O_4 components within **a1** and **a7** maintain their planar form parallel to the equatorial plane of uranyl nitrate, whereas unidentately bound planar N_2O_4 components within **a2** and **a3** although equatorially bound to uranium, maintain their planar shape outside the equatorial plane of uranyl nitrate.

With **a2** being within 0.2 kcal/mol of **a1** for our p5 B3LYP gas-phase calculations and actually lower than **a1** by 0.2 kcal/mol for the g03 B3LYP gas-phase calculations it is quite possible that **a2** is the more stable isomer. In any case, at room temperature both are as likely to be present. The remaining two isomers **a3** and **a7** have p5 gas-phase relative Gibbs free energies of 1.2 and 2.5 kcal/mol, respectively. In solution these four isomers become the fourth, sixth, 17th, and 10th most stable with relative Gibbs free energies of 3.6, 5.2, 9.0, and 6.8 kcal/mol, respectively. The absolute Gibbs free energy differences between the gas and the solution-phase results for these four isomers are found to be less than average (–18.3 kcal/mol), ranging from –12.8 to –14.7 kcal/mol with **a2** having the lowest ΔG_{solv} value of –12.8 kcal/mol. The dipole moment differences between the gas

and the solution phases are also found to be below average (2.36 D), ranging from 0.70 to 1.78 D.

The two longest U–O bonds, 2.762 Å for **a1** and 2.820 Å for **a7**, both connect uranium bidentately to N_2O_4. Correspondingly, we see the two smallest bond orders of 0.18 for **a1** and 0.17 for **a7**. The O_U–N bond lengths for **a1** and **a7** are 1.211 and 1.214 Å due to bidentately bound N_2O_4 components, whereas for **a2** and **a3** they are 1.226 and 1.231 Å due to unidentately bound N_2O_4 components. These four bonds correspond to the four strongest O_U–N bond orders overall, 1.63, 1.58, 1.53, and 1.65 for **a1**, **a2**, **a3**, and **a7**, respectively. The four weakly binding N–N bonds were found to have lengths of 1.864, 1.881, 1.897, and 1.884 Å and bond orders of 0.38, 0.37, 0.35, and 0.36 for **a1**, **a2**, **a3**, and **a7**. As for the atomic charges, only those on uranium showed a significant variation with 0.51 e for both bidentate isomers (**a1** and **a7**) and 0.60 e and 0.57 e for the two unidentate isomers **a2** and **a3**.

Four characteristic vibrational modes, one NO_2 stretching mode and two NO_2 bending modes along with one N–N stretching mode, were used to analyze three of the four a–series type 1 isomers. The lower–frequency out-of-plane antisymmetric bending mode of **a1** could be used to distinguish it from **a3** and **a7**. Otherwise the two NO_2 bonded radicals of **a1**, **a3**, and **a7** were found to have similar stretching and bending modes. Isomer **a2** has many mixed modes, and it was found to be very difficult to identify any distinct modes.

3.3.4.2 a–series type 6: a4, a5, a10 and a11

All four a–series type 6 isomers are found to be among the 22 selected isomers. This group is characterized by containing various orientations of *trans*–ON·O·NO_2 **19**. Only **a5** was found to bond bidentately to uranium. In comparing bond lengths of the N_2O_4 component of **a5** to those of free N_2O_4, we see that 1.862, 1.243, and 1.120 Å compare to 1.61, 1.20, and 1.13 Å for O_x–N_y, O_U–N and N_y=O. Of these, only the O_x–N_y bond distance, with a difference of 0.25 Å, does not compare very well. In going from the gas phase to solution isomers **a4**, **a5**, **a10**, and **a11** change from having relative Gibbs free energies of 2.1, 2.4, 3.0, and 3.7 kcal/mol to values of 7.4, 1.1, 6.0, and 10.0 kcal/mol. With **a5** being only 1.1 kcal/mol above **a6**, it is considered to be a reasonably good candidate to exist and predominate in solution. The ΔG_{solv} values show little variation from the average of –18.3 kcal/mol ranging from –15.4 to –20.3 kcal/mol. The change in dipole moment, $\Delta\mu$, ranges from 1.73 to 2.90 for these isomers but does not vary significantly from the average value of 2.36 D.

As for the structural analysis of this series of isomers, as well as the atomic charges and vibrational frequencies, they were found to be very similar, and no distinguishing features could be identified.

3.3.4.3 a–series type 7: a6, a9, a12, a15 and a16

Five of the possible six isomers of the a–series type 7 are found to be among the 22 selected isomers with the other isomer **a17** being the 23rd most stable isomer in solution. This group is characterized by containing *cis*–ON•O•NO_2 **18s**.

Isomer **a6**, with a gas-phase relative Gibbs free energy of 2.5 kcal/mol, was determined to be the most stable isomer in solution overall and as such is thought to be the most likely isomer to exist and predominate in solution. In comparing bond lengths of the N_2O_4 component of **a6** to those of free N_2O_4, we see that 1.938, 1.252, and 1.115 Å compare very well to 1.93, 1.23, and 1.09 Å for O_x–N_y, O_U–N, and N_y=O. Other features of **a6** are that it is the only type 7 isomer bidentately bound to uranium and that it along with **a9** contains the only two nearly planar forms of *cis*–ON·O·NO_2. As for the other type 7 isomers (**a12**, **a15**, and **a16**) their N_2O_4 components are found to be noticeably less planar. In going from the gas to the solution phase, the remaining isomers (**a9**, **a12**, **a15**, and **a16**) have relative Gibbs free energies of 2.9, 4.1, 4.8, and 5.5 kcal/mol and 6.8, 9.1, 10.4, and 7.6 kcal/mol, respectively. The values for ΔG_{solv}, μ and Δμ are quite similar for these isomers and change little from their average values with the exception of the dipole moment of **a6**, which at 12.63 D is the second largest.

The U=O bond length of **a6** is just over 0.1 Å longer than the other four isomers due to its bidentate bonding to uranium. Correspondingly, the bond order is about 0.06 less for **a6**. The atomic charges of the dinitrogen tetroxide component are found to be very similar for all five isomers.

As for the vibrational frequencies, all are very much the same, and no characterizing information could be identified. In particular, distinguishing **a6** from **a5** would be very difficult as nearly every mode tabulated for these two isomers is in close agreement. The N_y=O stretching mode provides the largest frequency difference of +24 cm^{-1} for **a6** relative to that of **a5**.

3.3.4.4 a–series type 8: a8, a13 and a14

Three of the five members of the a–series type 8 isomers are found to be among the 22 selected isomers. This group is characterized by containing ON•O_2NO **20** where the nitrogen of a nitrosonium cation bonds symmetrically to two oxygens of a nitrate group.

The only bidentate isomer is **a8** with gas- and solution-phase relative Gibbs free energies of 2.6 and 2.2 kcal/mol, respectively. Isomer **a8** is the third most stable solution-phase isomer and possibly a candidate to exist in solution. In comparing bond lengths of the N_2O_4 component of **a8** to those of free N_2O_4, we see that 2.110, 1.303, and 1.115 Å compare reasonably well to 2.03, 1.28, and 1.11 Å for O_x–N_y, O_U–N and N_y=O. The other two type 8 isomers are also found to be quite stable in solution with **a13** and **a14** being the sixth and eighth most stable at 5.6 and 6.3 kcal/mol compared to their gas-phase energies of 4.5 kcal/mol each. The ΔG_{solv}, μ, and Δμ values are quite similar and change little from their average values.

The U=O bond length of **a8** is just over 0.1 Å longer than the other two type 8 isomers due to the bidentate bonding of the N_2O_4 group to uranium. Correspondingly, the

bond order is about 0.08 less for **a8**. As for the atomic charges of the dinitrogen tetroxide component they are very similar for all three isomers.

The most identifying vibrational frequency of these three isomers is the symmetric stretching mode of the non–uranyl nitrate NO_3 group (974 cm^{-1} for **a8** and 999 cm^{-1} for both **a13** and **a14**), which is not seen for the other selected isomers.

3.3.4.5 a–series type 9: a27

Only one of two possible isomers of a–series type 9 **a27** was found to be among the selected isomers. This type is characterized by containing an ionically bound $NO^+NO_3^-$ **22** component, where uncharacteristically the oxygen of a nitrosonium cation bonds symmetrically to two oxygens of a nitrate group. Isomer **a27** with gas- and solution-phase relative Gibbs free energies of 17.8 and 4.5 kcal/mol, respectively, is the fifth most stable solution-phase UN_4O_{12} isomer. The **a27** isomer is found to have the largest values for ΔG_{solv} = –31.5 kcal/mol, μ_{gas} = 14.44 D, μ_{soln} = 20.03D, $\Delta\mu$ = 5.31 D, and O_x–N_y bond length = 2.375 Å of all 22 selected isomers.

Isomer **a27** has many similarities with **b6**; for example, both have a nitrosonium ion that is inverted with the oxygen of the NO^+ group, bonding equally to the two nitrate oxygens. As well, they represent the two isomers with the largest values for ΔG_{solv}, $\Delta\mu$, and O_x–N_y bond lengths. Furthermore, they share three very similar characteristic vibrational modes: the N_y=O stretching band and the two N_y=O torsion bands. Both are also found to have the two highest N_y=O stretching frequencies corresponding to the two

shortest N_y=O bond lengths. The one area where they differ substantially is the atomic charge on the $O_{N=O}$ oxygen, Table 5, where **a27** is seen to have the largest positive charge of 0.21 e, and **b6** is seen to have the lowest charge of –0.15 e (the only one found to be negatively charged).

3.3.4.6 b–series type 15: b1, b2, b3, b4 and b6

All five b–series type 15 nitrosonium salt adducts of uranyl nitrate are found to be among the 20 most stable gas-phase and the 22 most stable solution-phase isomers. This group is characterized by containing an NO^+ group ionically bound to a $[UO_2(NO_3)_3]^-$ complex anion. For isomer **b1**, the nitrogen of the NO^+ cation is bound to one of the uranyl oxygens. Similarly, for **b3** and **b4**, the nitrogen of the nitrosonium ion appears to be weakly shared between both the nitrate oxygen and the uranyl oxygen. As for isomers **b2** and **b6**, they share a similar symmetric configuration with the NO^+ group ionically shared between two different nitrate oxygens. With **b2**, the nitrogen of the nitrosonium ion is bound to the two nitrate oxygens, whereas in the case of **b6** the nitrosonium ion is inverted with the oxygen of the NO^+ group bonding equally to the two nitrate oxygens.

The fourth and fifth lowest gas-phase relative Gibbs free energy isomers are **b1** and **b2** with relative Gibbs free energies of 1.4 and 1.7 kcal/mol. They become the 15th and 14th isomers in solution with relative Gibbs free energies of 8.8 and 8.2 kcal/mol, respectively. The other isomers **b3, b4**, and **b6** have G_{gas}^{rel} values of 2.6, 3.6, and 15.7 kcal/mol in the gas phase and 9.6, 10.4, and 8.2 kcal/mol in solution. The ΔG_{solv} values of

these five b–series isomers show the largest variation ranging from –13.5 kcal/mol for **b1** to –31.1 kcal/mol for **b6**. As for the change in dipole moment values, Δμ, they are all found to be near the 2.36 D average for the selected isomers with the highest b–series type 15 Δμ of 4.58 D for **b6**.

The interaction of the NO^+ group with the uranyl oxygens leads to a weakening and therefore a lengthening of the uranyl bond lengths for **b1** (1.877 Å), **b3** (1.968 Å), and **b4** (1.893 Å) compared to the average of 1.795 Å. This is supported by smaller corresponding uranyl bond orders of 1.95, 1.95, and 1.88 relative to the average of 2.40 (as discussed previously). All five b–series type 15 isomers were found to have the lowest atomic charges on uranium (0.47 or 0.48 e).

With the b–series type 15 isomers containing an anionic trinitratouranylate, we are able to identify four characteristic vibrational modes: one N=O stretching band, two N=O torsion bands, and one O_xN_y stretching band. Isomers **b1** and **b6** were found to have the lowest and highest N=O stretching frequencies of 1915 and 2025 cm^{-1}, corresponding to the longest and shortest N_y=O bond lengths of 1.126 and 1.105 Å.

3.3.5 Dissociation

The dissociation of UN_4O_{12} is briefly discussed according to the following reaction:

$$\mathbf{UN_4O_{12} \leftrightarrow [UO_2(NO_3)_3]^- + NO^+} \qquad \textbf{(3–4)}$$

Free energies were calculated, for (reaction 3–4), using the exact same computational methods. Taking for the left-hand side of (reaction 3–4) the most stable gas-phase isomer **a1**, we obtained free energies for the reaction of 120.7, 102.8 and 100.9 kcal/mol for p5 PBE, p5 B3LYP, and g03 B3LYP, respectively. Not surprisingly, the dissociation reaction is highly unfavorable in the gas phase.

In solution, the most stable solution-phase isomer **a6** was used as the reference point. At the g03 B3LYP CPCM level of theory, we obtained a reaction energy of $\Delta G = -5.2$ kcal/mol. At this level of theory, the dissociated species, at infinite separation, would be more stable than the most stable non-dissociated conformer, and dissociation would be energetically favorable. The dramatic change between the gas and solution phase can be explained as being due to the stabilization of the charged species in a polar solvent.

However, continuum solvation models such as those used here are at or beyond the limits of their applicability for molecules with a high concentration of charge, such as the NO^+ ion in this case. In other words, the solvation treatment is not entirely balanced between the small and the large molecules in (reaction 3–4), introducing the potential for substantially large errors. Moreover, the situation in real, experimental solutions is likely to be even more complex than that modeled here. For instance, the possibility of ion pairs has not been accounted for by this simple solvation model. Overall, these errors make any conclusion regarding the relative stability of dissociated versus non-dissociated species somewhat questionable.

3.4 Conclusion

The combination of the experimental and computational results obtained by others and the computational results generated for this paper have provided us with a much broader view of the structures involved and we believe a better insight into the likely identity of the predominant UN_4O_{12} uranyl nitrate isomer existing in both the gas phase and the 30:70 nitromethane/dinitrogen tetroxide solution used in experiment [83].

We have studied the relative Gibbs free energies of 73 identified UN_4O_{12} uranyl nitrate isomers. Fourteen of these isomers are closely spaced within 2.6 kcal/mol of the most stable gas-phase isomer **a1**. Isomer **a1** contains the most familiar and well-studied sym–N_2O_4 bidentately bound to the uranium atom of uranyl nitrate. The next most stable isomer **a2** was determined to be 0.2 kcal/mol more energetic by one method (p5 B3LYP) and 0.2 kcal/mol less energetic by our other method (g03 B3LYP). Isomer **a2** contains a unidentately bound form of sym–N_2O_4. The following three isomers in order of stability are **a3**, **b1**, and **b2** with relative Gibbs free energies of 1.2, 1.4, and 1.7 kcal/mol, according to the p5 B3LYP calculations. Isomer **a3** is a higher-energy conformation of **a2**, and conformers **b1** and **b2** are the two most stable nitrosonium salt adducts of uranyl nitrate. For **b1** the nitrosonium ion is bound via nitrogen to one of the uranyl oxygens, and for **b2** the nitrosonium nitrogen is symmetrically bound between two oxygens of two different nitrate groups. On the basis of our relative Gibbs free energy results, all five of these isomers (**a1**, **a2**, **a3**, **b1**, and **b2**) are considered to be strong candidates to exist and possibly predominate in the gas phase, with **a1** and **a2** being the strongest candidates.

After narrowing down our relative Gibbs free energy calculations of 30 isomers in solution to the 22 most stable, we identified three isomers to be within 3.6 kcal/mol of the most stable solution-phase isomer **a6**. Isomer **a6** contains a *cis*–ON•O•NO_2 **18s** bidentately bound to uranyl nitrate. The next most stable isomer in solution **a5** (with a relative Gibbs free energy of 1.1 kcal/mol) contains the *trans*–ON•O•NO_2 **19** bidentately bound to uranyl nitrate. The third most stable isomer in solution is **a8** with a relative Gibbs free energy of 2.2 kcal/mol. Isomer **a8** is characterized by containing ON•O_2NO **20,** where the nitrogen of a terminal nitroso group bonds symmetrically to two oxygens of a nitrate group that is bidentately bound to uranium. The fourth most stable isomer in solution is **a1** with a relative Gibbs free energy of 3.6 kcal/mol. Therefore, isomer **a6** is considered to be the most likely candidate to predominate in a solution of nitromethane/dinitrogen tetroxide.

Of the 22 analyzed isomers, only two UN_4O_{12} isomers **a27** and **b6** were considered to clearly contain an O_x–N_y ionic bond with the two largest bond lengths of 2.375 and 2.364 Å, respectively. Also, these two isomers represented the two largest N_y=O stretching frequencies of 2007 cm^{-1} for **a27** and 2025 cm^{-1} for **b6**, corresponding to the two shortest bond lengths of 1.109 to 1.105 Å. Four isomers, **a1**–**a3** and **a7**, containing sym–N_2O_4 isomers had covalent character, and therefore no N_y=O stretching frequencies were present. The remaining 12 dinitrogen tetroxide adducts and four nitrosonium salt adducts of uranyl nitrate had mixed covalent/ionic character with N_y=O stretching frequencies that ranged from 1915 to 1991 cm^{-1} and corresponding bond lengths ranging from 1.113 to 1.128 Å.

Although the **b1** structure was found to most closely describe the geometry of the solid-state crystals prepared [60], the 8.8 kcal/mol relative Gibbs free energy in solution suggests that **b1** is not a likely candidate to predominate in solution. All five of the nitrosonium salt adducts of uranyl nitrate that were within the 22 most stable solution-phase isomers were at least 8.2 kcal/mol (**b6**) more energetic than the reference **a6** and therefore are not thought to be likely candidates to predominate in solution.

Experimentally, with the lowering of the temperature of the saturated solution and upon solidification, it seems quite possible for the terminal nitroso or nitrosonium cation group of any one of the 18 isomers mentioned (Figures 3–4 and 3–5) with ionic or mixed covalent/ionic character to have rearranged into the solid-state crystal structure that was identified as the nitrosonium salt, $NO^{+}UO_2(NO_3)_3^{-}$ [60].

The question of dissociation in solution has been addressed briefly by applying a simple model reaction. However, the results were found to be inconclusive.

It is important to recognize that the computational methods used do not take into account reaction kinetics and the necessary approximations of the methods used are sources of error that create some uncertainty in the interpretation of the results obtained. What the computational methods do provide are structural relative Gibbs free energies that can be used as a measure of relative stability for identifying those structures found to be the most computationally stable. Thus, in providing experimentalists with strong candidates, along with accompanying molecular properties, it is our hope that it will prove to be useful in identifying the existence of these UN_4O_{12} structures within both the solution and the gas phases.

For this study, the use of optimized gas-phase geometries to calculate single-point relative Gibbs free energies in solution is not ideal and may be a possible source of error. Optimizing these geometries in solution would be preferable, though current methods present difficulties with convergence.

Also, there is an inherent difficulty in modeling weak bonds, such as the O_x–N_y or O_x–O bond, found in 18 of the selected isomers, as well as the N–N bonds found in the remaining four isomers. This along with the known tendency for DFT PBE to overestimate bond lengths is a likely source of some error. Correspondingly, the longer bond lengths translate into an underestimation of vibrational frequencies. As well, there may be some error in the use of DFT B3LYP for calculating absolute Gibbs free energies; however, due to the benefit of error cancellation a smaller degree of error would be seen for relative Gibbs free energies. The same general conclusion would emerge from using DFT with the PBE functional, giving some confidence in our results.

The use of restricted, closed-shell formalism may not model some of the higher-energy structures effectively due to the radical nature of some of the N_2O_4 isomers and the UN_4O_{12} isomers containing them as components.

Furthermore, the inclusion of spin–orbit relativistic effects may be enough to change the ordering of relative Gibbs free energy results in the gas phase because many of the low-energy isomers are so closely spaced in energy. This is less likely in solution due to the larger gaps in relative Gibbs free energies. However, with all of the U^{VI} structures analyzed being of the f^0 type, spin–orbit effects may not be a significant factor.

CHAPTER FOUR

A COMPUTATIONAL DENSITY FUNCTIONAL STUDY OF POLYPYRROLIC MACROCYCLES: ANALYSIS OF ACTINYL–OXO TO 3d TRANSITION METAL BONDING

4.1 Introduction

Transition metals, lanthanides, and actinides are being used more and more often as targets for the multidentate chelating abilities of macrocyclic ligands such as crown ethers, calixarenes, expanded–porphyrins, and phthalocyanines. Growing interest in complexing early actinides and their actinyls has been created due to the possibilities for the selective extraction of their radionuclides. The ability to vary ring size and to alter the identity of donor atoms has also resulted in the possibility for the tailoring of specific cations and oxidation states within the ligand cavities of such structures.

Recent experimental investigations, by Edinburgh research team, [123, 156, 126] into polypyrrolic macrocycles [118-123] are reminiscent structurally of Pac–Man cofacial diporphyrins [124], that can accommodate a range of d- and f-block metals of various oxidation states. Such structures exhibit an abundance of chemical variation and are thought to offer potential chemical advantages. The binucleating Schiff–base calixpyrroles investigated possess the beneficial coordinative features of the pyrrole group along with the exceptional design characteristics and synthetic versatility of Schiff–base condensation procedures.

These experimental efforts [125, 126] have shown that the transamination reaction between **H_4L** (Figure 4–1) and the uranyl amide $[UO_2(thf)_2\{N(SiMe_3)_2\}_2]$ in THF at low temperature leads to the formation of a hinged complex which accommodates only one linear uranyl (UO_2^{2+}) **$U^{VI}O_2$1** within two available polypyrrolic cavities. The two aryl-groups of the polypyrrolic macrocycle function as hinges within a rigid molecular cleft-like structure in which the uranyl–endo–oxygen is hydrogen bonded to two adjacent pyrrolic hydrogens of the vacant N_4 cavity. Further reaction with $[M\{N(SiMe_3)_2\}_2]$ (M = Mn **2**, Fe **3**, and Co **4**) produces **$U^{VI}O_2$2–4**, shown as **2–4** in Figure 4–1.

Figure 4–1. Synthesis of uranyl transition metal complexes **2 – 4**. Copyright permission obtained from Polly Arnold/University of Edinburgh on 01/08/08 [125, 126].

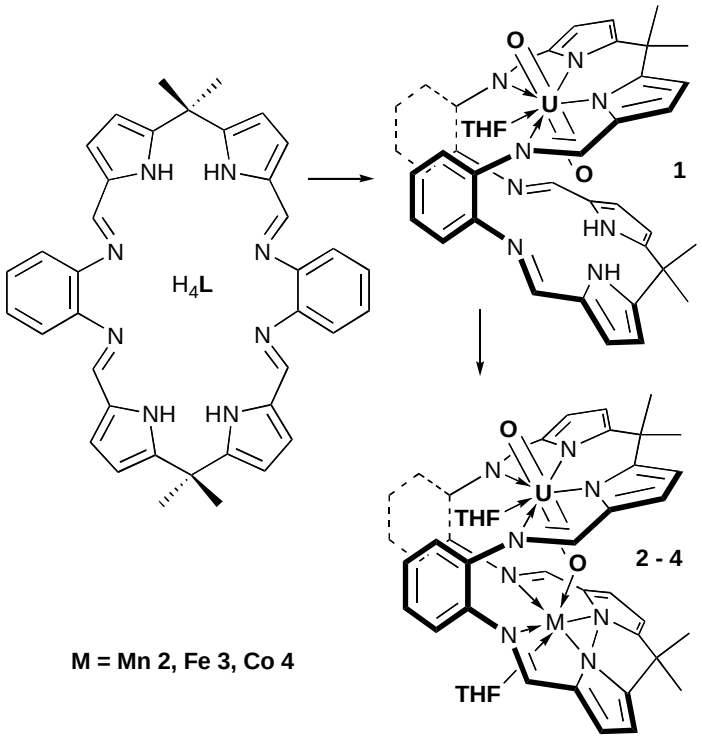

Crystals of $\mathbf{U^{VI}O_2 1}$, **2** and **4** were suitable for X–ray diffraction studies, whereas those of $\mathbf{U^{VI}O_2 3}$ were found to be too weakly diffracting to yield useful structural information. The most striking structural discovery, identified for the first time within the $\mathbf{U^{VI}O_2 2–4}$ isostructural bimetallic complexes, was the interaction between the uranyl– endo–oxygen and the 3d transition metal. In addition, the $\mathbf{An^{VI}O_2 5}$ and $\mathbf{An^{V}O_2 5^{-}}$ TM complexes containing Zn were studied computationally.

Other than polypyrrolic macrocycles, such structures can also be classified as "cation-cation" and "bimetallic". Actinyl cation-cation interactions are an uncommon but important feature in neptunyl [127] and plutonyl chemistry [128], and are even less commonly found in uranyl complexes [129]. Bimetallic complexes containing an actinide and a 3d transition metal are also considered to be rare and are more commonly found with a bridging ligand situated between the two metals [130]. Complexes with two centres of reactivity offer the potential for variations and improvements in new and existing reaction chemistry and catalysis by transition metals.

Our primary aim is to investigate the nature of bonding within these new complexes for the purpose of adding to the existing knowledge of these three classifications: polypyrrolic macrocycle, cation-cation, and bimetallic complexes. In particular, we are looking to exploit the actinyl–oxo group desymmetrization created by the bonding of the actinyl–endo–oxygen to the dicationic transition metals: Mn^{II}, Fe^{II}, Co^{II}, and Zn^{II}. Access to the selective chemical reactivity of one of the actinyl oxygens would be a desirable addition to the understanding of the speciation of the early actinides found in the nuclear fuel cycle and radioactive wastes. Also, as a goal, we are looking to extend the experimentally known chemistry of the $U^{VI/V}$, $Np^{VI/V}$, and $Pu^{VI/V}$ series

through observations of period trends in structure variations, redox potentials, energetics, harmonic vibrations, etc., not all of which we were able to cover within this work.

After outlining our methods of calculation below we begin our results and discussion section with a brief general discussion of our interpretation of calculations of bond angles, bond lengths, bond orders, and atomic charges for 30 structures across both the actinyl (VI) and (V) and the transition metal series of elements. We conclude our investigation with a comparison of calculated oxidation–reduction (redox) potentials [131].

4.2 Methods of Calculation

Since the largest structures studied contain 108 atoms, the calculation requirements limit us to the use of only a few theoretical and computational methods that allow for the completion of calculations in a reasonable amount of time.

With the inclusion of electron correlation, DFT [28, 29, 132] is known to have definite advantages for transition metals and actinides while often offering a significant time saving advantage over comparable *ab initio* methods. Gradient corrected calculations with the PBE [36] exchange–correlation (XC) functional offer additional time savings over the popular B3LYP [37, 38, 86] hybrid functional; while on average providing slightly less accurate Gibbs free energies [87], the PBE functional is often found to provide as accurate geometries and vibrational frequencies. Furthermore, additional time is saved with the incorporation of resolution–of–identity (RI) [44]

approximation methods, where an auxiliary basis set is used to improve the computational efficiency of the Priroda code [40, 44, 51-53]. Recent development of accurate relativistic methods has also played a significant part in the ability to model such structures accurately. Our research group has been able to verify the accuracy of three separate relativistic methods for a variety of actinide containing complexes [87-89, 95]: the all-electron (AE) scalar four–component method (Priroda), the ZORA (zero order regular approximation) [49, 54-56] method (ADF) [35], and the Stuttgart–Dresden SC– ECP (small-core effective core potential) method of Küchle et al. [57] (Gaussian). As for solvation methods we have gained confidence in using both the ADF–COSMO (conductor-like screening model) [34, 59, 60] and the Gaussian C–PCM (conductor polarized continuum model) [61] to calculate single-point energies. Lastly, the incorporation of Hay spin–orbit coupling and multiplet *ad hoc* corrections [58] have been determined to be necessary to obtained accurate oxidation–reduction potentials in solution. The remainder of this section outlines the methods we chose to use and includes relevant references for those interested in more detailed discussions.

Unconstrained gas-phase geometry optimizations were performed using version 5 of the Priroda program (p5) [40, 44, 51-53]. The Priroda code employs a fast RI method for calculating both Coulomb and exchange–correlation (XC) integrals with optimized fitted Gaussian basis sets. For relativistic effects in p5 an AE scalar four–component process was applied where all spin–orbit terms are separated out from the scalar terms [40, 50] and neglected [40, 44, 51-53]. Calculations with p5 were made using the gradient corrected PBE XC functional and the correlation consistent polarized valence triple zeta (cc–pVTZ) [40] Gaussian basis set. Harmonic vibrational frequencies were calculated to

obtain thermochemistry data, such as Gibbs free energies and zero-point energy corrections and also to verify the nature of stationary points of optimized geometries.

Systems with unpaired electrons used an unrestricted, open-shell Kohn–Sham formalism. The multiplicities (2S + 1) were determined based on TM's with weak field/high spin tetrahedral coordination of crystal field theory. Four categories of orbital occupations are found to occur for the bimetallic complexes being investigated: (1) where no unpaired electrons are found on either metal in the $\mathbf{U^{VI}O_2 1}$ and $\mathbf{U^{VI}O_2 5}$ complexes, (2) where unpaired electrons are found only on the actinide metal in the $\mathbf{U^{V}O_2 1,5^{-}}$, $\mathbf{Np^{VI}O_2 1,5}$, $\mathbf{Np^{V}O_2 1,5^{-}}$, $\mathbf{Pu^{VI}O_2 1,5}$, and $\mathbf{Pu^{V}O_2 1,5^{-}}$ complexes, (3) where unpaired electrons are found only on the TM in the $\mathbf{U^{VI}O_2 2–4}$ complexes, and (4) where unpaired electrons are found on both metals at the same time in the remaining TM complexes. In such cases, placement of the unpaired electrons within the chosen weak field tetrahedral crystal field environment, were taken to be always parallel to each other, due to the difficulties of implementing anti-parallel configurations with the software used. Efforts were made within p5 and ADF to model the distinguishing electron arrangements of these four categories of orbital occupations.

Several previous internal efforts have been made towards establishing the performance of the relativistic AE–DFT calculations with the Priroda code as applied to the simulation of actinide and actinyl molecules. Various test calculations were performed on small molecules such as actinyl cations, actinide fluorides, oxides, and oxofluorides [87] as well as larger molecules such as dinitrogen tetroxide adducts of uranyl nitrate [1], actinyl aquo complexes [88, 89], and various expanded–porphyrins [12, 14-17, 87, 95, 133]. In all such cases Priroda was determined to be an expedient and

reliable code providing essentially the same results as other relativistic methods, provided the same XC functionals and reasonably converged basis sets are used.

Mulliken population density [68] based Mayer bond orders [64, 65] were calculated with p5 using the PBE XC functional. Atomic charges were also determined within p5 with PBE using a method developed by Hirshfeld [66]. Both bond orders and atomic charges are not quantum mechanical observables but have been found to be useful in describing the chemical environment for a variety of actinide and actinyl complexes [1, 87-89, 95].

Reduction potentials for ferrocene and the actinyl series of complexes [58, 88, 89, 134] required the calculation of free energies of solvation with the ADF–COSMO [34, 59, 60] model using thf as the solvent with a dielectric constant of 7.58. The current version of Priroda does not contain continuum solvation models. ADF–COSMO single-point calculations, with an integration parameter of 5.5, were therefore performed on the p5–optimized geometries with the same relativistic method, XC functional, basis set, and conditions as described above (ADF ZORA/PBE/TZP/COSMO). Klamt radii were used for the main group atoms (O = 1.72 Å, N = 1.83 Å, C = 2.00 Å, and H = 1.30 Å) [59]. Radii of 1.50 Å for all TM's and 1.70 Å for all An's were also used [95]. Although there is in fact some variation in the radii along each of the metal series, it is thought that with each of the metals being either coordinated or sterically hindered on all sides within the two cavities that the variation in radii across each of the metal series would have minimal effect on calculations in solution.

The reduction of the $\mathbf{An^{VI}O_21}$ complexes leads to the anionic pentavalent $\mathbf{An^{V}O_21^-}$ complexes described in the following redox half reaction (reaction 4–1). The

complementary ferrocenium/ferrocene half-reaction is then used to balance the electron transfer reaction (reaction 4–2).

$$\mathbf{An^{VI}O_2 1} + \mathbf{e^-} \rightarrow \mathbf{An^{V}O_2 1^-} \qquad \textbf{(4–1)}$$

$$\mathbf{Cp_2Fe^+} + \mathbf{e^-} \rightarrow \mathbf{Cp_2Fe} \qquad \textbf{(4–2)}$$

The inclusion of "Hay corrections", based on model spin–orbit CI calculations [58], are found to be necessary. They account for multiplet and spin–orbit effects not included in a single-configuration DFT wave function. Corrections of –0.31, –1.17, and – 0.21 eV were applied for U, Np, and Pu.

4.3 Results and Discussion

4.3.1 Structure

4.3.1.1 Metal Coordination

All 30 calculated structures contain actinides that consistently formed 7– coordinate near pentagonal bipyramids with the actinide metal centrally located within a cavity plane formed by the four ring nitrogens (see, e.g., top front right hand side view of $\mathbf{Pu^{V}O_2 2^-}$ complex, Figure 4–2). The other coordination sites are filled by the two axial actinyl oxygens and the oxygen of an equatorial coordinating thf solvent molecule.

Figure 4–2. Optimized complexes of Case 1 $\mathbf{Pu^{V}O_{2}2^{-}}$ (top views) and Case 2 $\mathbf{Pu^{VI}O_{2}2}$ (bottom views) (magenta Pu, green Mn^{II}, red O, blue N, grey C, and H excluded)

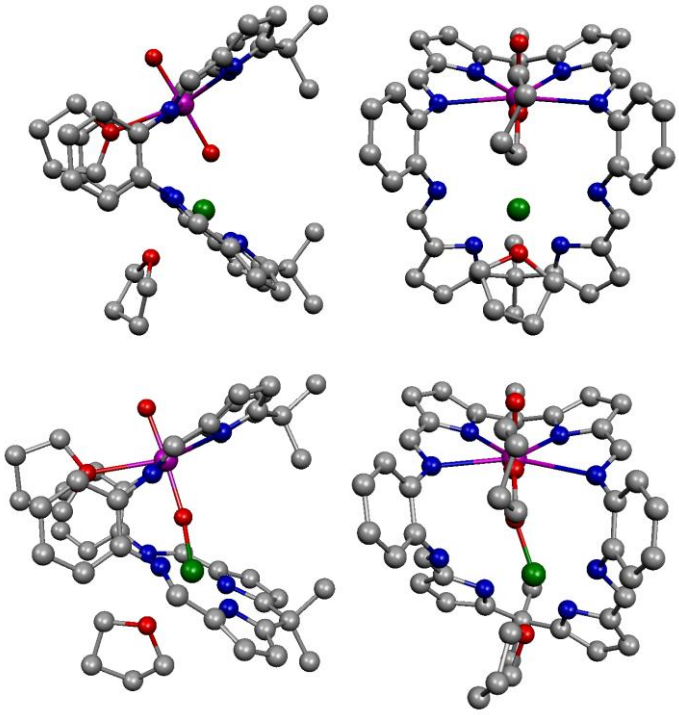

The predominant structural formation of the second cavity, case 1, is thought to be a 4-coordinate transition metal. Case 1 is found to account for 16 of the 24 TM complexes. The strong coordination of the two pyrrolic nitrogens and intermediate coordination to both the thf solvent molecule, and the actinyl–endo oxygen form a near tetrahedral coordination. Whereas, the two Schiff–base nitrogens are thought to have minimal bonding effects at distances of ≥ 2.599 Å from the TM centers ($\mathbf{Pu^{V}O_{2}2^{-}}$ complex, top views, Figure 4–2).

The remaining eight transition metal complexes make up the other two special cases. Case 2, has a much stronger bonding to one of the Schiff–base nitrogens. The following three complexes: $\mathbf{Np^{VI}O_{2}2}$, $\mathbf{Pu^{VI}O_{2}2}$, and $\mathbf{Pu^{VI}O_{2}3}$ are examples of case 2 (bottom views of Figure 4–2). Whereas, case 3, has no TM–THF bond, and is seen in the following complexes: $\mathbf{U^{V}O_{2}3^{-}}$, $\mathbf{Np^{V}O_{2}3^{-}}$, $\mathbf{Pu^{V}O_{2}3^{-}}$, $\mathbf{U^{V}O_{2}5^{-}}$, and $\mathbf{U^{V}O_{2}5^{-}}$ (Figure 4–3).

Figure 4–3. Optimized Case 3 complex of $\mathbf{U^{V}O_{2}3^{-}}$ (side and front view, brown Fe^{II})

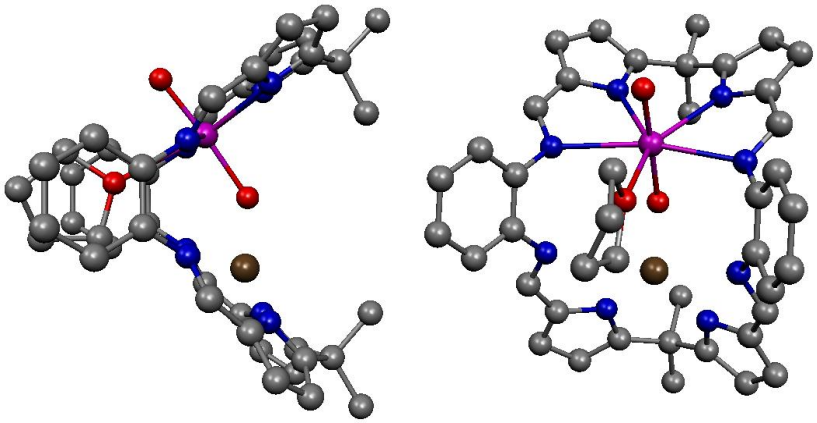

The O2–M–O4 bond angle of the cases 1 and 2 TM structures provides us with a measure of the near tetrahedral formation created between the two oxygens and two pyrrolic nitrogens within these complexes, Table 4–1. The O2–M–O4 bond angle is seen to range from 122.5 to 140.5º compared to 109.5º for purely tetrahedral formations.

Table 4–1. Gas-phase bond angles for $\mathbf{An^{VI}O_21–5}$ and $\mathbf{An^{V}O_21–5^-}$ **c**omplexes (degrees)[a]

complexes	O1–An –O2	N1–An –O3	N1,3–An –N2,4	N2–An –N3	An–O2 –M	O2–M –O4	Cofacial angle[e]
$\mathbf{U^{VI}O_21}$	175.3	77.3	67.0(0)	70.3			57.0(1)
exptl.[b]	177.6	76.6	66.8(1)	71.1			
$\mathbf{U^{V}O_21^-}$	175.7	78.3	65.4(1)	70.3			56.3(1)
$\mathbf{Np^{VI}O_21}$	178.1	76.5	67.3(1)	71.2			56.7(0)
$\mathbf{Np^{V}O_21^-}$	176.5	78.2	65.1(0)	70.3			56.2(1)
$\mathbf{Pu^{VI}O_21}$	179.2	77.9	66.2(1)	69.9			56.3(1)
$\mathbf{Pu^{V}O_21^-}$	177.2	78.6	65.2(0)	70.0			56.1(1)
$\mathbf{U^{VI}O_22}$	175.9	76.9	67.8(2)	70.9	147.5	137.6	60.9(2)
exptl.[b]	177.4	76.7	68.5(6)	71.4			
$\mathbf{U^{V}O_22^-}$	176.4	78.0	66.5(1)	71.5	144.1	137.1	62.9(1)
$\mathbf{Np^{VI}O_22}$[c]	177.4	76.8	67.7(4)	71.6	147.1	139.5	59.4(9)
$\mathbf{Np^{V}O_22^-}$	176.8	77.9	66.8(1)	71.5	144.7	137.5	62.0(1)
$\mathbf{Pu^{VI}O_22}$[c]	175.6	78.7	66.6(4)	71.2	161.6	124.9	56.3(43)
$\mathbf{Pu^{V}O_22^-}$	178.1	78.3	66.7(1)	70.8	142.4	139.1	62.3(1)
$\mathbf{U^{VI}O_23}$	178.0	76.8	67.6(2)	71.1	144.9	140.1	59.3(2)
$\mathbf{U^{V}O_23}$[d]	175.7	78.2	66.4(0)	70.1	143.7	none	64.5(1)
$\mathbf{Np^{VI}O_23}$	179.3	76.6	67.6(3)	71.4	145.6	140.1	58.8(1)
$\mathbf{Np^{V}O_23}$[d]	178.3	77.7	66.7(0)	70.9	142.7	none	63.6(2)
$\mathbf{Pu^{VI}O_23}$[c]	176.7	77.8	67.1(5)	71.3	151.5	136.3	57.8(30)
$\mathbf{Pu^{V}O_23}$[d]	179.5	77.9	66.6(1)	70.5	141.3	none	63.7(1)
$\mathbf{U^{VI}O_24}$	175.0	76.9	67.6(2)	70.8	153.4	132.2	58.5(0)
exptl.[b]	177.6	76.3	67.3(3)	71.6			
$\mathbf{U^{V}O_24^-}$	175.8	78.0	66.2(1)	71.2	148.5	133.1	60.1(1)
$\mathbf{Np^{VI}O_24}$	178.4	76.3	67.6(1)	71.4	150.9	133.6	58.1(0)
$\mathbf{Np^{V}O_24^-}$	176.8	77.9	66.4(1)	70.9	147.0	134.1	60.1(2)
$\mathbf{Pu^{VI}O_24}$	178.8	77.9	66.8(1)	69.7	148.2	134.9	59.1(1)
$\mathbf{Pu^{V}O_24^-}$	178.0	78.2	66.4(1)	70.5	145.7	135.2	59.8(1)
$\mathbf{U^{VI}O_25}$	174.4	77.0	67.6(1)	70.6	159.5	122.5	59.0(0)
$\mathbf{U^{V}O_25}$[d]	175.4	78.3	66.3(1)	70.1	147.4	none	63.9(1)
$\mathbf{Np^{VI}O_25}$	178.0	76.4	67.6(1)	71.4	156.1	124.3	58.8(1)
$\mathbf{Np^{V}O_25}$[d]	178.7	77.6	66.5(1)	70.7	144.8	none	63.4(1)
$\mathbf{Pu^{VI}O_25}$	178.6	78.1	66.8(1)	69.7	153.2	125.5	59.9(0)
$\mathbf{Pu^{V}O_25^-}$	178.2	78.2	66.4(1)	70.5	150.4	127.1	61.0(0)

[a]O1 exo, O2 endo, O3 An thf, O4 M thf , M = Mn **2**, Fe **3**, Co **4**, and Zn **5**, bFor preceeding complex, reference [126], [c]case 2 (3 short M–N bonds), [d]case 3 (no M–O4 bond), [e]Brackets contain maximum deviation from average, see text for definition

4.3.1.2 Bond Angles, Bond Lengths, Bond Orders and Atomic Charges

The nature of An=O bonding in early actinide complexes is considered to be quite complicated as suggested by the discussion of electronic configurations. The same linear structure is seen for both AnO_2^{2+} and AnO_2^{+} but with longer metal–oxygen bonds found in AnO_2^{+} due to the reduced charge on the metal (Table 4–2). A decrease in the strength accompanied by a shorter An=O bond is seen along the actinide series with increasing atomic number. One might have expected, that with the shorter An=O bond length created by the increase in the density of nuclear charge across the An series, a stronger bond would have formed, but a weakening of the bond occurs due to the previously mentioned 'actinide contraction' of the 5f orbitals [135].

In general, the early actinides are best viewed as being intermediates between the strongly ionic bonding lanthanides and the more covalent bonding d-block transition elements. For the most part actinyl–ligand bonds in the equatorial or nearly in the equatorial plane are determined by a combination of the electrostatic attraction to the actinide, electrostatic repulsions between ligands, and steric demands around the metal center. Such bonds are usually described as predominantly ionic in nature and are often relatively weak and kinetically labile in solution [2].

The structural data gathered from X–ray diffraction measurements for three of the uranyl complexes were used to gauge the accuracy of the gas-phase calculations in reproducing the solid-state experimental geometries. For the $\mathbf{U^{VI}O_2}$**1** structure, the five bond angles measured had a mean deviation between theory and experiment of 0.9°, with

the largest deviation of 2.3° found for the O=U=O angle (Table 4–1). Whereas, for the seven bond lengths compared with experiment a mean deviation of 0.030 Å was obtained (Table 4–2). This is considered to be a reasonably good result and in line with previous results obtained for other polypyrrolic macrocyclic ligands [95].

Table 4–2. Gas-phase bond lengths for $\mathbf{An^{VI}O_21}$ and $\mathbf{An^{V}O_21^-}$ complexes (Å)[a]

complex	An=O1	An=O2	An–O3	An–N1,4[c]	An–N2,3
$\mathbf{U^{VI}O_21}$	1.799	1.835	2.484	2.609(1)	2.466(1)
exptl.[b]	1.766	1.790	2.442	2.586(8)	2.443(1)
$\mathbf{U^{V}O_21^-}$	1.825	1.886	2.553	2.702(2)	2.531(1)
$\mathbf{Np^{VI}O_21}$	1.783	1.817	2.468	2.615(0)	2.452(0)
$\mathbf{Np^{V}O_21^-}$	1.817	1.890	2.586	2.723(3)	2.540(0)
$\mathbf{Pu^{VI}O_21}$	1.784	1.821	2.505	2.643(4)	2.490(1)
$\mathbf{Pu^{V}O_21^-}$	1.807	1.870	2.579	2.719(2)	2.535(0)

[a]O1 exo, O2 endo, O3 An thf, [b]For preceeding complex, reference [126], [c]Brackets contain maximum deviation from average, see text for definition

As for the larger $\mathbf{U^{VI}O_22}$ and $\mathbf{U^{VI}O_24}$ structures (108 atoms) the mean angle deviations were found to be 0.8° and 0.9°, respectively (Table 4-1). The total mean deviations of fourteen bonds measured were determined to be 0.066 Å and 0.062 Å (Table 4-4). The larger than expected non-systematic deviations can be attributed to the Mn–N8 bond distance with a deviation of 0.255 Å in the $\mathbf{U^{VI}O_22}$ complex and the Co–N5 bond distance with a deviation of 0.344 Å in the $\mathbf{U^{VI}O_24}$ complex. If these two poor results are neglected the mean deviations become 0.051 Å and 0.040 Å, respectively, becoming reasonably accurate for the DFT methods used.

Beginning with the geometric parameters pertaining to the actinyl fragments, the exo–oxygen containing An=O1 actinyl bond is found to range in length, over 15 hexavalent complexes, from 1.783 to 1.808 Å, and over 15 pentavalent complexes, from

1.807 to 1.842 Å, representing relatively small changes in these bonds, across both series of metals (Tables 4–2 and 4–4). The introduction of the transition metal to the secondary cavity can thus be said to have very little influence on the length of the An=O1 bond. Correspondingly, the very consistent An=O1 bond orders of 2.40 ± 0.02 support this (Tables 4–3 and 4–5).

Table 4–3. Gas-phase Mayer bond orders [64, 65] for $\mathbf{An^{VI}O_21}$ and $\mathbf{An^{V}O_21^-}$ complexes[a]

complex	An=O1	An=O2	An–O3	An–N1,4[b]	An–N2,3
$\mathbf{U^{VI}O_21}$	2.42	2.20	0.41	0.42(1)	0.57(0)
$\mathbf{U^{V}O_21^-}$	2.42	2.05	0.32	0.31(1)	0.47(0)
$\mathbf{Np^{VI}O_21}$	2.40	2.20	0.41	0.40(1)	0.55(0)
$\mathbf{Np^{V}O_21^-}$	2.41	1.99	0.28	0.29(0)	0.45(0)
$\mathbf{Pu^{VI}O_21}$	2.38	2.15	0.36	0.38(1)	0.48(1)
$\mathbf{Pu^{V}O_21^-}$	2.39	2.01	0.28	0.28(0)	0.44(0)

[a]O1 exo, O2 endo, O3 An thf, [b]Brackets contain maximum deviation from average, see text for definition

With the other actinyl bond An=O2 containing the endo–oxygen, a consistently longer bond length, over that of An=O1, is observed either due to O2 hydrogen bonding interactions for the six non-transition metal $\mathbf{An^{VI}O_21}$ and $\mathbf{An^{V}O_21^-}$ complexes, or to an even larger degree, due to the M–O2 transition metal bonding in the 24 $\mathbf{An^{VI}O_22–5}$ and $\mathbf{An^{V}O_22–5^-}$ TM containing structures. The lengthening of the An=O2 bond within these complexes can be interpreted as a desymmetrization of the typically symmetric linear actinyl fragment or in turn as a weakening of the An=O2 actinyl bond. A reduction in bond orders occurs for the hydrogen bonded O2, $\mathbf{An^{VI}O_21}$ and $\mathbf{An^{V}O_21^-}$ species, averaging 2.18 ± 0.03 and 2.02 ± 0.03, respectively (Table 4-3). The bond order decreases further (to less than full double bond) for the transition metal bonded O2,

An^{VI}O$_2$2–5 and **An^{V}O$_2$2–5^{-}** complexes, ranging from 1.97 to 1.44 and 1.76 to 1.59 for each species (Table 4-5). These changes in the actinyl bond can be considered as proof of the presence of a substantial M–O2 interaction.

Continuing with the actinyls, we see that in transitioning from the hexavalent to pentavalent oxidation states bond length increases are due to the reduced charge on the actinide metal. Average increases in An=O1 bond lengths of about 0.030 Å are observed, with the exception of **Pu^{VI}O$_2$2/Pu^{V}O$_2$2^{-}** and **Pu^{VI}O$_2$3/Pu^{V}O$_2$3^{-}** with only slight increases of 0.007 and 0.004 Å. Corresponding small increases in bond orders of 0.27 and 0.16 are also seen for these two Pu transitions in comparison to decreases seen for all other actinyl transitions.

Table 4–4. Gas-phase bond lengths for **$An^{VI}O_2$2–5** and **$An^{V}O_2$2–5$^-$** complexes (Å)[a]

complex	An=O1	An=O2	An–O3	An–N1,4[e]	An–N2,3	An–M	M–O2	M–O4	M–N5	M–N6,7	M–N8
$U^{VI}O_2$2	1.805	1.860	2.535	2.538(4)	2.447(2)	3.770	2.066	2.303	2.599	2.073(10)	2.909
exptl.[b]	1.768	1.808	2.458	2.498(10)	2.426(9)	3.804	2.163	2.217	2.547	2.127(7)	2.654
$U^{V}O_2$2$^-$	1.836	1.931	2.600	2.633(4)	2.498(1)	3.701	1.959	2.466	2.797	2.096(5)	2.937
$Np^{VI}O_2$2[c]	1.800	1.889	2.581	2.555(2)	2.447(6)	3.712	1.982	2.329	2.293	2.032(14)	3.049
$Np^{V}O_2$2$^-$	1.825	1.911	2.621	2.623(5)	2.486(1)	3.694	1.965	2.443	2.762	2.099(6)	2.917
$Pu^{VI}O_2$2[c]	1.808	1.960	2.589	2.575(10)	2.473(3)	3.745	1.834	2.282	2.133	1.962(9)	3.297
$Pu^{V}O_2$2$^-$	1.815	1.904	2.618	2.618(5)	2.492(1)	3.656	1.958	2.431	2.741	2.095(6)	2.906
$U^{VI}O_2$3	1.806	1.890	2.545	2.553(4)	2.450(1)	3.679	1.969	2.227	2.888	2.003(4)	2.720
$U^{V}O_2$3^{-d}	1.842	1.972	2.640	2.620(2)	2.498(1)	3.639	1.858	none	2.997	2.007(2)	3.039
$Np^{VI}O_2$3	1.793	1.878	2.538	2.548(3)	2.444(4)	3.670	1.964	2.213	2.670	2.003(7)	2.901
$Np^{V}O_2$3^{-d}	1.820	1.945	2.621	2.620(6)	2.488(0)	3.605	1.861	none	2.947	2.009(4)	3.041
$Pu^{VI}O_2$3[c]	1.807	1.973	2.649	2.561(11)	2.465(3)	3.677	1.821	2.268	2.111	1.918(13)	3.212
$Pu^{V}O_2$3^{-d}	1.811	1.934	2.623	2.611(3)	2.490(1)	3.576	1.856	none	2.939	2.006(3)	3.007
$U^{VI}O_2$4	1.803	1.859	2.516	2.540(5)	2.450(2)	3.751	1.995	2.150	2.790	1.969(3)	2.930
exptl.[b]	1.771	1.785	2.475	2.525(12)	2.412(10)	3.689	2.080	2.151	2.446	1.988(15)	3.003
$U^{V}O_2$4$^-$	1.835	1.935	2.593	2.636(5)	2.505(1)	3.697	1.907	2.234	2.914	1.982(2)	2.997
$Np^{VI}O_2$4	1.789	1.847	2.508	2.542(6)	2.444(2)	3.715	1.991	2.152	2.775	1.970(4)	2.927
$Np^{V}O_2$4$^-$	1.822	1.916	2.612	2.629(4)	2.502(2)	3.673	1.915	2.224	2.911	1.981(0)	2.959
$Pu^{VI}O_2$4	1.788	1.854	2.535	2.545(8)	2.490(1)	3.676	1.968	2.154	2.752	1.971(7)	2.946
$Pu^{V}O_2$4$^-$	1.812	1.903	2.610	2.621(5)	2.500(1)	3.650	1.916	2.220	2.871	1.981(2)	2.960
$U^{VI}O_2$5	1.802	1.858	2.499	2.545(4)	2.450(1)	3.814	2.018	2.244	2.921	1.964(3)	3.025
$U^{V}O_2$5^{-d}	1.842	1.958	2.628	2.636(1)	2.503(1)	3.675	1.871	none	3.140	1.967(2)	3.152
$Np^{VI}O_2$5	1.787	1.844	2.493	2.549(5)	2.443(1)	3.783	2.022	2.247	2.903	1.967(3)	3.019
$Np^{V}O_2$5^{-d}	1.817	1.931	2.611	2.636(1)	2.496(2)	3.631	1.879	none	3.133	1.967(1)	3.129
$Pu^{VI}O_2$5	1.786	1.848	2.518	2.575(26)	2.491(0)	3.749	2.006	2.252	2.898	1.965(0)	3.022
$Pu^{V}O_2$5$^-$	1.809	1.896	2.591	2.628(5)	2.499(1)	3.700	1.930	2.460	2.980	1.980(2)	3.051

[a]O1 exo, O2 endo, O3 An thf, O4 M thf , M = Mn **2**, Fe **3**, Co **4**, Zn **5**, [b]For preceeding complex, reference [126], [c]case 2 (3 short M–N bonds), [d]case 3 (no M–O4 bond), [e]Brackets contain maximum deviation from average, see text for definition

Table 4–5. Gas-phase Mayer bond orders [64, 65] for **$An^{VI}O_2$2–5** and **$An^{V}O_2$2–5$^-$** complexes[a]

complex	An=O1	An=O2	An–O3	An–N1,4[d]	An–N2,3	An–M	M–O2	M–O4	M–N5	M–N6,7	M–N8
$U^{VI}O_2$2	2.41	1.97	0.38	0.44(0)	0.56(1)	0.19	0.36	0.29	0.29	0.52(0)	0.20
$U^{V}O_2$2$^-$	2.42	1.74	0.30	0.33(1)	0.47(0)	0.16	0.56	0.23	0.21	0.49(0)	0.18
$Np^{VI}O_2$2[b]	2.41	1.80	0.33	0.39(1)	0.52(1)	0.38	0.54	0.29	0.38	0.54(0)	0.16
$Np^{V}O_2$2$^-$	2.40	1.76	0.28	0.32(1)	0.46(0)	0.16	0.54	0.24	0.23	0.49(0)	0.19
$Pu^{VI}O_2$2[b]	2.40	1.47	0.30	0.35(1)	0.49(1)	0.18	0.79	0.33	0.46	0.61(1)	0.10
$Pu^{V}O_2$2$^-$	2.38	1.74	0.28	0.32(0)	0.45(0)	0.18	0.54	0.24	0.24	0.50(0)	0.20
$U^{VI}O_2$3	2.42	1.83	0.37	0.42(1)	0.55(0)	0.50	0.48	0.32	0.25	0.59(1)	0.20
$U^{V}O_2$3$^-$[c]	2.41	1.59	0.30	0.35(0)	0.49(0)	0.18	0.69	none	0.16	0.58(0)	0.15
$Np^{VI}O_2$3	2.41	1.82	0.36	0.42(0)	0.54(0)	0.52	0.48	0.33	0.27	0.60(0)	0.20
$Np^{V}O_2$3$^-$[c]	2.41	1.60	0.30	0.34(1)	0.47(1)	0.18	0.68	none	0.18	0.58(0)	0.15
$Pu^{VI}O_2$3[b]	2.40	1.44	0.29	0.36(1)	0.49(1)	0.18	0.81	0.33	0.46	0.65(1)	0.33
$Pu^{V}O_2$3$^-$[c]	2.39	1.59	0.29	0.33(0)	0.46(0)	0.20	0.68	none	0.19	0.58(0)	0.16
$U^{VI}O_2$4	2.42	1.95	0.39	0.45(0)	0.56(0)	0.14	0.39	0.34	0.21	0.59(0)	0.17
$U^{V}O_2$4$^-$	2.42	1.72	0.30	0.33(1)	0.47(0)	0.16	0.60	0.29	0.16	0.56(0)	0.14
$Np^{VI}O_2$4	2.40	1.93	0.38	0.44(0)	0.54(0)	0.15	0.40	0.34	0.22	0.58(1)	0.17
$Np^{V}O_2$4$^-$	2.41	1.74	0.28	0.32(0)	0.46(0)	0.16	0.57	0.30	0.17	0.56(0)	0.15
$Pu^{VI}O_2$4	2.38	1.88	0.34	0.42(1)	0.47(1)	0.17	0.43	0.34	0.22	0.58(0)	0.16
$Pu^{V}O_2$4$^-$	2.38	1.73	0.28	0.32(0)	0.45(0)	0.17	0.56	0.30	0.18	0.56(0)	0.16
$U^{VI}O_2$5	2.42	1.95	0.39	0.46(1)	0.57(0)	0.10	0.38	0.29	0.14	0.57(1)	0.12
$U^{V}O_2$5$^-$[c]	2.42	1.64	0.30	0.35(0)	0.49(0)	0.14	0.64	none	0.09	0.58(0)	0.09
$Np^{VI}O_2$5	2.41	1.94	0.38	0.44(0)	0.55(0)	0.10	0.38	0.29	0.15	0.56(0)	0.12
$Np^{V}O_2$5$^-$ [c]	2.42	1.65	0.29	0.33(0)	0.47(0)	0.14	0.62	none	0.10	0.58(0)	0.09
$Pu^{VI}O_2$5	2.39	1.89	0.34	0.42(0)	0.48(0)	0.11	0.40	0.29	0.15	0.56(1)	0.12
$Pu^{V}O_2$5$^-$	2.39	1.75	0.28	0.32(0)	0.45(0)	0.13	0.53	0.22	0.12	0.54(0)	0.11

[a]O1 exo, O2 endo, O3 An thf, O4 M thf , M = Mn **2**, Fe **3**, Co **4**, Zn **5**, [b]case 2 (3 short M–N bonds), [c]case 3 (no M–O4 bond),
[d]Brackets contain maximum deviation from average, see text for definition

As for the Hirshfeld atomic charges on these two plutonium metal complexes they are found to increase by 0.04 and 0.02 e with increased valency compared to an average increase for the other valency transitions of 0.08 ± 0.03 e (Tables 4–6 and 4–7).

Table 4–6. Gas-phase Hirshfeld atomic charges [66] for $\mathbf{An^{VI}O_21}$ and $\mathbf{An^{V}O_21^-}$ complexes (e)[a]

complex	An	O1	O2	AnO_2	O3	N1,2,3,4[b]	N5,8	N6,7
$\mathbf{U^{VI}O_21}$	0.56	–0.29	–0.29	–0.02	–0.06	–0.11(1)	–0.12(1)	–0.02(0)
$\mathbf{U^{V}O_21^-}$	0.45	–0.35	–0.33	–0.23	–0.06	–0.11(1)	–0.11(0)	–0.02(0)
$\mathbf{Np^{VI}O_21}$	0.48	–0.26	–0.27	–0.05	–0.05	–0.10(1)	–0.12(1)	–0.02(0)
$\mathbf{Np^{V}O_21^-}$	0.37	–0.33	–0.32	–0.28	–0.06	–0.10(1)	–0.10(0)	–0.02(0)
$\mathbf{Pu^{VI}O_21}$	0.40	–0.25	–0.26	–0.11	–0.06	–0.10(2)	–0.11(0)	–0.02(0)
$\mathbf{Pu^{V}O_21^-}$	0.33	–0.31	–0.30	–0.28	–0.06	–0.10(1)	–0.10(0)	–0.02(0)

[a]O1 exo, O2 endo, O3 An thf, [b]Brackets contain maximum deviation from average, see text for definition

Taking a closer look at the actinyl fragment charges we find that the $An^{VI}O_2$ fragments have charges of nearly 0 e with the exception of $\mathbf{Pu^{VI}O_22,3,5}$ with –0.15, – 0.12, and –0.10 e, respectively. This is not the case for the $An^{V}O_2$ fragments which are found to have fragment charges of between –0.17 and –0.28 e with only one exception for $\mathbf{Np^{V}O_23^-}$ with charge of –0.08 e. In comparison to the formal charges of the actinyl fragments (+2 and +1, respectively), one can see that substantial charge transfer from the equatorial ligands has taken place. This charge transfer suggests that a much larger degree of covalent bonding may be involved, between the actinyl units and the macrocyclic ligand, than that of the ionic model on which these structures were initially based.

Table 4–7. Gas-phase Hirshfeld atomic charges [66] for **An^{VI}O$_2$2–5** and **An^{V}O$_2$2–5**$^{-}$ complexes (e)[a]

complex	An	O1	O2	AnO_2	O3	N1,2,3,4[d]	M	O4	N5,6,7,8
U^{VI}O$_2$2	0.56	–0.29	–0.26	+0.01	–0.06	–0.10(1)	0.28	–0.07	–0.11(1)
**U^{V}O$_2$2**$^{-}$	0.44	–0.37	–0.31	–0.24	–0.06	–0.10(1)	0.27	–0.07	–0.10(1)
Np^{VI}O$_2$2[b]	0.46	–0.28	–0.26	–0.08	–0.06	–0.10(1)	0.31	–0.07	–0.10(2)
**Np^{V}O$_2$2**$^{-}$	0.39	–0.34	–0.29	–0.24	–0.06	–0.10(1)	0.27	–0.07	–0.10(1)
Pu^{VI}O$_2$2[b]	0.38	–0.27	–0.26	–0.15	–0.06	–0.10(1)	0.32	–0.07	–0.09(2)
**Pu^{V}O$_2$2**$^{-}$	0.34	–0.31	–0.27	–0.24	–0.06	–0.10(1)	0.27	–0.07	–0.10(1)
U^{VI}O$_2$3	0.55	–0.29	–0.27	–0.01	–0.06	–0.10(1)	0.28	–0.06	–0.10(1)
**U^{V}O$_2$3**$^{-}$[c]	0.48	–0.35	–0.30	–0.17	–0.06	–0.11(1)	0.25	none	–0.10(1)
Np^{VI}O$_2$3	0.47	–0.27	–0.25	–0.05	–0.06	–0.10(1)	0.29	–0.06	–0.10(1)
**Np^{V}O$_2$3**$^{-}$[c]	0.42	–0.32	–0.28	–0.08	–0.06	–0.11(1)	0.25	none	–0.10(1)
Pu^{VI}O$_2$3[b]	0.39	–0.26	–0.25	–0.12	–0.07	–0.10(1)	0.25	–0.06	–0.07(3)
**Pu^{V}O$_2$3**$^{-}$[c]	0.37	–0.29	–0.26	–0.18	–0.06	–0.11(1)	0.26	none	–0.10(1)
U^{VI}O$_2$4	0.57	–0.29	–0.25	+0.03	–0.06	–0.10(1)	0.21	–0.05	–0.10(1)
**U^{V}O$_2$4**$^{-}$	0.44	–0.36	–0.30	–0.22	–0.06	–0.10(1)	0.20	–0.05	–0.10(1)
Np^{VI}O$_2$4	0.48	–0.26	–0.23	–0.01	–0.05	–0.10(1)	0.21	–0.05	–0.10(1)
**Np^{V}O$_2$4**$^{-}$	0.40	–0.33	–0.28	–0.21	–0.06	–0.10(1)	0.20	–0.05	–0.10(1)
Pu^{VI}O$_2$4	0.41	–0.25	–0.22	–0.06	–0.06	–0.09(1)	0.21	–0.05	–0.10(1)
**Pu^{V}O$_2$4**$^{-}$	0.35	–0.30	–0.26	–0.21	–0.06	–0.10(1)	0.21	–0.05	–0.10(1)
U^{VI}O$_2$5	0.56	–0.28	–0.27	+0.01	–0.06	–0.11(1)	0.38	–0.07	–0.12(1)
**U^{V}O$_2$5**$^{-}$[c]	0.46	–0.35	–0.33	–0.22	–0.06	–0.11(1)	0.41	none	–0.11(1)
Np^{VI}O$_2$5	0.48	–0.26	–0.25	–0.03	–0.05	–0.10(1)	0.39	–0.08	–0.11(1)
**Np^{V}O$_2$5**$^{-}$[c]	0.40	–0.32	–0.31	–0.23	–0.06	–0.10(1)	0.41	none	–0.11(1)
Pu^{VI}O$_2$5	0.40	–0.25	–0.25	–0.10	–0.06	–0.10(1)	0.39	–0.07	–0.11(1)
**Pu^{V}O$_2$5**$^{-}$	0.34	–0.30	–0.28	–0.24	–0.06	–0.11(1)	0.39	–0.08	–0.11(1)

[a]O1 exo, O2 endo, O3 An thf, O4 M thf , M = Mn **2**, Fe **3**, Co **4**, and Zn **5**, [b]case 2 (3 short M–N bonds), [c]case 3 (no M–O4 bond), [d]Brackets contain maximum deviation from average, see text for definition

Although the actinides are found to be nearly planar within the N_4 cavity, the TM's are typically located slightly above the N_4 cavity plane (0.155 Å in the case of **U^{VI}O$_2$3** for example). For the most part consistency is seen for the bond lengths of the pair of cavity pyrrolic nitrogens. The pyrrolic An–N2,3 and M–N6,7 bonds are on average significantly stronger and shorter than their neutral Schiff–base counterparts with An–N1,4 and M–N5,8 bond lengths and distances. The actinide complexes with lower

oxidation states show a noticeable increase in bond lengths for the pyrrolic nitrogens moving closer to the cavity center (equidistant and planar to all four nitrogens) leading to a reduction in Schiff–base nitrogen bond lengths. For the M–N5 and M–N8 distances of the Schiff–base nitrogens we see significant variations in length from being nearly equal in length for $\mathbf{Np^{V}O_{2}3^{-}}$ to having a difference of 1.164 Å for $\mathbf{Pu^{VI}O_{2}2}$.

An offset of the transition metal from the center of the cavity manifests itself in the difference in transition metal to Schiff–base nitrogen bond lengths and is found to occur to varying degrees for most transition metal containing structures. As for the atomic charges on the eight nitrogens of the macrocyclic ligand they are almost always found to be –0.10 ± 0.02 e with the exception of the N6,7 pyrrolic nitrogens of $\mathbf{Pu^{VI}O_{2}3}$ which are –0.06 ± 0.01 e and the N6,7 pyrrolic nitrogens of the vacant cavity for the $\mathbf{An^{VI}O_{2}1}$ complexes which are all –0.02 e.

Bonding of the thf solvent molecules to the actinide or transition metals is considered to be part of the first solvation shell, for cases 1 and 2 and as such the actinide coordination is considered to be a slightly distorted pentagonal bipyramid. The An–O3 bond lengths range from 2.468 to 2.649 Å, with the shortest bond lengths seen in the $\mathbf{An^{VI}O_{2}1}$ complexes. As for the TM to thf bonds, M–O4 = 2.150 to 2.466 Å, they are found to be always shorter, than that of the An–O3 bond, consistent with the difference in size between the 3d TM and the An atom. Comparatively, very little variation is seen for TM complexes with first solvation shell thf coordination to the TM, cases 1 and 2, where bond orders average 0.33 ± 0.08 for An–O3 and 0.29 ± 0.07 for M–O4. The atomic charges on either of the THF oxygens are consistently found to be –0.06 ± 0.01 e.

For case 2 structures, **Np^{VI}O$_2$2**, **Pu^{VI}O$_2$2**, and **Pu^{VI}O$_2$3**, all three instances have TM's significantly more offset from the center of the cavity. In this case, the TM is found to have three strong cavity bonds to nitrogen, instead of two. A key feature of these structures is the shortening of the transition metal to Schiff–base nitrogen bond M–N5, to bond lengths of 2.293, 2.133, and 2.111 Å. Corresponding bond orders are 0.38, 0.46, and 0.46. For these structures there is a noticeable loss of symmetry in the transition metal cavity and substantial distortion can be seen to occur, for example see the comparison between side and front views of **Pu^{V}O$_2$2^{-}** (top) and **Pu^{VI}O$_2$2** (bottom) (Figure 4–2). The differences between the M–N5 and M–N8 bond distances are 0.756, 1.164, and 1.101 Å, respectively, compared to 0.231 Å or less for the remaining TM complexes. These differences can be regarded as a rough indication of the degree to which the metal is offset from center. However, the offset appears to be an inherent feature of these structures as seen from the differences of the two experimental examples tabulated, 0.310 Å for **U^{VI}O$_2$2** and 0.557 Å for **U^{VI}O$_2$4** (Table 4–2). Alternatively, further analysis of these structures without the weekly bound thf solvent molecule attached to the TM, should be checked to verify the lowest Gibbs free energy structure.

Another feature of the case 2 structures is the change in the cofacial angle (formed between the two nearly planar cavities). The cofacial angle is taken as an average of two angles N2–X1–N7 and N3–X2–N6, where X1 and X2 represent dummy atoms placed at the center of each aryl ring. The average cofacial angle for the structures without TM's **An^{VI}O$_2$1/An^{V}O$_2$1^{-}** is 56.4 ± 0.1º with variation from 56.1 ± 0.1º to 57.0 ± 0.1º, while progressively decreasing with An^{VI}/An^{V} valency by 0.7, 0.5, and 0.2º across the actinyl series. With the addition of TM's larger cofacial angles are seen averaging 58.8º and

62.0º for An^{VI} and An^{V} complexes. However, very little variation is seen for complexes containing Mn at (58.9/62.4º), Co (58.6/60.0º) and Zn (59.2/62.8º) for the $An^{VI/V}$ oxidation states in comparison to Fe at (58.6/63.9º). The largest variation between actinyl oxidation states is seen for Case 1 $\mathbf{Pu^{V}O_{2}2^{-}}$ of 62.3 ± 0.1º compared to that of the Case 2 $\mathbf{Pu^{VI}O_{2}2}$ of 56.3 ± 4.3º (Table 4–1). The large deviation from average seen in $\mathbf{Pu^{VI}O_{2}2}$ is an indication of the rather large measure of cofacial angle variation from one side of the TM cavity to the other.

As for the case 3 structures, $\mathbf{U^{V}O_{2}3^{-}}$, $\mathbf{Np^{V}O_{2}3^{-}}$, $\mathbf{Pu^{V}O_{2}3^{-}}$, $\mathbf{U^{V}O_{2}5^{-}}$, and $\mathbf{U^{V}O_{2}5^{-}}$, with no thf–TM bond, the TM's are found to be pulled out of the cavity towards the actinyl–endo–oxygen. For example, Fe of $\mathbf{U^{V}O_{2}3^{-}}$ is 0.674 Å above N_4 cavity plane compared to 0.155 Å for $\mathbf{U^{VI}O_{2}3}$.

Evidence of M–O2 bond formation, for all 24 transition metal containing complexes, of 0.36 to 0.81 for bond orders and 2.066 to 1.821 Å for corresponding bond lengths is observed (Table 4–5). In looking at Figure 4–4 we see that Zn^{II} has the least and Mn^{II} the most variation in M–O2 bond length across the An^{VI} series and Figure 4–5 shows that Np^{VI} has the least and Pu^{VI} the most variation in M–O2 bond length across the TM series. Also, the trend across the An^{V} series of TM's is seen to be nearly constant (with the exception of $\mathbf{Pu^{V}O_{2}5^{-}}$), Figure 4–4. Furthermore, we see decreasing bond length trends of Mn > Zn > Co > Fe for U^{V}, and Zn > Co > Mn > Fe for Np^{V} and Pu^{V}.

Figure 4–4. Variation in M–O2 bond lengths across An^{VI} and An^{V} series with fixed TM

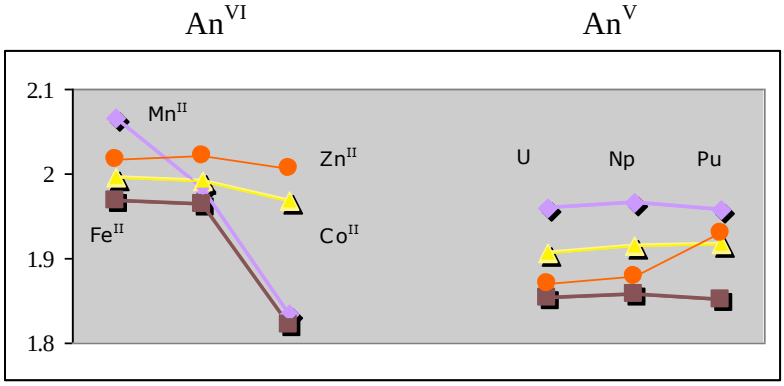

Figure 4–5. Variation in M–O2 bond lengths across TM series with fixed An^{VI} and An^{V}

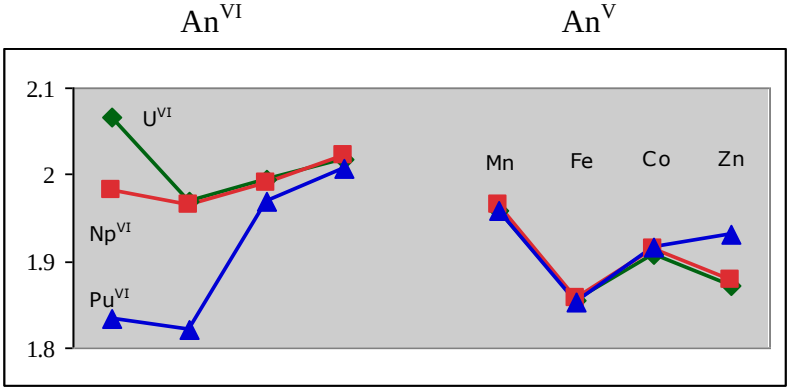

Atomic charge averages for the **AnO_2M** complexes are 0.29 e for Mn, 0.27 e for Fe, 0.21 e for Co, and 0.40 e for Zn. The atomic charges found on manganese, iron, and zinc are found to be consistently higher than those on cobalt. As such, with the case 2 and 3 structural variations identified in the TM complexes found to occur with Mn, Fe and Zn and not with Co, a likely contributing factor is the larger atomic charge found on these three transition metals (Table 4–7).

Measurement of the metal–metal An–M distances was obtained with the intent of determining the proximity that the two metals have to each other within the TM complexes (Table 4–4). The bond orders for three structures, 0.38 for **$Np^{VI}O_2$2**, 0.50 for

$U^{VI}O_2$3, and 0.52 for **$Np^{VI}O_2$3** are indicative of a significant amount of charge built up between the two metals suggesting the possibility of bond formation. Comparatively, An–M bond orders of only 0.17 ± 0.03 are seen for all other TM complexes, which can be interpreted as no bond formation. With the corresponding actinide to transition metal bond distances of 3.712, 3.679, and 3.670 Å it is thought that these bond orders are an artifact of the calculation method and that no bonds exist between the An and TMs.

The An–O2–M bond angle is seen to remain fairly rigid for the majority of the structures with the lowest angle 141.3º occurring for the **$Pu^{VI}O_2$3$^-$** complex and the largest angle 161.6º occurring for the highly distorted **$Pu^{VI}O_2$2** relative to the average of 144.9º for the six case 1 complexes containing Mn and Fe. However, both the Co and Zn TM complexes have larger An–O2–M average bond angle at 149.0º and 154.8º, respectively, for the case 1 complexes (Table 4–1).

4.3.2 Oxidation and Reduction Potentials

For the ferrocenium/ferrocene half–reaction (reaction 4–4) we obtained a gas-phase reduction potential of –5.27 eV. Calculated values for the **$An^{VI}O_2$1/$An^{V}O_2$1$^-$** series of redox potentials were –1.67, –0.02, and –0.47 eV relative to the Fc^+/Fc couple after taking into account the corresponding Hay corrections (Table 4–8).

Table 4–8. Gas-phase energies p5 and oxidation reduction potentials (p5 and ADF) for $\mathbf{An^{VI}O_21/An^{V}O_21^-}$ couples (eV)

Redox half reactions	ΔE_{298}	ΔG_{298}	ΔG_{solv}	vs Fc^+/Fc[a]	+Hay[b]$_{corr}$
$\mathbf{U^{VI}O_21} + e^- \rightarrow \mathbf{U^{V}O_21^-}$	–1.72	–1.85	–3.29	–1.98	–1.67
$\mathbf{Np^{VI}O_21} + e^- \rightarrow \mathbf{Np^{V}O_21^-}$	–2.39	–2.47	–4.07	–1.19	–0.02
$\mathbf{Pu^{VI}O_21} + e^- \rightarrow \mathbf{Pu^{V}O_21^-}$	–2.74	–2.80	–4.59	–0.68	–0.47

[a]ΔG_{solv} of Fc^+/Fc redox couple = –5.27 eV, [b]Hay correction U, Np, and Pu = –0.31, –1.17, and –0.21 eV

A recent study of penta–aqua actinyls yielded p5 PBE/DZP reduction potentials for the series of complexes containing uranium, neptunium, and plutonium of –0.58, 0.80, and 0.36 eV relative to a ferrocenium/ferrocene (Fc^+/Fc) potential of –5.20 eV [58, 88, 89]. Comparing the results of the $AnO_2(H_2O)_5^{2+/1+}$ series of redox couples to results for the $\mathbf{An^{VI}O_21/An^{V}O_21^-}$ series of this study, we find the Np > Pu > U trend remains the same (Figure 4–6).

Figure 4–6. Redox potentials across actinide series for both the $\mathbf{An^{VI}O_21/An^{V}O_21^-}$ (calculated ▲; predicted ●) couple relative to the ferrocene/ferrocenium couple and the $AnO_2(H_2O)_5^{2+/1+}$ (calculated ♦; experiment ■) couple relative to the standard hydrogen couple (eV), see the text

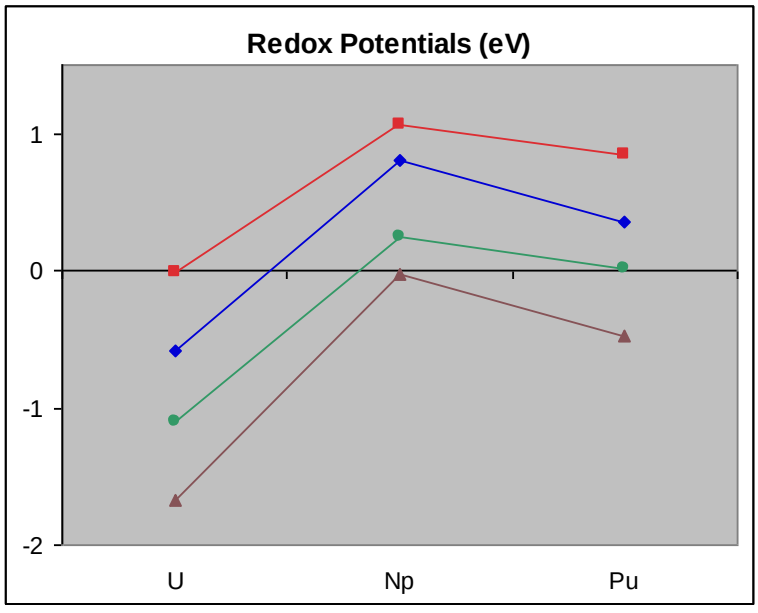

Furthermore with available experimental results for the $AnO_2(H_2O)_5^{2+/1+}$ series of Fc^+/Fc redox couples (-0.01, 1.07, and 0.84 eV) [95], we were able to determine the corresponding amounts (0.57, 0.27, and 0.48 eV) by which the calculated results underestimated these experimental values. Using these underestimated values as corrections we obtained rough approximations (–1.10, 0.25, and 0.01 eV) to experimental values for the $\mathbf{An^{VI}O_21/An^{V}O_21^-}$ redox potentials across the series (Figure 4–6, green circles). Comparing the newly predicted redox potential to the available cyclic voltammetry data for the $\mathbf{U^{VI}O_21/U^{V}O_21^-}$ redox couple of –1.18 eV, obtained in a thf/$NBu^n_4BF_4$ solvent by the Edinburgh research group [136] we find it to be within 0.08 eV of our predicted value.

4.4 Conclusion

Density functional computational methods are used to study a new form of binucleating Schiff–base macrocycles containing actinyl cations $U^{VI}O_2^{2+}$, $U^{V}O_2^{+}$, $Np^{VI}O_2^{2+}$, $Np^{V}O_2^{+}$, $Pu^{VI}O_2^{2+}$, and $Pu^{V}O_2^{+}$ within the first cavity and 3d transition metal cations Mn^{II}, Fe^{II}, Co^{II}, and Zn^{II} within the second cavity.

Formal bond order evidence is provided for transition metal to actinyl–endo–oxygen partial bond formation for all $\mathbf{An^{VI}O_22–5}$ and $\mathbf{An^{V}O_22–5^-}$ complexes (M–O2 = 0.36 to 0.81). Bond order evidence of metal–to–metal partial bond formation found for: $\mathbf{U^{VI}O_23}$ (0.50), $\mathbf{Np^{VI}O_22}$ (0.38) , and $\mathbf{Np^{VI}O_23}$ (0.52) is thought to be an artifact of the theoretical formal bond order calculations since all three have actinide to transition metal

bond distances of greater than 3.670 Å. This does, however, bring into question whether the other bond orders obtained can be trusted, and based on comparison to bond lengths that have be measured against experiment they seem reasonable.

Three instances of case 2 are identified, where offset transition metals form 3 rather than 2 strong N bonds resulting in distorted geometries for: $\mathbf{Np^{VI}O_2 2}$, $\mathbf{Pu^{VI}O_2 2}$, and $\mathbf{Pu^{VI}O_2 3}$. As well, five instances of case 3 occur, where TM's of the $\mathbf{U^{V}O_2 3^{-}}$, $\mathbf{Np^{V}O_2 3^{-}}$, $\mathbf{Pu^{V}O_2 3^{-}}$, $\mathbf{U^{V}O_2 5^{-}}$, and $\mathbf{U^{V}O_2 5^{-}}$ complexes are located above the cavity plane closer to actinyl–endo–oxygen displacing thf solvent molecules. With most of the chemical variation found to occur in Mn, Fe and Zn complexes the most likely common denominator is thought to be the greater atomic charge found on Mn, Fe, and Zn relative to Co.

Redox potentials for $\mathbf{An^{VI}O_2 1/An^{V}O_2 1^{-}}$ couples were determined to have a nearly identical trend Np > Pu > U to those previously studied for $AnO_2(H_2O)_5^{2+/1+}$ [58, 95]. We can therefore conclude that this trend in relative redox potentials is primarily a function of the actinide metal and not the ligand system. The Shamov et al. [95] results were found to underestimate the experimental $AnO_2(H_2O)_5^{2+/1+}$ redox potentials by 0.57 eV, 0.27 eV, and 0.48 eV for U, Np, and Pu, respectively. These energy displacements allowed us to roughly predict $\mathbf{An^{VI}O_2 1/An^{V}O_2 1^{-}}$ redox potentials of U = –1.10 eV, Np = 0.25 eV, and Pu = 0.01 eV. We then compared the predicted value for the uranyl moiety $\mathbf{U^{VI}O_2 1/U^{V}O_2 1^{-}}$ of –1.10 eV to the experimental cyclic voltammetry redox potential result of –1.18 eV determined in a thf/$NBu^{n}_4BF_4$ solvent by the Edinburgh research group [136]. The 0.08 eV difference lends some support to the potential accuracy of the

somewhat *ad hoc* values predicted for both the $\mathbf{Np^{VI}O_21/Np^{V}O_21^-}$ and $\mathbf{Pu^{VI}O_21/Pu^{V}O_21^-}$ redox potentials.

For the first time computational methods are used to provide reasonably expedient and accurate results for bimetallic actinide-containing structures of this size (108 atoms) while at the same time taking into relativistic effects in determining gas-phase geometries and gas- and solution-phase energetics.

CHAPTER FIVE

SUMMARY AND OUTLOOK

5.1 Summary

In this thesis we first report the computational results of a density functional study of 73 UN_4O_{12} isomers containing uranyl nitrate, $UO_2(NO_3)_2$, as a component. The isomers are grouped into three categories and nineteen types. 44 isomers of 14 types are dinitrogen tetroxide adducts of uranyl nitrate, $UO_2(NO_3)_2{\cdot}N_2O_4$, 22 are nitrosonium salt adducts of uranyl nitrate, $NO^+UO_2(NO_3)_3^-$, $NO^+UO_2(NO_3)_2O(NO_2)^-$, $NO^+UO_2(NO_3)_2(ONOO)^-$ or $(NO^+)_2UO_2(NO_3)_2O_2^{2-}$ and 7 are bis(nitrogen dioxide) adducts of uranyl nitrate, $UO_2(NO_3)_2{\cdot}2NO_2$. The 22 most stable isomers in solution, representing the 20 most stable gas-phase isomers, were selected for a more detailed analysis. Of these selected structures only two categories and six types were represented. Structures, frequencies, gas-phase and solution energetics, atomic charges, dipole moments, and the bonding within the N_2O_4 unit and between NO^+ and $UO_2(NO_3)_3^-$ components have been analyzed in detail. Based on relative Gibbs free energy calculations five isomers (the N_2O_4 adducts **a1**, **a2** and **a3**, and the nitrosonium salts **b1** and **b2**) were identified as strong candidates to exist and possibly predominate in the gas-phase, with **a1** and **a2** being the strongest candidates. Similarly, four isomers (**a6**, **a5**, **a8** and **a1**, all of them N_2O_4 adducts) were identified as strong candidates to exist and possibly predominate in a nonaqueous solution of nitromethane/dinitrogen tetroxide. Of these, **a6** was determined to be the most likely candidate to predominate in solution. In

addition, computational evidence of four new N_2O_4 isomers **20**, **22**, **27** and **28** in both gas- and solution-phase is presented for the first time.

Density functional theoretical (DFT) methods are then used to study a new form of binucleating Schiff–base polypyrrolic macrocycles $\mathbf{An^{X}O_21–5}$ (X = VI or V) containing actinyl ions $[AnO_2]^{n+}$ (An = U, Np, Pu; n = 1, 2) and 3d transition metals: no TM **1**, Mn **2**, Fe **3**, Co **4**, and Zn **5**. Recent experimental synthesis and X–ray crystal diffraction analysis of the recently identified uranyl moieties $\mathbf{U^{VI}O_21–4}$ has provided us with first time knowledge into these complexes and has led to our computational investigation across this series of actinyl structures. Formal bond order evidence is provided for twenty-four transition metal to actinyl–endo–oxygen partial bond formations (M–O2 = 0.36 to 0.81) within the $\mathbf{An^{X}O_22–4}$ complexes. Two sets of non-standard structural forms were identified as special cases: (1) case 2, with offset transition metals forming three instead of two strong N bonds resulting in distorted geometries for: $\mathbf{Np^{VI}O_22}$, $\mathbf{Pu^{VI}O_22}$, and $\mathbf{Pu^{VI}O_23}$, and (2) case 3, with no thf–TM bond for: $\mathbf{U^{V}O_23^{-}}$, $\mathbf{Np^{V}O_23^{-}}$, $\mathbf{Pu^{V}O_23^{-}}$, $\mathbf{U^{V}O_25^{-}}$, and $\mathbf{U^{V}O_25^{-}}$.

Redox potentials for $\mathbf{An^{VI}O_21/An^{V}O_21^{-}}$ couples were determined to have a nearly identical trend Np > Pu > U, to those previously studied of $AnO_2(H_2O)_5^{2+/1+}$. Energy displacements from the $AnO_2(H_2O)_5^{2+/1+}$ study allowed us to roughly predict $\mathbf{An^{VI}O_21/An^{V}O_21^{-}}$ redox potentials of U = –1.10 eV, Np = 0.25 eV, and Pu = 0.01 eV. Furthermore, the Edinburgh research group's [136] experimental cyclic voltammetry redox potential result for $\mathbf{U^{VI}O_21/U^{V}O_21^{-}}$ of –1.18 eV in thf/$NBu^{n}{}_4BF_4$ solvent is found to be within 0.08 eV of the predicted value. For the first time computational methods are used to provide expedient and accurate results for bimetallic structures of this size (108

atoms), while at the same time taking into account electron correlation and relativistic effects, in determining gas-phase geometries and gas- and solution-phase energetics.

5.2 Outlook

The small group of early actinides investigated (U, Np, Pu) is unlike any other in the periodic table, with coordination numbers of between one to thirteen possible and oxidation states ranging from two to seven and maybe even eight for Pu, resulting in a variety of states capable of existing at the same time in solution with similar and often reversible redox potentials. Because of this, many areas of actinide and actinyl complexation chemistry remain relatively unexplored. Some of the emerging new topics in actinide and actinyl complexation include complexation by neutral ligands in aqueous solution, the formation of mixed ternary complexes, and the behavior of complexes in alkaline solutions. In addition, studies of ligands that are capable of stabilizing difficult to attain oxidation states with well-defined actinide binding sites, as well as studies of soft donor ligands, are also likely to create new actinide chemistry.

More importantly the question of nuclear waste has become the largest single issue standing in the way of further development of this otherwise non-polluting source of energy. There are basically three choices for the management of spent nuclear fuel: (a) recycle to recover reusable components, (b) geolocical disposal as waste, or (c) long-term monitoring of surface or near–surface waste.

Actinide separations of spent fuels primarily involve hydrometallurgical solvent extraction processes. However, processing to recover plutonium is no longer the principal driving force for research into the complexes used in separations. The need for waste cleanup and environmental restoration, as well as reducing the quantity of hazardous chemicals generated by the existing nuclear fuel cycle, mainly through improvements in existing separations techniques, has become the primary concern.

The large volume of alkaline mixed wastes in underground storage tanks currently represents a long-term potential threat to the surrounding environment. Due to the high complexity of these wastes, which take on the form of sludges, solid–solutions, and alkaline or acidic solutions and slurry phases, minimization of both the volume and types of wastes going to repositories has become of critical importance. Two important areas of development are: improving washing procedures to selectively separate actinides and industrial scale separations within alkaline solutions.

A more permanent strategy for the elimination of potential long-term hazards of actinide wastes is to "incinerate or burn" (transmutation via neutron bombardment) them and thus transform them into short-lived fission products. This remedy also has the potential added benefit of providing a source of energy and because transmutation occurs, weapons proliferation concerns are minimized as well. Two areas of relevant research are the fast reactors/pyrometallurgical process and the development of new soft–donor extractants for actinide/lanthanide separations.

The continued development of solvent extraction technology may assist in securing public acceptability of fission–based nuclear power as a potentially viable

strategy for combating global warming through the reduction in greenhouse gas emissions.

As for decontamination of the terrestrial environment, the development of reliable speciation techniques and thermodynamic models, solid–solution separation methods for removal of actinides from soils, and solution–mineral conversion techniques to fix residual actinides on site and inhibit their entry into the hydrosphere/biosphere are also important areas of research.

Furthermore, the development of more advanced X–ray, neutron and EXAFS spectroscopy techniques, as well as improved relativistic DFT quantum mechanic methods in both gas-phase and solution accompanied by faster computational times, will be crucial in moving forward.

With the complex nature and growing abundance of stored nuclear wastes at many repository sites, the environmental uncertainties of actinide migration via groundwater contamination, the continuing improvements in extraction techniques for fuel processing and reprocessing schemes for heavy metal recovery, and the growing fundamental academic interests in these challenging elements, advances in actinide and actinyl chemistry are certain to continue to be of increasing importance into the foreseeable future [1].

Research into the UN_4O_{12} isomers has enabled us to identify, with some degree of confidence, the most likely isomers to exist and predominate in both gas-phase and non-aqueous solution. A component of these isomers, uranyl nitrate $UO_2(NO_3)_2$, is considered to be the most abundant salt found in the reprocessing of spent nuclear fuel and uranyl nitrate hexahydrate, $UO_2(NO_3)_2{\cdot}6H_2O$, is one of the most important compounds of the

PUREX process for the separation of fission products from uranium and plutonium fuels and a main wastewater pollutant. Therefore, in providing experimentalists with strong candidates, along with accompanying molecular properties, it is our hope that it will prove to be useful in identifying the existence of these UN_4O_{12} structures within both the solution and the gas phases. Furthermore, as a result the potential to better understand and advance separation methods within such environments, in which they are commonly found, may become possible.

In regards to the continuation of the ongoing investigation into the UN_4O_{12} isomers, the use of optimized gas-phase geometries to calculate single-point relative Gibbs free energies in solution is not ideal and optimizing these geometries in solution would allow us to verify not only the energetic ordering of these structures in solution but also that their geometries do not change substantially from those obtained in the gas-phase. Though current methods present difficulties with convergence it is my understanding that Scientific Computing & Modelling (SCM) intends to improve their SCF convergence methods within their ADF software in the near future and this should allow for improved optimization calculations in solution to be made.

As for our research into the second case study of the binucleated Schiff–base polypyrrolic macrocycles, the resulting desymmetrization provided us with the rare opportunity to investigate the nature of bonding between an actinyl-oxygen and dicationic transition metals. Formal bond order evidence is provided for transition metal to actinyl-endo-oxygen partial bond formation for all twenty-four complexes analyzed. Access to the selective chemical reactivity of one of the actinyl oxygens would be

desirable to further the understanding of the speciation of the early actinides commonly found in the nuclear fuel cycle and radioactive wastes.

Such uncommon structures can also be classified as cation-cation and bimetallic and further investigations into geometries, atomic charges, energies and redox potentials provide valuable insight into the understanding of these complexes.

Growing interest in complexing early actinides and their actinyls has been created due to the possibilities for the selective extraction of their radionuclides. The ability to vary ring size and to alter the identity of donor atoms has also resulted in the possibility for the tailoring of specific cations and oxidation states within the ligand cavities of such structures. Complexes with two centers of reactivity offer the potential for variations and improvements in new and existing reaction chemistry and catalysis by transition metals. Interest in redox potentials has been mostly driven by the need for developing separations and process chemistry relating to the nuclear fuel cycle. However, more recently the environmental concern of treating nuclear wastes containing this early series of actinide elements has led to increased interest.

Continuation of research for the polypyrrolic macrocycles would involve the addition of Americium to complete the study of the early actinide series and allow for a broader comparison that would benefit the analysis of the overall data. Also, the inclusion of relativistic spin–orbit and multiplet effects not included in the single–configuration DFT wave function are found to be necessary to obtain accurate energetic results. The *ad hoc* Hay correction used appears to give reasonably good results but there is limited data available to say definitively that it provides consistently good results. The incorporation of spin–orbit and multiplet effects within the DFT wave function or as an addition to the

DFT wave function should improve the accuracy of the obtained results. The experimental research team, which we have been collaborating with, at the University of Edinburgh, has already shown that a reaction between the uranyl THF adducts and excess pyridine results in THF substitution and the formation of mono-pyridine adducts, $[UO_2(py)(H_2L)]$, leaving the other actinyl and TM moieties still to be investigated. Furthermore, this raises the possibility of exploring the stabilities of these complexes within other polar, aprotic solvents that may be of interest. As well, if we consider other combinations of TM's the magnitude of potential new research soon becomes quite substantial.

The Edinburgh team has also suggested that we look into investigating binucleated An^{V}–An^{III} complexes [123]. Such complexes have the potential of forming under conditions where mixtures of actinides in various oxidation states are found to exist, such as those found in separations of spent fuels and waste reprocessing. Finally, an in-depth comparison of the relative solvent extraction capabilities to other related macrocycles (crown ethers, calixarenes, expanded–porphyrins, and phthalocyanines) within different solvents and under various conditions remains to be investigated. This would allow us to identify any potential solvent extraction advantages such binucleated polypyrrolic macrocylces may have to offer.

APPENDIX

A.1 Results and Discussion

A.1.1 The Structural Components

The majority of the nitrogen oxide and oxoion species discussed below were found to combine with uranyl nitrate to form gas- and solution-phase optimized UN_4O_{12} isomers.

A.1.1.1 Uranyl, Uranyl Nitrate, Dioxygen and Superoxide

The U=O bond length of 1.70 Å for uranyl in uranyl nitrate **1**, Figure 3–1, is a calculated value using the Stuttgart SC–ECP (60 e) for uranium and the DFT/B3LYP/TZVP combination for oxygen and nitrogen [102, 103].

The bond lengths of uranyl nitrate **2** were calculated using the Stuttgart SC–ECP (60 e) for uranium and the DFT/SVWN/TZVP combination for oxygen and nitrogen [102, 103]. SVWN combines a Slater exchange functional [104] with the Vosko, Wilk, and Nusair correlation functional [105]. Uranyl nitrate contains two nitrates and not one as the name suggests (reaction A–1).

The superoxide anion **4** forms from the one electron reduction of molecular oxygen (dioxygen) **3** in aprotic solvents such as nitromethane (reaction A–2).

Experimental bond lengths for dioxygen and superoxide are 1.21 and 1.33 Å, respectively [99].

$$\mathbf{UO_2^{2+}(l) + 2(NO_3^-)(l) \rightarrow UO_2(NO_3)_2(l)} \qquad \textbf{(A–1)}$$

$$\mathbf{O_2(g) + e^- \leftrightarrow O_2^-(l)} \qquad \textbf{(A–2)}$$

A.1.1.2 Nitric Oxide and Nitrosonium

The nitric oxide radical NO **5** has an experimental bond length of 1.15 Å [101], Figure 3–1. With a boiling point of –152 °C NO is thermodynamically unstable at room temperature, and at high pressures it readily decomposes to N_2O and NO_2 (reaction A–3). Colorless NO radicals are known to react rapidly with oxygen to form brown gaseous NO_2 (reaction A–4). Although the dimerization of NO does not occur at room temperature in the gas-phase, dimerization to planar *cis*– and *trans*–$(NO)_2$ does occur in solution (reaction A–5) [98]. Covalent NO has a theoretical bond order of 2.5 due to its unpaired anti–bonding electron. In solution the π^* electron is relatively easily lost (Δ_{ion} = 891 kJ/mol) to give the nitrosonium ion NO^+ **6**, which forms a variety of salts (reaction A–6). This leads to a stronger covalent bond with a theoretical bond order of 3 and a shorter bond length of 1.06 Å for NO^+ [99]. Nitrosonium salts are considered to be thermodynamically stable but chemically reactive. Gas-phase stretching modes for free NO and NO^+ of 1876 cm^{-1} [115], and 2390–2102 cm^{-1} are observed [100, 112]. The nitrosonium ion in salts is seen to absorb in the 2391–2150 cm^{-1} range [116]. Our gas-

phase calculations with DFT/B3LYP/cc–VTZ yielded a NO^+ stretching mode of 2353 cm^{-1} and a bond length of 1.07 Å. It has also been suggested that the larger the counteranion, the lower the NO^+ frequency due to the weakening of the N=O bond [100]. N_2O_3 (reaction A–11) and N_2O_4 (reaction 3–2) are also known to form nitrosonium cations by self-ionization.

$$\mathbf{3NO(g) \rightarrow N_2O(g) + NO_2(g)} \qquad \mathbf{(A–3)}$$

$$\mathbf{2NO(g) + O_2(g) \rightarrow 2NO_2(g)} \qquad \mathbf{(A–4)}$$

$$\mathbf{2NO(l) \rightarrow (NO)_2(l)} \qquad \mathbf{(A–5)}$$

$$\mathbf{NO(g) - e^- \leftrightarrow NO^+(l)} \qquad \mathbf{(A–6)}$$

A.1.1.3 Nitrogen Dioxide, Nitrite and Nitronium

Nitrogen dioxide NO_2 **7**, Figure 3–1, also loses its odd electron fairly easily (Δ_{ion} = 928 kJ/mol) to give NO_2^+ **9**, the nitronium ion (reaction A–7). NO_2 has a bent C_{2v} structure with an N=O bond length of 1.19 Å, and a bond angle of 133.8° [101], whereas NO_2^+ has a linear structure with two double bonded N=O groups of length 1.15 Å [99]. The nitrite anion NO_2^- **8**, however, is bent due to a lone pair of electrons on nitrogen leading to a bond length of 1.24 Å and an angle of 115.0° [99]. The nitronium ion is known to form in ionizing solvents such as CH_3NO_2. Self-ionization of N_2O_4 (reaction 3-3) and N_2O_5 (reaction A-13) are also known to result in nitronium cations. Many nitronium salts are considered to be thermodynamically stable, but are often very reactive

chemically and are rapidly hydrolyzed. IR active NO_2 stretches antisymetrically at 1612 cm^{-1}, whereas the corresponding symmetric mode at 1325 cm^{-1} is Raman active [116]. The bands attributed to adsorbed NO_2, however, are usually in the 1642–1605 cm^{-1} region [116]. The nitrite anion (also with C_{2v} symmetry) is found to asymmetrically stretch at 1260 cm^{-1} and symmetrically stretch at 1330 cm^{-1} [100, 115]. However, coordination of the nitrite anion to metal cations often results in drastic changes to its IR spectra [116]. Chelating bidentate NO_2^- groups are found to have IR symmetric and antisymmetric stretching bands of 1314–1266 cm^{-1} and 1203–1176 cm^{-1}, respectively [115]. The symmetric NO_2^+ vibrations are Raman active between 1408 and 1308 cm^{-1}. The respective antisymmetric mode is IR active in the 2392–2360 cm^{-1} region.

$$\mathbf{NO_2(g) - e^- \leftrightarrow NO_2^+(l)} \qquad \mathbf{(A–7)}$$

A.1.1.4 Nitrate and Peroxynitrite

Most metal cations form nitrate complexes, which are frequently hydrated and almost always soluble and difficult to reduce in water. A common way of producing them is via the disproportionation of N_2O_4 (reaction 3–2). The free nitrate anion NO_3^- **11**, Figure 3–1, has a planar D_{3h} symmetry and as a result it has an antisymmetric IR active mode at 1380 cm^{-1} and a symmetric Raman active mode at 1050 cm^{-1} [115]. Nitrates can be bound to metal cations either unidentately or bidentately and in general the stability of the complex increases in the same order [116]. The NO_3 radical **10** is not well

characterized, and is considered to be quite unstable [101]. However, the NO_3 radical is believed to play an important role in atmospheric chemistry [81, 82].

Peroxynitrite ions $OONO^-$ **14** are unstable isomers of the nitrate ion. They are obtained by a radical coupling reaction of NO with superoxide at pH 12–13 (reactions A– 8 and A–9) [137, 138]. Studies on the decay of peroxynitrite have revealed that below 5 °C and at pH 7 most isomerizes to nitrate, whereas at higher pH decomposition to nitrite and O_2 dominates. CCSD(T) calculated values of **12–15** [106] are shown in Figure 3–1.

$$\mathbf{O_2^-(l) + NO(l) \leftrightarrow ONOO^-(l)} \qquad \textbf{(A–8)}$$

$$\mathbf{O_2(l) + NO^-(l) \leftrightarrow ONOO^-(l)} \qquad \textbf{(A–9)}$$

A.1.1.5 Dinitrogen Trioxide

Unstable at room temperatures but stable at low temperatures, the weak N–N 1.86 Å bond [101] of the most common form, planar asym–N_2O_3 **16**, Figure 3–1, is rather reactive and readily dissociates, as a gas, into NO and NO_2 (reaction A–10). In solution, it undergoes self-ionization to NO^+ and NO_2^- (reaction A–11) [99].

$$\mathbf{N_2O_3(g) \leftrightarrow NO(g) + NO_2(g)} \qquad \textbf{(A–10)}$$

$$\mathbf{N_2O_3(l) \leftrightarrow NO^+(l) + NO_2^-(l)} \qquad \textbf{(A–11)}$$

A.1.1.6 Dinitrogen Pentoxide

In the gas-phase, planar N_2O_5 **29** is unstable and dissociates to NO_2 and NO_3 (reaction A–12), whereas in solution ionic dissociation occurs to produce NO_2^+ and NO_3^- (reaction A–13). N_2O_5 has been observed at low temperatures only. Known routes of formation are via strong oxidation of N_2O_4 by ozone (reaction A–14), interaction of NO_2 with NO_3 or dehydration of HNO_3 [99]. The IR spectrum of so-called covalent N_2O_5 is very similar to that of N_2O_4. Self-ionized N_2O_5 bands are 2375 cm^{-1} and 1400 cm^{-1} (for NO_2^+) and 1413 cm^{-1} (for NO_3^-) [115]. Experimental values [101] are shown in Figure 3–1.

$$\mathbf{N_2O_5(g) \leftrightarrow NO_2(g) + NO_3(g)} \qquad \textbf{(A–12)}$$

$$\mathbf{N_2O_5(l) \leftrightarrow NO_2^+(l) + NO_3^-(l)} \qquad \textbf{(A–13)}$$

$$\mathbf{N_2O_4(g) + O_3(g) \rightarrow N_2O_5(g) + O_2(g)} \qquad \textbf{(A–14)}$$

A.1.2 Classifications of UN_4O_{12} Isomers Containing Uranyl Nitrate

A.1.2.1 N_2O_4 Adducts

The remaining higher energy gas-phase optimized structures identified under the a–series category of the UN_4O_{12} isomers, $UO_2(NO_3)_2{\cdot}N_2O_4$ are shown in Figures A–1 to A–3.

Figure A–1. *Optimized UN_4O_{12} isomers – Uranyl Nitrate N_2O_4 adducts (bound NO_2 groups)* obtained from p5 PBE/cc–pVTZ gas-phase optimized geometries:

type 2 containing perp–ON·O·NO_2 **21**

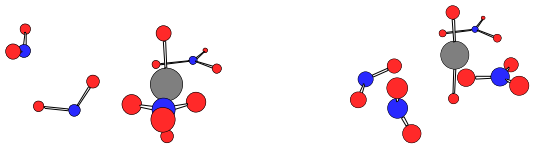

a18 a19

type 3 containing **TS21**

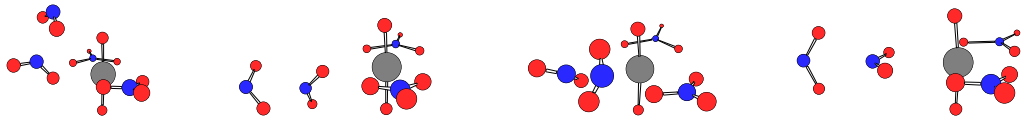

a23 a24 a25 a30

type 4 containing planar–ONO·NO_2

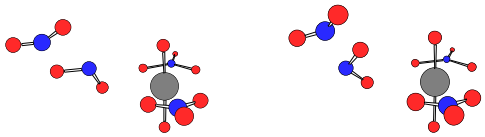

a20 a21

type 5 containing NO_2·O_2N **23**

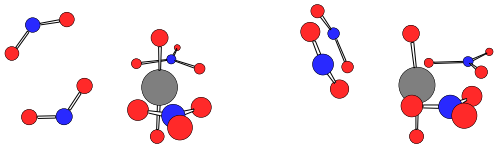

a26 a31

The fifth most stable solution-phase form of free N_2O_4 is perp–ON·O·NO_2 **21**. Only two type 2 forms containing **21** were found, **a18** and **a19**, with gas-phase relative Gibbs free energies of 8.6 and 9.3 kcal/mol, respectively. The four isomers classified as type 3 in Figure A–1 (**a23**–**a25** and **a30**) contain a transition state of **21**, which we have

labeled as **TS21**. The perpendicular cross structure of **TS21** is seen to contain an NO_2 group centrally located, with nitrogens aligned, between the two possible NO bound forms of **21** [108]. Of the UN_4O_{12} structures identified as containing **TS21**, isomers **a23– a25** are unidentately bound and **a30** is bidentately bound to uranium.

The type 4 UN_4O_{12} isomers containing planar–ONO·NO_2 **a20** and **a21** are characterized by a weak N–O bond between two planar NO_2 groups. Both have similar gas-phase relative Gibbs free energies of 12.5 and 13.0 kcal/mol, respectively. Our calculations show that planar–ONO·NO_2 is unstable and does not exist in its free N_2O_4 form.

The fifth type containing planar NO_2·O_2N **23** occurs twice as **a26** and **a31**, both times in relatively high-energy UN_4O_{12} isomers. The lowest energy form **a26** has a relative energy of 18.0 kcal/mol. This structural type is rather unique in that its two NO_2 groups are bound together via their four oxygens. In the unidentately bound version **a26** the two nitrogens are slightly offset, whereas in the bidentately bound version **a31** the two nitrogens are aligned.

cis–ON·O·NO_2 **18s** is considered to be the second most stable solution-phase form of free N_2O_4. The only type 7 UN_4O_{12} isomer not within the 22 selected UN_4O_{12} isomers was **a17** (Figure A–2).

Figure A–2. *Optimized UN_4O_{12} isomers – Uranyl Nitrate N_2O_4 adducts (NO_3 bound to a terminal nitroso [─N=O] or inverted nitrosonium cation)* obtained from p5 PBE/cc–pVTZ gas-phase optimized geometries:

type 7 containing *cis*–ON·O·NO_2 **18s**

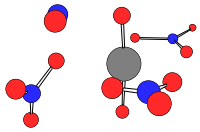

a17

type 8 containing ON·O_2NO **20**

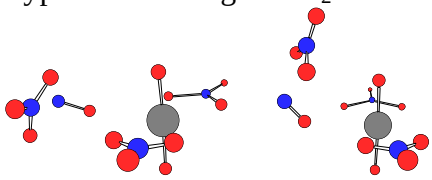

a34 a35

type 9 containing $NO^+NO_3^-$ **22**

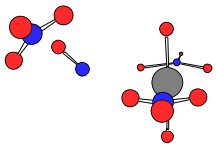

a44

The fourth most stable solution-phase form is ON·O_2NO **20**. The only type 8 UN_4O_{12} isomer not within the 22 selected UN_4O_{12} isomers was an inverted form with the nitroso (─N=O) group oxygen unidentately bound to uranium as **a34** and **a35**.

The only other occurrence of type 9 was **a44** containing $NO^+NO_3^-$ **22**, the sixth most stable solution form of free N_2O_4. Isomer **a44** corresponds to an inverted form of **a34**. Isomer **a44** is the only structure identified with a nitrogen atom bound to uranium.

The tenth type containing *cis,cis*–ON·OO·NO **24** first occurs as **a22**, with a gas-phase relative Gibbs free energy of 16.2 kcal/mol, and is characterized by the central peroxide bound bidentately side-on to uranium (Figure A–3). Other conformations are

type 11 containing *cis,trans*–ON·OO·NO **25** within isomer **a29** and type 12 containing *trans,trans*–ON·OO·NO **26** within isomers **a32** and **a35**.

Figure A–3. *Optimized UN_4O_{12} isomers – Uranyl Nitrate N_2O_4 adducts (two terminal nitroso [─N=O] groups bound to an O_2 group)* obtained from p5 PBE/cc–pVTZ gas-phase optimized geometries:

type 10 containing **24**

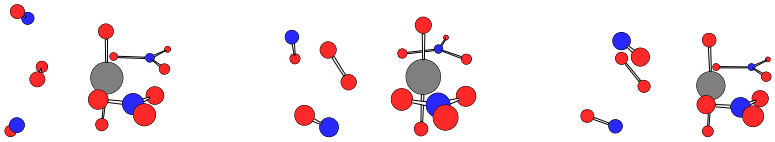

a22 a28 a29

type 11 containing **25**

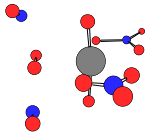

a30

type 12 containing **26**

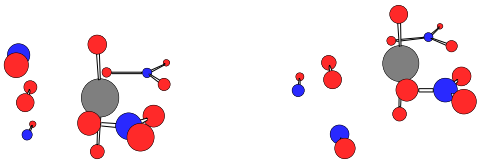

a33 a36

type 13 containing **27**

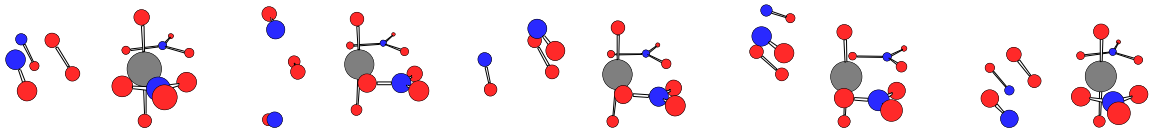

a37 a38 a39 a40 a41

type 14 containing **28**

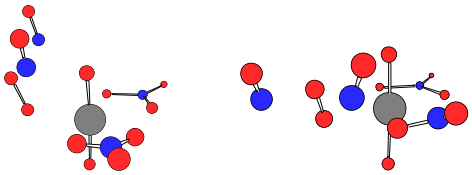

a42 a43

Our last two classifications are type 13 containing *cis,cis*–OO·$(NO)_2$ **27** within isomers **a36**–**a40** and type 14 containing *trans,trans*–OO·$(NO)_2$ **28** within isomers **a41**– **a42**. The respective relative Gibbs free energies of **a36** and **a41** are 25.1 and 37.7 kcal/mol.

A.1.2.2 Nitrosonium Salts

The second set of nine type 16 isomers **b5**, **b7**–**b11**, **b14** and **b21**–**b22** can be easily identified by an isolated third equatorial oxygen (in addition to the two axial uranyl oxygens) bonding to uranium forming a t-shaped structure (Figure A–4).

Figure A–4. *Optimized UN_4O_{12} isomers – Uranyl Nitrate Nitrosonium Salt adducts* obtained from p5 PBE/cc–pVTZ gas-phase optimized geometries:

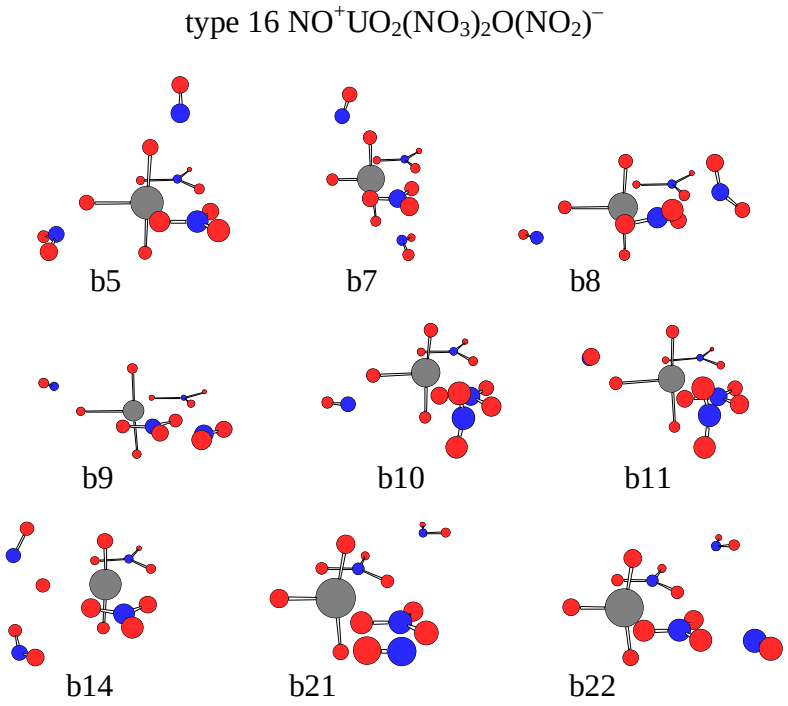

Both an NO^+ and an NO_2 ligand can be found at various locations within these structures. The gas-phase relative Gibbs free energy of **b5** is 11.1 kcal/mol. All b–series structures were found to characteristically consist of 7-coordinate uranium. Two structures **b21** and **b22** with the highest gas-phase relative Gibbs free energies of all the isomers calculated, 83.7 and 83.8 kcal/mol, respectively, are found to have the UO_3 structure with three oxygens double bonded to uranium. Calculated gas-phase bond lengths of 1.86 ± 0.03 Å and bond orders of 2.23 ± 0.03 for both structures verify the double bond character. An unsuccessful effort was made to locate previously identified *cis*–uranyl type structures for these complexes where two double bonded oxygens are at angles of 113° to 132° to each other [139].

The third set of seven type 17 structures **b12**, **b13** and **b15**–**b19**, Figure A–5, all contain a single high energy peroxynitrite radical or anion, group **9** or **14** (Figure 3–1). Of these only **b15** and **b19** contain *cis*–peroxynitrite unidentately bound to uranium and only **b16** contains a *trans*–peroxynitrite unidentately bound to uranium by the peroxide terminal oxygen. The gas-phase relative Gibbs free energy of the lowest isomer of this type **b12** is 26.8 kcal/mol.

The remaining b–series high-energy type 18 isomer **b20** has a gas-phase relative Gibbs free energy of 73.6 kcal/mol. Isomer **b20** is unique in that it appears to have two nitrosonium ions bound to uranyl nitrate as well as a superoxide anion bidentately bound to uranium.

Figure A–5. *Optimized UN_4O_{12} isomers – Uranyl Nitrate Nitrosonium Salt adducts* obtained from p5 PBE/cc–pVTZ gas-phase optimized geometries:

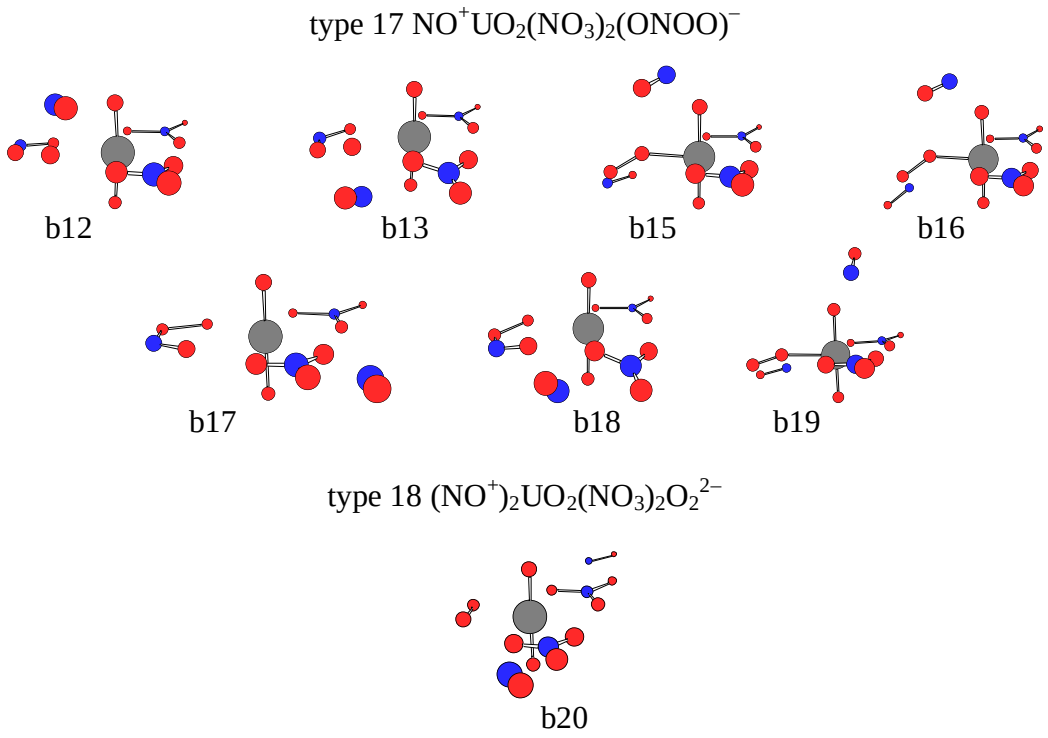

A.1.2.3 2·NO_2 Adducts

Isomers **c1**–**c5** are characterized by having one of the NO_2 groups bidentately bound to uranium. Only **c6** has a unidentately bound NO_2 group. Whereas, **c7** is the only structure that contains dual unidentately bound NO_2 groups. With the lowest relative energy gas-phase structure **c1** calculated to have a gas-phase relative Gibbs free energy 19.1 kcal/mol, it appears unlikely that this category of UN_4O_{12} isomers forms in any significant amounts relative to those with lower Gibbs free energies (Figure A–6).

Figure A–6. *Optimized UN_4O_{12} isomers – Uranyl Nitrate 2·NO_2 adducts* obtained from p5 PBE/cc–pVTZ gas-phase optimized geometries:

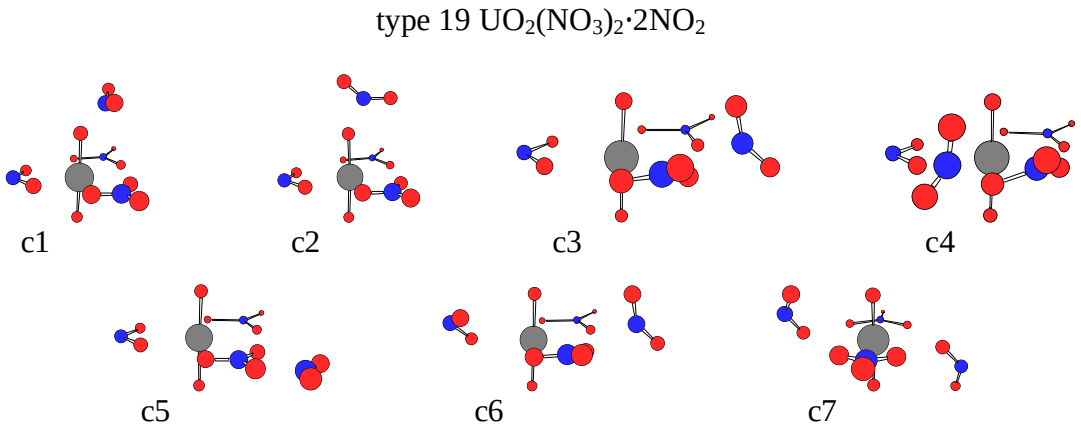

A.1.3 General Analysis and Discussion of Select UN_4O_{12} Isomers

A.1.3.1 Energies

The complete list of relative Gibbs free energies in gas-phase for three classifications of all 73 UN_4O_{12} isomers identified on the potential energy surface as minima is provided for three separate methods (Table A–1).

Table A–1. Calculated gas-phase optimized single-point relative Gibbs free energies (kcal/mol)

Isomers	p5 PBE G_{gas}^{rel}	p5 B3LYP G_{gas}^{rel}	g03 B3LYP G_{gas}^{rel}	Isomers	p5 PBE G_{gas}^{rel}	p5 B3LYP G_{gas}^{rel}	g03 B3LYP G_{gas}^{rel}
a1	0.0	0.0	0.0	a38	28.5	26.3	32.9
a2	1.0	0.2	–0.2	a39	28.4	26.5	32.4
a3	1.5	1.2	0.9	a40	29.9	28.9	35.0
a4	7.9	2.1	2.5	a41	34.5	34.5	39.6
a5	8.6	2.4	3.3	a42	35.8	37.7	44.2
a6	8.2	2.5	3.0	a43	38.8	39.8	46.3
a7	2.2	2.5	2.7	a44	43.5	49.1	46.2
a8	7.0	2.6	3.6	b1	3.9	1.4	4.2
a9	2.6	2.9	3.0	b2	6.5	1.7	3.8
a10	9.9	3.0	3.3	b3	5.3	2.6	5.5
a11	8.7	3.7	4.4	b4	5.9	3.6	6.1
a12	9.5	4.1	4.8	b5	11.7	11.1	14.3
a13	8.7	4.5	4.4	b6	19.2	15.7	15.5
a14	8.5	4.5	4.6	b7	20.4	23.7	27.5
a15	11.6	4.8	4.7	b8	25.1	25.8	28.4
a16	11.9	5.5	5.6	b9	26.3	27.2	28.1
a17	9.5	7.0	9.6	b10	27.1	27.4	28.3
a18	8.5	8.6	8.7	b11	27.7	27.6	28.6
a19	9.4	9.3	9.9	b12	30.0	26.8	33.1
a20	15.5	12.5	12.4	b13	32.5	28.4	34.3
a21	15.6	13.0	13.1	b14	29.2	33.9	38.5
a22	20.4	16.2	24.0	b15	35.3	36.5	43.5
a23	12.5	16.5	17.7	b16	38.2	38.8	45.4
a24	13.2	16.8	17.4	b17	41.3	39.3	43.2
a25	13.7	17.4	18.1	b18	43.7	41.7	45.9
a26	12.6	18.0	18.6	b19	49.5	62.7	69.2
a27	19.3	18.5	17.8	b20	56.4	73.6	78.3
a28	23.1	19.0	24.9	b21	62.2	83.7	84.5
a29	23.2	19.3	25.2	b22	61.9	83.8	84.9
a30	22.1	19.7	28.2	c1	16.9	19.1	22.2
a31	14.9	19.9	21.2	c2	17.2	19.6	22.7
a32	14.1	20.8	23.4	c3	19.9	19.8	22.0
a33	23.6	22.1	31.2	c4	20.9	20.1	22.6
a34	23.5	23.7	23.1	c5	22.0	21.6	22.5
a35	23.5	24.0	23.9	c6	23.5	30.9	31.6
a36	25.2	24.0	32.0	c7	25.9	40.0	43.1
a37	27.5	25.1	48.1				

BIBLIOGRAPHY

1. Berard, J.J., Shamov, G.A., and Schreckenbach, G., J. Phys. Chem. A, 2007. **111**(42): p. 10789-10803.

2. Morss, L.R., Edelstein, N.M., and Fuger, J., *The Chemistry of the Actinide and Transactinide Elements*. 3rd ed. 2006, The Netherlands: Springer: Dordrecht.

3. Clark, D.L., Hobart, D.E., and Neu, M.P., Chem. Rev., 1995. **95**: p. 25-48.

4. Cramer, C.J. and Truhlar, D.G., Chem. Rev., 1999. **99**(8): p. 2161-2200.

5. Tomasi, J., Mennucci, B., and Cammi, R., Chem. Rev., 2005. **105**(8): p. 2999-3093.

6. Spence, R., Talanta, 1968. **15**: p. 1307-9.

7. Songkasiri, W., Reed, D.T., and Rittmann, B.E., Radiochim. Acta, 2002. **90**(9-11): p. 785-789.

8. Fankuchen, I., Z. Kristallogr., 1935. **91**: p. 473-9.

9. Bradshaw, J.S., et al., *Comprehensive Supramolecular Chemistry: Molecular Recognition: Receptors for Cationic Guests*, G.W. Gokel, Editor. 1996, Pergamon: Oxford. p. 35-95.

10. Clark, D.L., et al., Angewandte Chemie, International Edition in English, 1998. **37**: p. 164-166.

11. Thuery, P., et al., *Calixarenes 2001*, ed. V.B. Z. Asfari, J. Harrowfield, J. Vicens. 2001, Dordrecht: Kluwer Academic. 561-82.

12. Sessler, J.L., Camiolo, S., and Gale, P.A., Coord. Chem. Rev., 2003. **240**(1-2): p. 17-55.

13. Sessler, J.L., et al., Inorg. Chim. Acta, 2002. **341**: p. 54-70.

14. Sessler, J.L. and Seidel, D., Angew. Chem. Int. Ed., 2003. **42**(42): p. 5134-5175.

15. Sessler, J.L., et al., Inorg. Chem., 2005. **44**(7): p. 2125-2127.

16. Sessler, J.L., et al., Coord. Chem. Rev., 2001. **216-217**: p. 411-434.

17. Sessler, J.L. and Weghorn, S.J., *Tetrahedron Organic Chemistry Series: Expanded, Contracted and Isomeric Porphyrins*. Vol. 15. 1997, Oxford: Pergamon.

18. Schreckenbach, G., Hay, P.J., and Martin, R.L., J. Comput. Chem., 1999. **20**: p. 70-90.

19. Blackwell, L.J., King, T.J., and Morris, A., J. Chem. Soc., Chem. Commun., 1973. **17**: p. 644.

20. Streitwieser, A., Inorg. Chim. Acta, 1984. **94**: p. 171-177.

21. Pepper, M. and Bursten, B.E., Chem. Rev., 1991. **91**: p. 719-741.

22. Dolg, M., *Lanthanides and Actinides*, in *Encyclopedia of Computational Chemistry*, P.R.v. Schleyer, Editor. 1998, Wiley Interscience: New York. p. 1478-1486.

23. Kaltsoyannis, N., Chem. Soc. Rev., 2003. **32**: p. 9-16.

24. Vallet, V., et al., Theor. Chem. Acc., 2006. **115**(2-3): p. 145-160.

25. Sonnenberg, J.L., et al., Inorg. Chem., 2005. **44**(7): p. 2255-2262.

26. Denning, R.G., J. Phys. Chem. A, 2007. **111**(20): p. 4125-4143.

27. Hay, P.J. and Martin, R.L., Los Alamos Science, 2000. **26**: p. 382-391.

28. Cramer, C.J., *Essentials of Computational Chemistry: Theories and Models*. 2nd ed. 2004, Hoboken, NJ: Wiley.

29. Koch, W. and Holthausen, M.C., *A Chemist's Guide to Density Functional Theory*. 2000, New York: Wiley-VCH.

30. Hohenberg, P. and Kohn, W., Phys. Rev. B, 1964. **136**(3): p. 864.

31. Kohn, W. and Sham, L.J., Phys. Rev. A, 1965. **140**(4): p. 1133.

32. Fonseca Guerra, C., et al., Theor. Chem. Acc., 1998. **99**: p. 391-403.

33. te Velde, G., et al., J. Comput. Chem., 2001. **22**: p. 931-967.

34. Pye, C.C. and Ziegler, T., Theor. Chem. Acc., 1999. **101**: p. 396-408.

35. Baerends, E.J., et al., *ADF 2006.01*. 2006, Scientific Computing and Modelling, Theoretical Chemistry, Vrije Universiteit: Amsterdam, The Netherlands.

36. Perdew, J.P., Burke, K., and Ernzerhof, M., Phys. Rev. Lett., 1996. **77**: p. 3865-3868.

37. Becke, A.D., J. Chem. Phys., 1993. **98**: p. 5648-5652.

38. Lee, C., Yang, W., and Parr, R.G., Phys. Rev. B: Condens. Matter, 1988. **37**: p. 785.

39. Dunning, T.H., J. Chem. Phys., 1989. **90**: p. 1007.

40. Laikov, D.N., Chem. Phys. Lett., 2005. **416**: p. 116-120.

41. Almlof, J., *In Modern Electronic Structure Theory*, D.R. Yarkony, Editor. 1995, Worls Scientific: Singapore. p. 110.

42. Whitten, J.L., J. Chem. Phys., 1973. **58**: p. 4496.

43. Dunlap, B.I., Connolly, J.W.D., and Sabin, J.R., J. Chem. Phys., 1979. **71**: p. 3396.

44. Laikov, D.N., Chem. Phys. Lett., 1997. **281**: p. 151-156.

45. Kaltsoyannis, N. and Scott, P., *The f Elements*. 1999, New York: Oxford University Press.

46. Jensen, F., *Introduction to Computational Chemistry*. 2nd ed. 2007: John Wiley & Sons. 599.

47. Dirac, P.A.M., Proc. Soc. London, Ser. A, 1929. **123**: p. 714-33.

48. Foldy, L. and Wouthuysen, S.A., Phys. Rev., 1950. **78**: p. 29.

49. van Lenthe, E., Baerends, E.J., and Snijders, J.G., J. Chem. Phys., 1993. **99**: p. 4597-4610.

50. Dyall, K.G., J. Chem. Phys., 1994. **100**: p. 2118-2127.

51. Laikov, D.N. *An implementation of the scalar relativistic density functional theory for molecular calculations with Gaussian basis sets*. in *poster presentation, DFT2000 Conference*. 2000. Menton, France.

52. Laikov, D.N., *Ph.D. Thesis*. 2000, Moscow State University.

53. Laikov, D.N. and Ustynyuk, Y.A., Russ. Chem. Bull., 2005. **54**(3): p. 820-826.

54. van Lenthe, E., Baerends, E.J., and Snijders, J.G., J. Chem. Phys., 1994. **101**: p. 9783-9792.

55. van Lenthe, E., Ehlers, A., and Baerends, E.J., J. Chem. Phys., 1999. **110**: p. 8943-8953.

56. van Lenthe, E., van Leeuwen, R., and Baerends, E.J., Int. J. Quant. Chem., 1996. **57**: p. 281-293.

57. Küchle, W., et al., J. Chem. Phys., 1994. **100**: p. 7535-7542.

58. Hay, P.J., Martin, R.L., and Schreckenbach, G., J. Phys. Chem. A, 2000. **104**: p. 6259-6270.

59. Klamt, A., et al., J. Phys. Chem. A, 1998. **102**: p. 5074-5085.

60. Klamt, A. and Schüürmann, G., J. Chem. Soc., Perkin Trans. 2, 1993. **2**: p. 799-805.

61. Cossi, M., et al., J. Comput. Chem., 2003. **24**: p. 669-681.

62. Pascualahuir, J.L., et al., J. Comput. Chem., 1987. **8**(6): p. 778-787.

63. Schafer, A., et al., Phys. Chem. Chem. Phys., 2000. **2**: p. 2187-2193.

64. Bridgeman, A.J., et al., J. Chem. Soc., Dalton Trans., 2001(14): p. 2095-2108.

65. Mayer, I., Chem. Phys. Lett., 1983. **97**(3): p. 270-274.

66. Hirshfeld, F.L., Theor. Chim. Acta, 1977. **44**: p. 129-138.

67. Morris, D.E., Inorg. Chem., 2002. **41**(13): p. 3542-3547.

68. Mulliken, R.S., J. Chem. Phys., 1955. **23**: p. 1833-1840.

69. Taylor, J.C. and Mueller, M.H., Acta Crystallogr., 1965. **19**: p. 536.

70. Dalley, N.K., Mueller, M.H., and Simonsen, S.H., Inorg. Chem., 1971. **10**: p. 323-328.

71. Hughes, K.A. and Burns, P.C., Acta Crystallogr., Sect C: Cryst. Struct. Commun., 2003. **59**: p. I7-I8.

72. Ruas, A., et al., J. Phys. Chem. B, 2006. **110**(7): p. 3435-3443.

73. Pasilis, S., et al., J. Am. Soc. for Mass Spectrom., 2006. **17**(2): p. 230-240.

74. Kaplan, L., Hildebrandt, R.A., and Ader, M., J. Inorg. Nucl. Chem., 1956. **2**: p. 153-163.

75. Krivovichev, S.V. and Burns, P.C., Radiochemistry, 2004. **46**(1): p. 16-19.

76. Dehnicke, K. and Strahle, J., Chem. Ber., 1964. **97**: p. 1502.

77. Addison, C.C., Chem. Rev., 1980. **80**(1): p. 21-39.

78. Tikhomirov, G.A., et al., Z. Anorg. Allg. Chem., 2002. **628**(1): p. 269-273.

79. Brouard, M., et al., J. Chem. Phys., 2006. **124**(6): p. 064309-1 to 15.

80. Tolbert, M.A., Rossi, M.J., and Golden, D.M., Science, 1988. **240**(4855): p. 1018-1021.

81. Wayne, R.P., et al., Atmos. Environ., Part A, 1991. **25**(1): p. 1-203.

82. Brown, S.S., et al., J. Photochem. Photobiol., A, 2005. **176**(1-3): p. 270-278.

83. Crawford, M.J. and Mayer, P., Inorg. Chem., 2005. **44**(23): p. 8481-8485.

84. Addison, C.C., et al., J. Chem. Soc., 1964: p. 2354.

85. Frisch, M.J., et al., *Gaussian 03*. 2004, Gaussian, Inc.: Wallingford CT.

86. Stephens, P.J., et al., J. Phys. Chem., 1994. **98**: p. 11623-11627.

87. Shamov, G.A., Schreckenbach, G., and Vo, T.N., Chem. Eur. J., 2007. **13**(17): p. 4932-4947.

88. Shamov, G.A. and Schreckenbach, G., J. Phys. Chem. A, 2005. **109**: p. 10961-10974.

89. Shamov, G.A. and Schreckenbach, G., J. Phys. Chem. A, 2006. **110**(43): p. 12072-12072.

90. Batista, E.R., et al., J. Chem. Phys., 2004. **121**: p. 2144-2150.

91. Han, Y.-K. and Hirao, K., J. Chem. Phys., 2000. **113**: p. 7345-7350.

92. Han, Y.K., J. Comput. Chem., 2001. **22**: p. 2010-2017.

93. Schreckenbach, G., Int. J. Quant. Chem., 2005. **101**: p. 372-380.

94. Straka, M. and Kaupp, M., Chem. Phys., 2005. **311**: p. 45-56.

95. Shamov, G.A. and Schreckenbach, G., J. Phys. Chem. A, 2006. **110**(30): p. 9486-9499.

96. Charrin, N., Moisy, P., and Blanc, P., Radiochim. Acta, 2001. **89**(9): p. 579-585.

97. Bagnall, K.W., Robinson, P.S., and Stewart, M.A.A., J. Chem. Soc. (A), 1961: p. 4060.

98. King, R.B., *Inorganic Chemistry of Main Group Elements*. 1995.

99. Cotton, F.A., et al., *Advanced Inorganic Chemistry, 6th Ed.* 1999.

100. Laane, J. and Ohlsen, J.R., *Characterization of nitrogen oxides by vibrational spectroscopy,* in *Prog. Inorg. Chem.*, LIPPARD, Editor. 1980, Wiley: New York. p. 465-513.

101. Stirling, a., et al., J. Chem. Phys., 1994. **100**(4): p. 2910-2923.

102. de Jong, W.A., et al., J. Phys. Chem. A, 2005. **109**: p. 11568 - 11577.

103. de Jong, W.A., et al., Theor. Chem. Acc., 2001. **107**(1): p. 22-26.

104. Slater, J.C., Phys. Rev., 1951. **81**: p. 385-390.

105. Vosko, S.H., Wilk, L., and Nusair, M., Can. J. Phys., 1980. **58**: p. 1200.

106. Lebrero, M.C.G., Perissinotti, L.L., and Estrin, D.A., J. Phys. Chem. A, 2005. **109**(42): p. 9598-9604.

107. Olson, L.P., et al., J. Am. Chem. Soc., 2002. **124**(32): p. 9469-9475.

108. Mckee, M.L., J. Am. Chem. Soc., 1995. **117**(5): p. 1629-1637.

109. Addison, C.C., et al., J. Chem. Soc., Chem. Commun., 1973: p. 347-348.

110. Blackwell, L.J., Nunn, E.K., and Wallwork, S.C., J. Chem. Soc., Dalton Trans., 1975: p. 2068-2072.

111. Song, Y., et al., Chem. Phys. Lett., 2003. **382**(5-6): p. 686-692.

112. Givan, A. and Loewenschuss, A., J. Chem. Phys., 1989. **90**(11): p. 6135-6142.

113. Wang, X.F. and Qin, Q.Z., Int. J. Quant. Chem., 2000. **76**(1): p. 77-82.

114. Guerra, C.F., et al., J. Comput. Chem., 2004. **25**(2): p. 189-210.

115. Nakamoto, K., *Infrared Spectra of Inorganic and Coordination Compounds 2*. 2nd ed. 1970, New York: Wiley-Interscience.

116. Hadjiivanov, K.I., Cat. Rev. - Sci. Eng., 2000. **42**(1-2): p. 71-144.

117. Kobets, L.V., Klavsut, G.N., and Umreiko, D.S., Zh. Neorg. Khim., 1981. **26**(1): p. 173-178.

118. Givaja, G., et al., Chem. Commun., 2003(19): p. 2508-2509.

119. Givaja, G., et al., Chem. Commun., 2005(35): p. 4423-4425.

120. Givaja, G., et al., Angew. Chem. Int. Ed., 2007. **46**(4): p. 584-586.

121. Givaja, G., et al., Chem. Eur. J., 2007. **13**(13): p. 3707-3723.

122. Veauthier, J.M., et al., Inorg. Chem., 2005. **44**(19): p. 6736-6743.

123. Arnold, P.L., et al., Nature, 2008. **451**: p. 315-317.

124. Chang, C.J., et al., Inorg. Chem., 2002. **41**(12): p. 3102-3109.

125. Arnold, P.L., et al., Inorg. Chem., 2004. **43**(26): p. 8206-8208.

126. Arnold, P.L., et al., J. Am. Chem. Soc., 2006. **128**(30): p. 9610-9611.

127. Sullivan, J.C., Hindman, J.C., and Zielen, A.J., J. Am. Chem. Soc., 1961. **83**: p. 3373-8.

128. Newton, T.W. and Burkhart, M.J., Inorg. Chem., 1971. **10**: p. 2323-6.

129. Newton, T.W. and Baker, F.B., Inorg. Chem., 1962. **1**: p. 368-77.

130. Baudry, D. and Ephritikhine, M., J. Organomet. Chem., 1986. **311**(1-2): p. 189-192.

131. Li, J., et al., Inorg. Chem., 1996. **35**(16): p. 4694-4702.

132. Tsipis, C.A., Comments Inorg. Chem., 2004. **25**(1-2): p. 19-74.

133. Shamov, G.A. and Schreckenbach, G., *Theoretical Study of the Oxidative Nucleophilic Substitution of Hydrogen in the Uranyl Sapphyrin Complex*. 2005, University of Manitoba, unpublished results.

134. Jaque, P., et al., J. Phys. Chem. C, 2007. **111**: p. 5783-5799.

135. Tait, C.D., et al., Actinide Research Quarterly, 2004. **1**: p. 20-2.

136. Arnold, P.L., Patel, D., and Love, J.B., *Uranyl desymmetrisation in Pacman shaped macrocyclic complexes*. 2007, University of Edinburgh, unpublished results.

137. Blough, N.V. and Zafiriou, O.C., Inorg. Chem., 1985. **24**(22): p. 3502-3504.

138. Hughes, M.N., Biochim. Biophys. Acta, 1999. **1411**(2-3): p. 263-272.

139. Schreckenbach, G., Hay, P.J., and Martin, R.L., Inorg. Chem., 1998. **37**: p. 4442-4451.